**TECHNISCHE**
**UNIVERSITÄT**
**WIEN**

**VIENNA**
**UNIVERSITY OF**
**TECHNOLOGY**

D I S S E R T A T I O N

# Anatomical Modeling
# for Image Analysis in Cardiology

ausgeführt zum Zwecke der Erlangung des akademischen Grades eines
Doktors der technischen Wissenschaften

unter Anleitung von
Ao.Univ.Prof. Dipl.-Ing. Dr.techn. Eduard Gröller
Institut für Computergraphik und Algorithmen
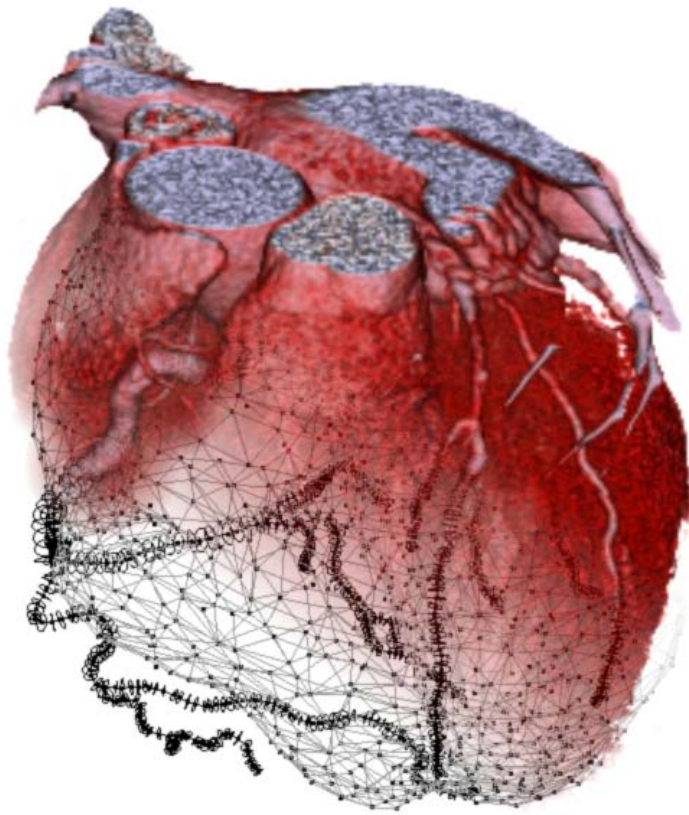der Technischen Universität Wien

in Zusammenarbeit mit
Katja Bühler und Jiří Hladůvka
vom VRVis Research Center

eingereicht
an der Technischen Universität Wien,
Fakultät für Informatik

von
Dipl.-Ing. Sebastian Zambal
Matrikelnummer 9826978
Ybbsitzerstraße 44a
A-3340 Waidhofen/Ybbs, Österreich
geboren am 4. 9. 1979

Wien, im März 2009.

# Anatomical Modeling
# for Image Analysis in Cardiology

# Abstract

The main cause of death in the western world is cardiovascular disease. To perform effective diagnosis of this kind of disease, modern medical imaging modalities offer great possibilities. In cardiology the advent of computed tomography (CT) and magnetic resonance (MR) scanners with high temporal resolution have made imaging of the beating heart possible. Large amounts of data are aquired in everyday clinical practice. Intelligent software is required to optimally analyze the data and perform reliable and effective diagnosis.

This thesis focusses on model-based approaches for automatic segmentation and extraction of clinically relevant properties from medical images in cardiology. Typical properties which are of interest are the volume of blood that is ejected per cardiac cycle (stroke volume, SV) or the mass of the heart muscle (myocardial mass).

Compared to other segmentation and image processing algorithms, the investigated model-based approaches have the advantage that they exploit prior knowledge. This increases robustness. Throughout this thesis models are discussed which consist of two important parts: shape and texture. Shape is modeled in order to restrict the geometric properties of the investigated anatomical structures. Texture on the other hand is used to describe gray values and plays an important role in matching the model to new unseen images.

Automatic initialization of model-based segmentation is important for many applications. For cardiac MR images this thesis proposes a sequence of image processing steps which calculate an initial placement of a model.

A special two-component model for segmentation of functional cardiac MR studies is presented. This model combines individual 2D Active Appearance Models with a 3D statistical shape model.

An approach to effective texture modeling is introduced. An information theoretic objective function is proposed for optimized probabilistic texture representation.

Finally a model-based coronary artery centerline extraction algorithm is presented. The results of this method were validated at a workshop at the international MICCAI conference. In a direct comparison the method outperformed four other automatic centerline extraction algorithms.

# Kurzfassung

Eine der häufigsten Todesursachen in der westlichen Welt sind kardiovaskuläre Krankheiten. Für die Diagnose dieser Krankheiten eröffnen moderne bildgebende Verfahren beeindruckende Möglichkeiten. Speziell in der Kardiologie hat die Entwicklung von Computertomographie (CT) und Magnetresonanztomographie (MRT) Scannern mit hoher zeitlicher Auflösung die Aufnahme des schlagenden Herzens ermöglicht. Um die großen Datenmengen, die in der täglichen klinischen Routine akquiriert werden, zu analysieren und eine optimale Diagnose zu erstellen, wird intelligente Software benötigt.

Diese Arbeit befasst sich mit modellbasierten Methoden für die automatische Extraktion von klinisch relevanten Eigenschaften von medizinischen Bildern in der kardialen Bildgebung. Typische Eigenschaften sind etwa das Schlagvolumen des Herzens (engl. stroke volume, SV) oder die Masse des Herzmuskels.

Im Vergleich zu anderen Algorithmen für die Segmentierung und Bildverarbeitung haben die untersuchten modellbasierten Ansätze den Vorteil, dass vorhandenes Wissen in den Segmentierungsprozess eingebunden wird und damit die Robustheit erhöht wird. In dieser Arbeit werden Modelle betrachtet, welche aus zwei essentiellen Teilen bestehen: Form und Textur. Form wird modelliert, um die geometrischen Eigenschaften der analysierten anatomischen Strukturen einzuschränken. Textur wird verwendet um Grauwerte zu modellieren und spielt eine wichtige Rolle bei der Anpassung des Formmodells an ein neues Bild.

Automatische Initialisierung von modellbasierter Segmentierung ist für viele Anwendungen interessant. Für kardiale MR Bilder wird in dieser Arbeit eine Folge von Bildverarbeitungsschritten vorgeschlagen, um eine initiale Plazierung des Modells zu berechnen.

Ein spezielles Modell für die Segmentierung von funktionalen kardialen MR Studien, welches aus zwei Komponenten besteht, wird erläutert. Dieses Modell kombiniert einzelne 2D Active Appearance Models mit einem statistischen 3D Formmodell.

Ein Ansatz zur effektiven Texturmodellierung wird vorgestellt. Eine informationstheoretische Zielfunktion wird für optimierte probabilistische Texturrepräsentation vorgeschlagen.

Modellbasierte Extraktion von Koronararterien wird am Ende der Arbeit

diskutiert. Die Resultate dieser Methode wurden auf einem Workshop auf der internationalen MICCAI Konferenz validiert. In einem direkten Vergleich schnitt diese Methode besser ab, als vier andere Ansätze.

# Acknowledgements

I would like to thank Katja Bühler for believing in me, for encouraging me to go forward in model-based segmentation and for giving me the chance to work at the VRVis research center.

I would like to thank Jiří Hladůvka for fruitful discussions, and for the constructive review of my work.

I am very thankful to Prof. Eduard Gröller for supporting my PhD over the large distance across the Danube river.

I would like to thank Armin Kanitsar for several extreme programming sessions during which I had the chance to get into contact with industrial software development.

I want to say "thank you" to all people at VRVis. I really enjoyed their companionship over the last few years.

Last but not least I want to thank my parents Christa and Walter Zambal. Without their support and encouragement this thesis would not have been possible.

# Contents

# List of Figures

# List of Tables

# Chapter 1

# Introduction

**Figure 1.1:** *Main causes of death and main causes of death through cardiovascular diseases in 2007 in Austria.*

## 1.1 Cardiac imaging

The most common cause of death in the western world is cardiovascular disease. Figure 1.1 illustrates the main causes of death in general and causes of death through cardiovascular disease in 2007 in Austria [57]. About 44% of deaths are caused by cardiovascular diseases. Among these, ischaemic heart disease (IHD) represents with 46% the largest fraction. Statistics like this show that efficient monitoring of cardiac disease is important for a very large number of patients.

In order to keep track of function and morphology of a patient's heart, various imaging techniques such as Magnetic Resonance Imaging (MRI) or Computed Tomography (CT) are nowadays available. The application of many of these imaging techniques for cardiology has matured in the last few years to a high degree. These techniques are now able to deliver high quality 3D images of the beating heart. There exists a broad spectrum of procedures in radiology to perform a morphological and functional analysis of the heart. To support the clinician in his/her workflow, modern imaging software for fast and realiable analysis of the captured image data is required.

### 1.1.1 Anatomy and Physiology of the Heart

The human heart consists of four chambers: Left atrium (LA), left ventricle (LV), right atrium (RA), and righ ventricle (RV). A schematic illustration of cardiac anatomy and comparison with a CT image are shown in figure 1.2. By performing periodic contractions, the heart pumps blood through the body. The right atrium receives deoxygenated blood. From

| (a) | (b) |
|-----|-----|
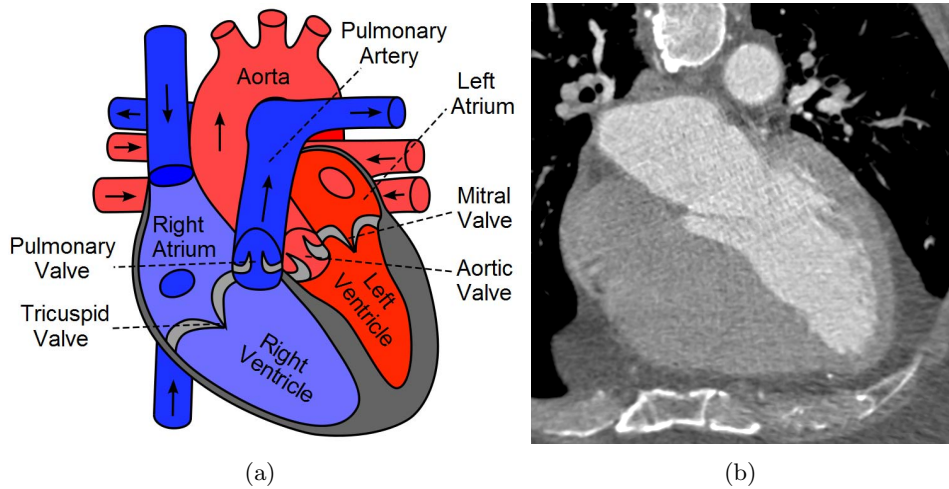
***Figure 1.2:*** *Schematic illustration of cardiac anatomy (a) and four-chamber view of the heart in cardiac computed tomography (b).*

the right atrium the blood flows into the right ventricle, which pumps it through the pulmonary artery into the lung arteries. After the blood has been enriched with oxygen within the lungs, it enters the left atrium through the lung veins. From the left atrium it proceeds to the left ventricle which pumps it through the aorta into the rest of the body.

Since the left ventricle has to pump blood into all parts of the body (except the lungs) it experiences a high resistance and has to generate considerable pressure. As a consequence, the wall of the heart muscle (myocardium) surrounding the left ventricle is significantly thicker than myocardium surrounding other heart chambers. It is also the left ventricle which plays a very important role in the analysis of cardiac function.

Ischaemic heart disease represents an important group of cardiac diseases This is clearly reflected by figure 1.1. Ischaemic heart disease is an under-supply of the myocardium with oxygen. The cause for this under-supply usually is narrowing (stenosis) of the coronary arteries that supply the muscle. If a permanent under-supply is given, sooner or later, cells in the affected tissue die (necrosis). This causes a myocardial infarction. Subsequently the contraction ability and the efficiency of the heart decreases.

Coronary arteries supply the myocardium with fresh oxygenated blood. To avoid ischaemic heart disease, monitoring of coronary arteries is important. The left coronary artery (LCA) and the right coronary artery (RCA) normally originate from the aorta. A few centimeters distal, the LCA normally splits into two larger branches: Left anterior descending (LAD) and left circumflex (LCx) arteries. A number of anatomical variations have been observed for coronary arteries [73, 25]. For example, the number of coronary origins (ostia) may be different: LCA and RCA may originate from a single

3
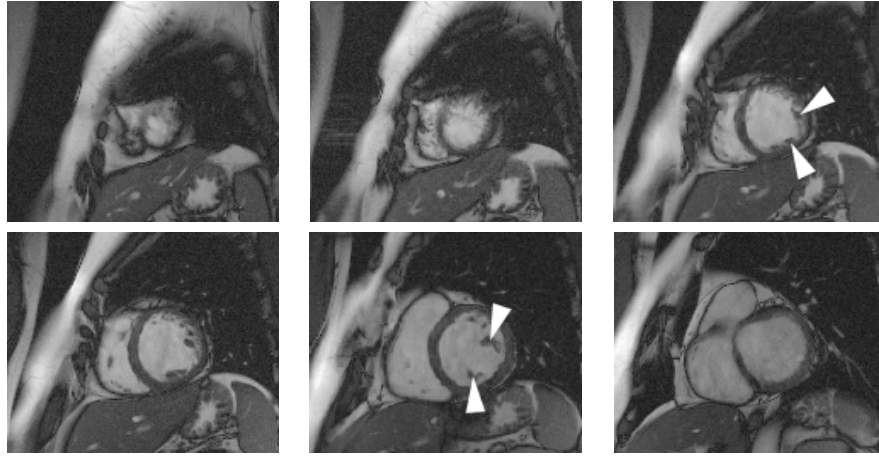
**Figure 1.3:** *Papillary muscles in MR short axis views.*
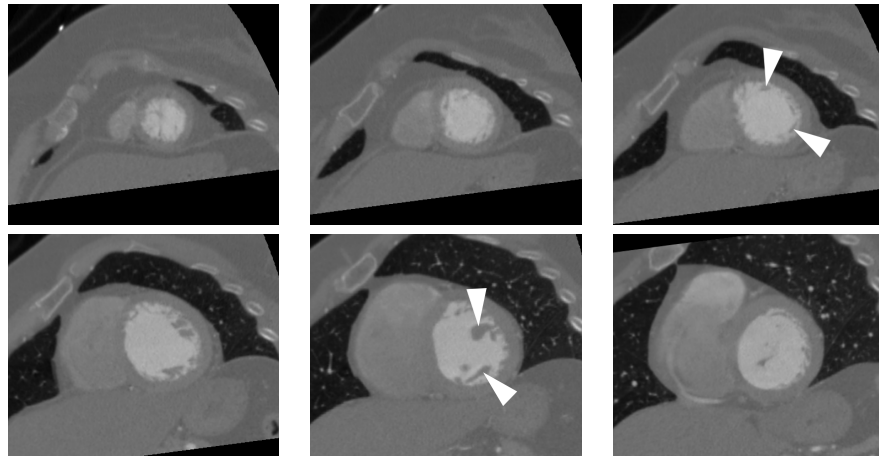


**Figure 1.4:** *Papillary muscles in contrast-enhanced CT short axis views.*

ostium. The other extreme is an increased number of coronary branches originating from the aorta. Three and even four different origins have been observed. In general, coronary anomalies are related to: coronary artery ostium, course of the artery, termination of the artery, and size of the artery. A model-based method for automatic coronary artery tracking is presented later in this thesis in chapter 6.

At the transitions from atria to ventricles and from ventricles to pulmonary artery and aorta, the flow of blood is controlled by cardiac valves (figure 1.2). Flow from the left ventricle into the aorta is governed by the aortic valve and flow from the right ventricle into the pulmonary artery is governed by the pulmonary valve. The tricuspid valve governs blood flow from right atrium to right ventricle. The mitral valve governs blood flow from the left atrium to the left ventricle. Because the mitral valve consists
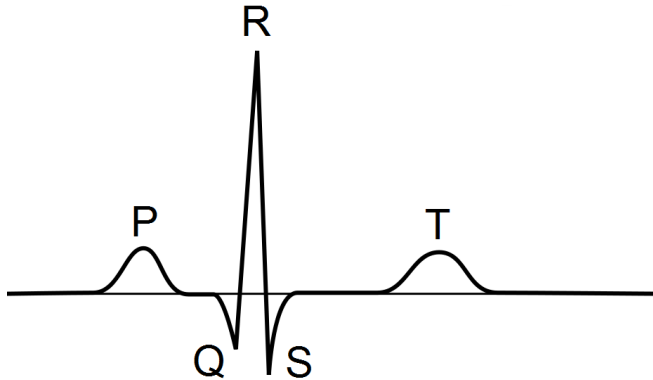
***Figure 1.5:*** *Electrocardiogram with preceding P-wave, QRS-complex, and T-wave.*

of only two cusps, it is also called bicuspid valve.

The tips of the cusps of both, mitral and tricuspid valve, are attached by tendons (chordae tendineae) to the papillary muscles. The papillary muscles are irregularly shaped muscles inside the ventricles. The plane in which mitral and tricuspid valve lie defines the base of the heart (basis cordis). The apex of the heart (apex cordis) is located at the tip of the ventricles.

Besides the papillary muscles, the inner surface of the ventricular myocardial wall exhibits other irregular muscular structures: the trabeculae carnae. Short axis views of MR and CT data clearly show papillary muscles and trabeculae (figures 1.3 and 1.4).

A problematic aspect arises from these trabeculae and the papillary muscles: A clinical definition of the interior surface of the myocardium is in many cases very hard to establish. This makes it difficult to reduce interobserver variability and to perform standardized segmentation of the anatomical structures. As a consequence, the irregular structures impose a challenge on the design, comparison, and evaluation of methods and algorithms for computer assisted image analysis.

An important source of complexity in cardiac imaging is the periodic contraction of the heart. The complex contraction mechanism is triggered by electrical impulses. These impulses originate from the sinoatrial node (SA node) which is located on the wall of the RA. From there the impulse spreads over the heart and makes firstly the atria and then the ventricles contract. Using electrodes placed upon the body surface, the electrical impulses of the heart are measured as electrocardiogram (ECG). The waveforms generated by an ECG enable triggering of modern imaging modalities. By identifying characteristic sections in the waveform (e.g. the R-wave, figure 1.5), the imaging process is synchronized with the patient's heart beat.

The complete heart cycle can be divided into two main phases: systole and diastole. In systole the heart ejects blood by contraction and in diastole

(a)           (b)
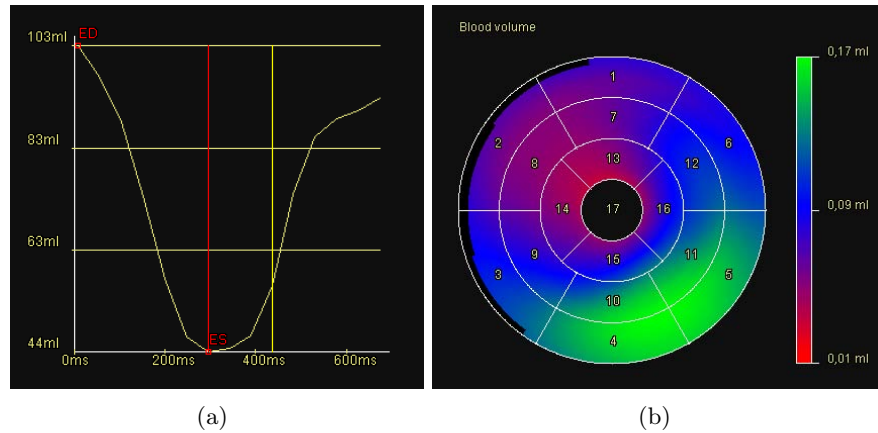
**Figure 1.6:** *A plot of the blood volume of the left ventricle over time (a); bull's eye view displaying regional blood volumes in different regions of the left ventricle (b).*

the heart relaxes. At the time steps of end-systole and end-diastole the ventricles of the heart are in contracted and relaxed state. For clinical analysis, end-systole and end-diastole are of major interest. In clinical routine mostly only these two time steps are investigated in more detail.

### 1.1.2 Analysis of Cardiac Function

An important issue in modern medical imaging is standardized evaluation of the investigated anatomy. Standard measures are important for clinicians to compare diagnoses, make better predictions, and effectively track morphological changes over time. Efforts are currently being undertaken to develop robust automatic image processing algorithms. This is not only done to support radiologists by reducing time-consuming manual image pre-processing. The long term goal is to open the door for better standards in medical image analysis which allow a more precise analysis and better comparability of diagnoses.

Important parameters of the heart and its function help the physician to effectively analyze a patient's heart and give a precise diagnosis. Typical parameters which are calculated in order to assess cardiac function are:

- End-systolic volume (ESV): The volume of blood contained in the left ventricle or right ventricle in end-systole.

- End-diastolic volume (EDV): The volume of blood contained in left ventricle or right ventricle in end-diastole.

- Stroke volume (SV): The volume of blood pumped within a single cardiac cycle (difference of end-diastolic and end-systolic volumes).

- Ejection fraction (EF): The fraction of stroke volume relative to end-diastolic volume. For a healthy heart the Ejection fraction is greater than 55%.

- Left ventricular regional stroke volumes: The stroke volumes of individual regions within the left ventricle.

- Left ventricular regional ejection fractions: The ejection fraction of individual regions within the left ventricle.

- Myocardial mass: The mass of the myocardium.

- Myocardial wall thickness: The thickness of the myocardium in end-diastole and end-systole. Also the progress of thickness over the complete heart cycle is of interest to the cardiologist.

- Stenosis grading of coronary arteries: In order to assess how well coronary arteries supply the heart with oxygen, a grading of stenoses (narrowings) of these arteries is performed.

- Calcium scoring: Calcium scoring is an attempt to quantify the severity of coronary artery disease. Severity of calcifications are mapped to a calcium score.

The above measures are usually displayed to the clinician as simple numbers or charts (e.g. varying left ventricular volume over the cardiac cycle as shown in figure 1.6(a)). For regional measures concerning the left ventricle (such as myocardial wall thickness) a bull's eye [9] can be used. The bull's eye maps the surface of the left ventricle to a plane. Color coding gives the clinician a comprehensive overview of regional measures over the complete surface of the left ventricle. An example of a bull's eye plot is shown in figure 1.6(b).

### 1.1.3   Cardiac Magnetic Resonance Imaging

The principle of Magnetic Resonance (MR) Imaging in cardiology (cardiac MR, CMR) is the same as for other organs: A strong magnetic field aligns the spins of atomic cores within the scanned body. These spins are excited by a radio frequency (RF) pulse. When the spins re-align with the magnetic field (relaxation), they send out a signal. Relaxation times T1 and T2 are measured and transformed into images. The intensities of these images are influenced by proton density, flow and motion, changes in susceptibility, molecular diffusion, magnetization transfer, etc. [27].

Two important sources of motion impose major difficulties in the cardiac MR imaging process: Contraction of the heart and respiratory motion. A conventional MR sequence would result in unreadable images caused by the strong motion artifacts. In order to account for cardiac contraction,

synchronization with an ECG is required. Several critical aspects have to be considered here: The ECG surface electrodes measure not only electrical currents from the heart but also currents which are induced by the magnetic field on the blood flow. As a result an increase in amplitude of the ST segment may cause false results in certain R-wave detection algorithms. Older ECG systems were influenced by RF pulses and the switching of the gradient fields due to the use of carbon leads. This problem has been largely banned due to increased use of fiber optics instead of carbon leads [27].

Basically two different strategies exist for synchronization of the imaging process with the beating heart: Prospective triggering and retrospective gating. In prospective triggering a preceding R-wave is used to trigger the image acquisition in the following R-R interval or cardiac cycle. In retrospective gating the data is acquired continuously over time and later matched to the simultaneously recorded ECG. Synchronization with ECG makes it possible to reconstruct the final images not only from a single phase in a single cardiac cycle. Images may as well be reconstructed from corresponding phases in different cycles [27].

Images from different spatial positions (different slices) are captured one after the other. This may cause slice misregistration in resulting images and reconstructed volume data. Due to patient motion such as free breathing or unequal depth of breath-holds, cardiac shifts of up to 1cm can occur. Such motion artifacts result in over- or underestimation of cardiac volumes during analysis [27]. With new parallel imaging techniques where multiple slices are captured at once, these problems can be reduced to some degree.

### 1.1.4   Cardiac Computed Tomography

Modern multidetector-row computed tomography (MDCT) with up to 64 detector rows has opened new perspectives for computed tomography (CT) imaging in cardiology. MDCT with ECG gating enables the acquisition of dynamic 3D image data from multiple time steps. This is a prerequisite for calculation of cardiac functional parameters such as left ventricular ejection fraction (EF) or Stroke Volume (SV). A critical aspect of CT for functional imaging, however, is the increased radiation exposure of the patient compared to other imaging modalities like MR and ultrasound.

An important application of CT in cardiology is the analysis of coronary artery disease (CAD). In computed tomography angiography (CTA), 3D images of coronary arteries are generated. CTA increasingly replaces conventional coronary angiography (CCA). Conventional angiography requires the use of a catheter for contrast agent injection. This catether is pushed through the aorta close to the origins of the coronary arteries. This means a certain risk for the patient. Contrast agent injection in CTA, by contrast, does not require a catheter and is thus considered a non-invasive technique. Although CCA is the gold standard for coronary lumen evaluation, this pro-

cedure offers little information on coronary artery arteriosclerosis. Although CTA is still emerging it will be a major cardiovascular imaging option in the future [11].

As in MR, the contraction of the heart imposes several difficulties on the CT imaging process. A synchronization with ECG helps to acquire reasonable image information. The speed of image acquisition of a CT scanner is limited by its gantry rotation time. For volumetric image reconstruction half a gantry rotation has to be performed. Current CT scanners perform half a rotation in between 165ms and 210ms [25].

Optimally cardiac motion should be minimal during the time interval of the acquisition process. Assuming an optimal heart rate of 50 to 60 beats per minute, data for a 3D (single time step) volume reconstruction can be acquired in a single cardiac cycle. Given a sufficiently slow heart beat, the phase in the cardiac cycle where minimal motion occurs is in mid-diastole. With prospective triggering the peak in radiation is applied during the selected cardiac phase. Thus by using prospective ECG triggering, a satisfactory image quality with reduced motion artifacts can be achieved by keeping the radiation dose at a low level.

Prospective triggering may not be accurate enough when irregular contraction of the patient's heart occurs. If this is the case, or if the heart is to be imaged in multiple phases of the cardiac cycle, another strategy has to be applied. With retrospective gating in CT, the image acquisition process is continued over a longer time period. Images from the respective time steps are used for reconstruction of time-varying volume data. The recorded ECG signal is used for the correct temporal context. The disadvantage of this method is that the patient is exposed to a higher radiation dose.

In order to increase the temporal resolution of a cardiac CT scan, image information from different cycles can be combined to perform multicycle reconstruction. However, this technique requires that the cardiac structures reside at the same location in corresponding cardiac phases.

Two promising technologies are expected to speed up the acquisition process even more: First, dual source CT scanners comprise two x-ray tubes instead of a single one. Second, an increased amount of 256 detector rows in future CT scanners will also decrease acquisition time. Issues which are currently related to ECG triggering and multicycle reconstruction will thus be less problematic. Temporal resolution will increase. This is especially interesting for analysis of cardiac morphology and function. The increased temporal resolution is expected to make even cardiac CT perfusion studies possible in the future [25].

## 1.2 Medical Image Understanding

Quick understanding and accurate description of features in complex medical image data are key issues in radiology. Great efforts are currently put into the development of methods that automatically extract clinically important properties from medical image data. In general the related tasks are very complex, even for the human observer. Several critical issues have to be considered:

- Large amount of data (1 GB and larger).

- Complex structure of the data (time-dependent, 3D).

- Image artifacts (motion artifacts, noise, etc.).

- High demands on accuracy and patient safety.

- Medical domain knowledge required.

Algorithms which automatically extract important high-level information from images are known to be very difficult to implement. One reason for this is that the fuzzy and complex requirements for such algorithms are hard to define. For example, a ground truth on which several experts agree is often difficult to establish.

An important issue is medical expertise: the correct interpretation of medical images requires experience and learning. Even a human observer needs to build up the necessary experience over years. This indicates that learning techniques are essential to be integrated if ever automatic medical image understanding will be realized. This thesis focusses on different aspects on how to integrate prior knowledge in order to establish intelligent image processing algorithms in the domain of medical imaging.

As a long term goal, robust automatic medical image analysis will open the door for calculation of clinically relevant properties within huge data bases of medical images. By replacing the tedious task of manual segmentation, labelling, or annotation, statistical evaluations and semantics-based browsing in huge medical image databases will be possible. It has to be underlined that the technological prerequisites for such a large-scale and largely automatic statistical analysis of medical data will not exist before the problem of automatic medical image segmentation has been solved.

In the following paragraphs some aspects of model-based image analysis are discussed. The discussion will focus on very general image models. The two key concepts of an image are considered to be shape and texture.

### 1.2.1 Model-based Image Understanding

Geometry and texture are fundamental concepts in computer graphics. While geometry is used to describe object shapes, texture is mapped to surfaces in
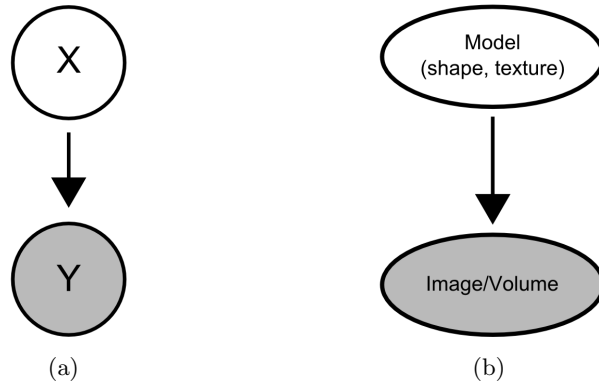
**Figure 1.7:** *The principle of Bayesian reasoning: The simplest configuration of Bayesian variables where a random variable Y depends on another variable X (a). The equivalent relationship for models of shape and appearance (b).*

order to enrich detailedness. Both shape and texture are also the main ingredients to model-based image segmentation. In literature the term *models of shape and appearance* has largely been established for statistical models which represent shape and texture [13, 59, 67].

The goal of model-based segmentation is to find out the shape of an object which is shown in a 2D image or 3D volume. This is done with the help of a model of the object of interest. The great advantage of model-based segmentation over other segmentation methods is that domain-specific knowledge about shape and texture is exploited. The input for a model-based segmentation algorithm usually consists of:

1. A model of the shape variations/deformability. The shape model restricts the outcome of the segmentation by object-dependent shape constraints.

2. A model of the texture which predicts or constrains the texture that is expected to be observed.

3. The image actually showing the object of interest.

The expected output of a model-based segmentation algorithm is purely the shape of the object of interest. It is important to note that although shape is to be calculated, the observed image contains shape only indirectly. The only information that is observed directly is an image (texture). This is a typical case of "inverse reasoning" that starts with an observation. From this observation the internal (hidden) configuration of the model is derived.

In probability theory the relation between model and observation is represented by conditional probabilities. The method of reasoning to derive

posterior probabilities of hidden model states from a related observation and prior probabilities is known as Bayesian reasoning. Figure 1.7(a) illustrates a simple Bayesian relation: The probability distribution of random variable $Y$ depends on random variable $X$ (conditional probability). $Y$ is called the *observed* variable and $X$ is called the *hidden* variable. With Bayesian reasoning one can calculate the probability distribution of the hidden variable given the observed variable and the corresponding conditional probabilities.

In figure 1.7 the example with two random variables is juxtaposed with model-based segmentation (figure 1.7(b)). For the latter an image (or volume) is observed and the most likely model configuration that produced the image is calculated.

The general strategy of most model-based segmentation algorithms is to vary the model's shape and appearance in order to make the model optimally fit to the given image. If probabilistic models are used, Bayesian reasoning or Bayesian model inference plays an important role in model matching. In chapter 5 such a probabilistic approach based on entropy optimization is introduced.

### 1.2.2   Shape Modeling

The term *shape* is frequently used in everyday language. When humans speak about an object's shape, they refer to spatial properties of the object. However, it is difficult to establish a formal mathematical definition which covers all aspects of the concept "shape".

Already Renaissance artists like Leonardo DaVinci and Albrecht Dürer were facing the problems of correct proportion when constructing portrayals of humans. Manuscripts of the time suggest that in order to draw a perfect image of a person or object, the artist has to fully understand the person's or object's proportions. In order to obtain the desired geometrical relations, Renaissance artists intensively studied proportions of the human body. Leonardo DaVinci even carried out dissections of over 30 human corpses and many animals (figure 1.8(a)) in order to gain more insight into anatomy. For DaVinci in many aspects "understanding" meant "drawing". In his conception the artist first has to study nature and absorb the proportions and colors of objects in order to later reproduce them as a painting. This philosophy seamlessly fits the model-based segmentation approach.

A very interesting turnaround in the opinion about human proportions is observed in the work of Albrecht Dürer. In the early works the artist tried to find the perfect proportions of the human body. He was convinced that there exists something like a recipe for the design of the perfect human body. After years of searching, Dürer largely switched away from this concept of a single perfect recipe of proportions. He started to try out different construction methods for different types of human bodies, e.g. the elongate, the medium, and the short female types (figure 1.8(b)). One could say that Dürer turned
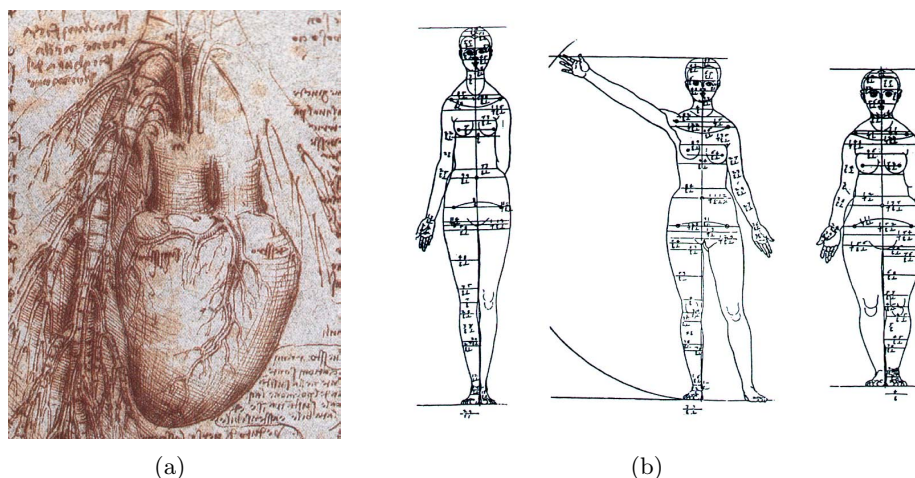
***Figure 1.8:*** *The heart of an ox drawn by Leonardo DaVinci (a). Different types of construction methods for the female human body by Albrecht Dürer (b).*

from the idea of a single perfect template to the idea of more complex models which better account for shape variation.

In computer graphics the most conventional approach to define shapes of objects is to use surface meshes that consist of simple geometrical building blocks like triangles or quads. In many applications it is not enough to define static shapes, but it is necessary to also model changes or deformations of shapes. In computer graphics, for example, modeling the deformation of tissue, hair, or clothes is important to generate realistic animations. To achieve this goal, more or less accurate physical models are usually applied [72, 2, 47].

Physical modeling is not the only approach to describe shape deformation. Variation of shape can also be modeled in terms of statistical variation. For example: Although human faces have common features (two eyes, nose, mouth), significant statistical variations in the spatial compositions may be observed for different individuals.

In medicine the shape of anatomical structures is of great interest for analysis and diagnosis. In cardiology the myocardial wall thickness, blood volumes, or diameters of coronary arteries are examples of clinically relevant properties which are derived from shape. The statistical properties of these structures are not only of interest for analyzing anatomical anomalies. Investigation of the occurring shape variations also helps to build up prior knowledge about structures. This knowledge can be re-used for intelligent application-specific image segmentation. The use of prior knowledge is especially important for medical image segmentation tasks, where even human observers have to be well-trained to perform correct segmentation.

A formal theory of shape variations is widely known as *Kendall shape spaces*. It was originally introduced by David Kendall in 1977 in a work entitled "The diffusion of shape" [30]. In this work, corresponding shapes are represented by a fixed number of particles (points). The spatial configuration of the points is considered modulo scaling, rotation and translation. Using the words of David Kendall, shape is *what is left when the differences which can be attributed to translations, rotations, and dilatations have been quotiented out.* [31]

Shape spaces are an active research topic and are interesting for different applications. In a recent work, for example, geodesics based on shape space metrics are explored. These geodesics represent paths in the shape space which correspond to well-behaving smooth deformations [32]. Deformations of the considered shapes are described as interpolation (and extrapolation) between different shapes in the shape space.

Throughout this thesis we identify the problem of finding a segmentation as *finding a shape configuration which optimally fits some given image*. This problem can be formulated with the help of shape spaces: For a given image the optimal point (shape) in the shape space is to be found which best fits the image.

In order to describe shape variability, many different approaches have been proposed. For Active Shape Models [15], a Principal Component Analysis (PCA) is applied to a number of training shapes. This is done in order to perform dimensionality reduction of the space in which the training shapes live. A Gaussian distribution of the according shapes is assumed. Different shapes are generated by linear combinations of a limited set of principal components. However, a problem arises if too complex linear combinations are performed in shape space: Self-intersections are likely to occur if shapes are reconstructed which are too far away (in shape space) from the original training shapes. Figure 1.9 illustrates this problem for a 3D shape model of the heart.

One approach to avoid self-intersections is to use diffeomorphic warps. Accordingly, diffeomorphic shape models [12] can be formulated. Although diffeomorphic warps also have the advantage of making deformations smooth, model-building is more complicated. Instead of linear interpolation of principal components, diffeomorphic warps have to be found which warp the training shapes to each other [12].

Another general restriction in PCA-based shape representation is that usually a large number of training examples is needed in order to capture the full shape variations with sufficient detail. Especially shape variations in pathological anatomical structures are critical. With $N$ training shapes the resulting maximum number of principal components is $N-1$. The number of principal components is the dimensionality of the linear shape space. For structures with complex variations the limitation to $N-1$ parameters is not acceptable.
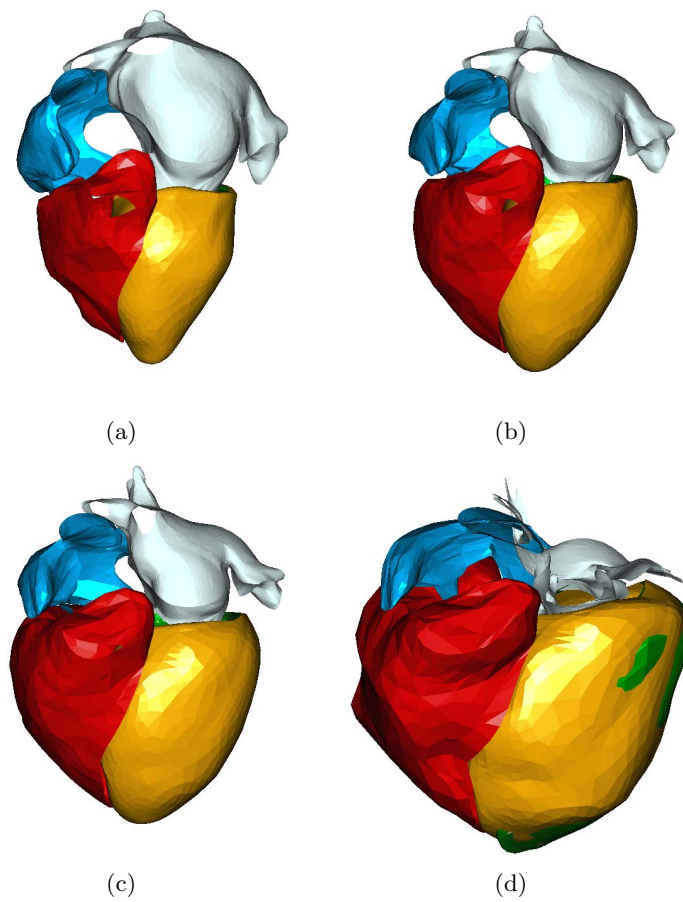
**Figure 1.9:** *Linear interpolation of shapes in diastole (a) and systole (c). The mean shape (b) (arithmetic mean) of (a) and (c). When the linear interpolation is exaggerated, self-intersections occur (d).*

Because PCA is based on the covariations of all landmarks it tends to represent mainly *global* shape variations. For the resulting segmentation this means that the rough overall shape is often found but locally the contours do not match well. The model is powerful in describing global covariances. However it is not capable of handling fine local variations which are largely independent from the global shape [16].

One approach to better account for local shape variations is to apply Independent Component Analysis (ICA) [68]. ICA aims at detecting statistically independent variations. For statistical analysis of a set of shapes, ICA tends to detect mainly local variations [68]. This indicates that in a local set of landmarks the mutual dependence of spatial variability is higher than for more distant landmarks. Although ICA seems to be better suited to model local shape variations it lacks the ability to handle global variations.

A more general way to model statistical variation of shapes at different levels of detail is to apply the statistical analysis on different resolutions and for different regions of a shape. In a work on hierarchical Active Shape Models (ASMs) [16], two approaches to subdivision of an ASM for multiresolution modeling are proposed: A simple approach is to manually split the contour into multiple segments. On the lowest level of resolution PCA is then applied to each of the centers of gravity of the individual segments. At the next finer level PCA is applied for each segment separately. The subdivision and statistical analysis can be continued recursively. In order to avoid discontinuities between the individual segments, local variations are calculated for overlapping segments and are blended continuously.

Multiresolution statistical shape modelling can be realized more elegantly by using wavelet decomposition [16, 45, 46]. This allows consistent analysis of low resolution (global) variations and high resolution (local) variations. The problem of multiple resolutions is thus elegantly solved and the statistical analysis of variations can be applied by directly using the wavelet coefficients as input to PCA.

In a work on hierarchical modelling of deformable shapes [22] a non-statistical approach is proposed. Hierarchically subdivided shape segments and their relative positions are represented by a so called shape tree. Random variations of the shape tree at different nodes which represent different levels of detail preserve the overall recognizability of the shape. In the same work a shape matching algorithm is proposed. It compares a template shape tree with curve segments that were extracted from an image.

### 1.2.3  Texture Modeling

An effective model of the gray values observed in medical images is crucial for robust model-based segmentation. In this thesis the main task of the texture model is considered to provide a basis for comparing some shape configuration (shape model instance) with an unknown image.

In order to match a model to an unknown image it is necessary to define a cost function which reflects the matching accurracy. A model matching algorithm can then be understood as an optimization algorithm which minimizes this cost. This is done with respect to the shape parameters of the model. Active Contours or snakes [29] are an early example of such an approach. The cost function originally proposed for Active Contours accumulates two terms: an inner and an outer energy. The inner energy represents the deformability of the shape and the outer energy moves the shape towards image features. In the early Active Contour approach both energy functionals are chosen in an ad-hoc fashion. For example, as image features which attract the contour, brightness or image gradients are used. Especially when textured images are investigated or images which show complex structures, the Active Contour is easily misled by gradients which do not represent the desired contours.

Alternative energy functionals have been proposed later. A popular example is the Mumford-Shah energy functional [44]. It is based on two assumptions:

1. An image varies smoothly and/or slowly over a region which represents an object.

2. An image varies discontinuously and/or rapidly across the boundaries between different objects.

A variation of the Mumford-Shah energy functional is used in a work which exploits it for evolution of level sets [10]. Although the assumptions on which this model is based are in many cases more adequate than attraction by simple gradients, it may still have problems with objects that exhibit strongly varying textures.

In order to gain more robust and more specialized texture models it is useful not to define texture properties a priori but to derive them from examples. By avoiding to make assumptions on the properties of texture it seems to be more robust and more elegant to "learn" such properties from examples for specific applications.

With the help of probabilistic and statistical methods, promising results have been achieved in many texture-related applications. If probability distributions can be derived from training textures, predictions of new unknown textures or images can be made. One very interesting application of texture modeling is texture synthesis. The goal of example-based texture synthesis is to derive a large image with stochasically varying local detail. At the same time the global visual appearance of the example texture shall be preserved. A very popular approach to this problem assumes that the probability of a pixel's color is defined by the pixel colors in a patch around it [21]. A probability distribution for different pixel colors with respect to different neighborhoods is estimated from the example texture. By drawing samples

(a)                           (b)
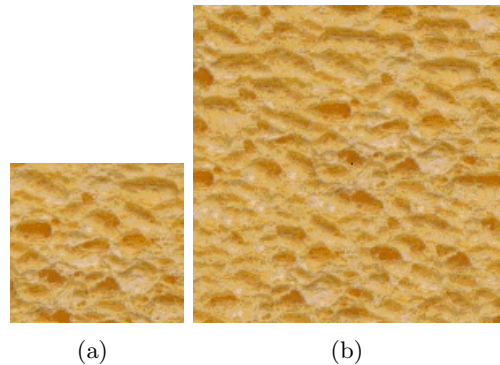
***Figure 1.10:*** *A small patch of an example texture (a) and a larger patch generated out of the example (b) (images from [21]).*

from the estimated probability distributions, incrementally a new texture is grown which looks visually similar to the example texture (figure 1.10). The outlined method is a nice example on how the estimation of probability distributions serves as a tool for predicting probabilities of pixel colors in newly synthisized textures.

A question that arises in probabilistic texture modeling is, which dependencies are assumed and how to derive reasonable estimations for probability distributions. In the above example a pixel is assumed to be dependent on other pixels within the patch. Further it is assumed to be independent from all other pixels outside the patch. The patch size influences the results significantly. It is also necessary to define a tolerance for similarity of patches in order to derive a reasonable probability distribution. A whole set of parameters has to be chosen and constraints have to be introduced in order to realize a probabilistic texture model.

## 1.3   Thesis Overview

The scope of this thesis is on model-based segmentation in medical imaging with a special focus on applications in cardiology. Methods are proposed and validated which implement general ideas of shape and appearance models in different ways.

A general problem in model-based segmentation is a reasonable initialization of the model. A very application-specific approach for this task tailored to functional MR images is proposed in chapter 2.

To increase robustness in model-based segmentation of cardiac magnetic resonance short axis images, a two-component model is proposed (chapters 3 and 4). The first component consists of multiple 2D Active Appearance Models for characteristic short axis slices. The second component models the spatial relation between the 2D models. While the first component

increases flexibility, the second component assures robustness.

The considerable random variation in medical images due to different scanners, fuzzy anatomical structures (e.g. trabeculae), and varying noise levels is a critical source of error for many segmentation algorithms. Considering statistical analysis of a training set helps to cope with such variations. In order to increase robustness, an information theoretic approach to probabilistic texture modeling is proposed. Chapter 5 shows how the optimization of information entropy increases the model's generality while keeping the loss of specificity minimal.

Empirical validation of algorithms for medical image analysis is very important. Currently the scientific community is attempting to introduce standards for validation similar to those which are already in use for pharmaceutic products. In chapter 6 an automatic approach to centerline extraction of coronary arteries is presented. The method is based on principles of model-based segmentation. Results were validated within a workshop at the MICCAI conference. The method performed best in a direct comparison with four other automatic centerline extraction algorithms.

# Chapter 2

# Automatic Detection of the Heart in MRI

## 2.1  Introduction

Segmentation of cardiac structures from magnetic resonance images (MRI) has been of great interest in the medical imaging community [56, 62, 39, 69]. The great advantage of model-based segmentation is that it incorporates prior knowledge about the segmented structures.

Active Appearance Models (AAMs) [14] are deformable models which describe possible configurations of shape and gray values by statistical analysis of a training dataset. Several authors have proposed the use of AAMs and their numerous extensions to the problem of segmentation of cardiac structures. Methods proposed so far comprise 3D AAMs [42], temporal AAMs [39], and 3D+time AAMs [62].

A concrete instance of an AAM is defined by parameters comprising: position, scaling, orientation, shape and texture parameters. Matching the model to unseen data is equivalent to finding a configuration of parameters that optimally fit the model to the unseen data. The common proceeding is to place the model onto unknown image data. Then deformations are iteratively applied until a difference measure such as root mean square (RMS) texture difference reaches a minimum. A problem often ignored in literature is robust and fast automatic initialization of the model, i.e. finding reasonable initial position, orientation and scaling. A brute-force method iteratively tries out each and every configuration. However this is very time-consuming since the number of possible initializations is huge. In previous work it has been suggested to perform AAM Search in parallel with multiple different initialization parameters [58]. However, this approach is quite time consuming, especially when dealing with 3D AAMs. To utilize AAM-based segmentation for cardiac cine MR in daily clinical practice, a more efficient method for initialization is required.

Recently a method based on sparse Markov Random Fields (MRFs) [20] has been proposed for fast initialization of model-based segmentation. However this method relies on feature extraction which is not proven to deliver adequate results on cardiac cine MR data. Furthermore the run times reported for solving the considered MRF are in the order of a few seconds while the method we present in this chapter delivers the result after about one second.

This chapter presents a method that automatically determines the initial position parameters for an AAM for segmentation of the human heart in MRI short axis data. In earlier work Sörgel and Vaerman [56] have introduced a method for automatic heart localization for initialization of Active Contours. The presented work extends this approach. Instead of initializing Active Contours, the goal of the method proposed in this chapter is to initialize an Active Appearance Model. A set of well-established image processing algorithms is used including morphological operators [54] and Hough-transformation for circles [17]. In contrast to previous work where

Fuzzy Hough-transformation [49] was applied to detect the left ventricle [48] we propose to perform Hough-transformation directly on gray values as will be outlined later in this chapter.
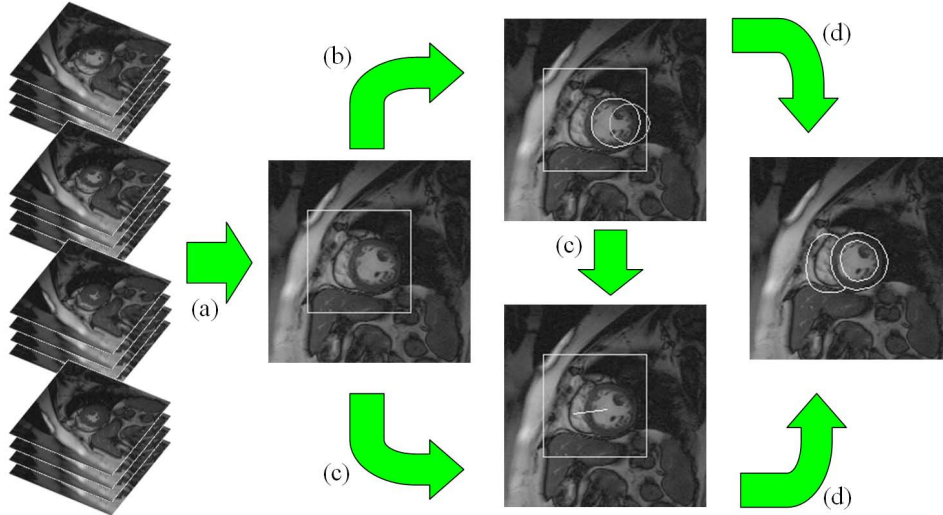


**Figure 2.1:** *The pipeline: ROI extraction (a), LV localization (b), LV-RV orientation (c), model-based candidate selection (d).*

This chapter is organized as follows: In section 2.2 an overview of the investigated MRI data is given. The fully automatic method for localization of the heart is described in detail in section 2.3. Validation and results are presented in section 2.4 and the chapter concludes with section 2.5.

## 2.2 Data

The 4D data considered in this chapter consists of cine MRI short axis studies of 42 different patients. The data was captured using two MR scanners from different vendors each operating at a magnetic field strength of 1.5 Tesla. Each short-axis study consists of 7 to 13 slices with pixel resolutions ranging from 1.17mm to 1.68mm. The spacing between slices ranges from 7.2mm to 12.0mm. Time-resolution lies in the range of 11 to 27 time steps per patient study.

## 2.3 Method

Our method takes into account the complete four-dimensional (3D + time) input data and computes the initial parameters for the model: position,

orientation and scale-factor. The pipeline is made up of four steps (see figure 2.1):

- Extraction of the region of interest (ROI)

- Localization of the left ventricle

- Calculation of LV-RV orientation

- Model-based candidate selection

In each step elementary digital image processing algorithms are used. This makes the method transparent, comprehensible, and easy to implement. In the following the individual steps of the algorithm are explained in detail.

### 2.3.1 Extraction of the Region of Interest

In order to limit more complex calculations to a restricted ROI, the first step is a detection of the image area which contains the heart. Over the period of the cardiac cycle, position and size of the heart vary due to contraction of the myocardium. As a result the strongest variations of gray values appear in the region inside the heart. The localization is based on these variations of gray values over time similarly as proposed by Sörgel and Vaerman [56].

For every slice a variance image is calculated. The gray values of a variance image correspond to the variance of the according pixel over the complete cardiac cycle. High gray values indicate strong variance and thus the according pixels belong to the heart region with high probability. Figure 2.2 shows examples of such variance images for different slices of a single dataset.

It has to be considered, especially for MRI data, that high variance of a pixel's gray value might possibly come from noise or imaging artifacts. To reduce the disturbing influence of noise, the following image processing steps are carried out for the individual variance images. A threshold is selected such that the according number of pixels above the threshold approximately cover the area of the heart (roughly $10000mm^2$).

To eliminate single pixels and small pixel areas a morphological cleaning is applied to each variance image. The morphological structuring element that is used is a $5 \times 5$ mask centered over the considered pixel. If less than 11 pixels in this mask are set the pixel is unset. If more than 15 pixels are set the center pixel is set. Otherwise the old pixel value is kept.

This improves the results significantly but in some cases there still remain misleading pixels set. To increase robustness all masks from all slices are considered jointly. A new mask is generated by summation of the individual variance images. This gives a result as depicted in figure 2.3(a). Outliers where misleading variances appear in individual slices only are removed with the following operation: All pixels which are set in less than 25% of all slices
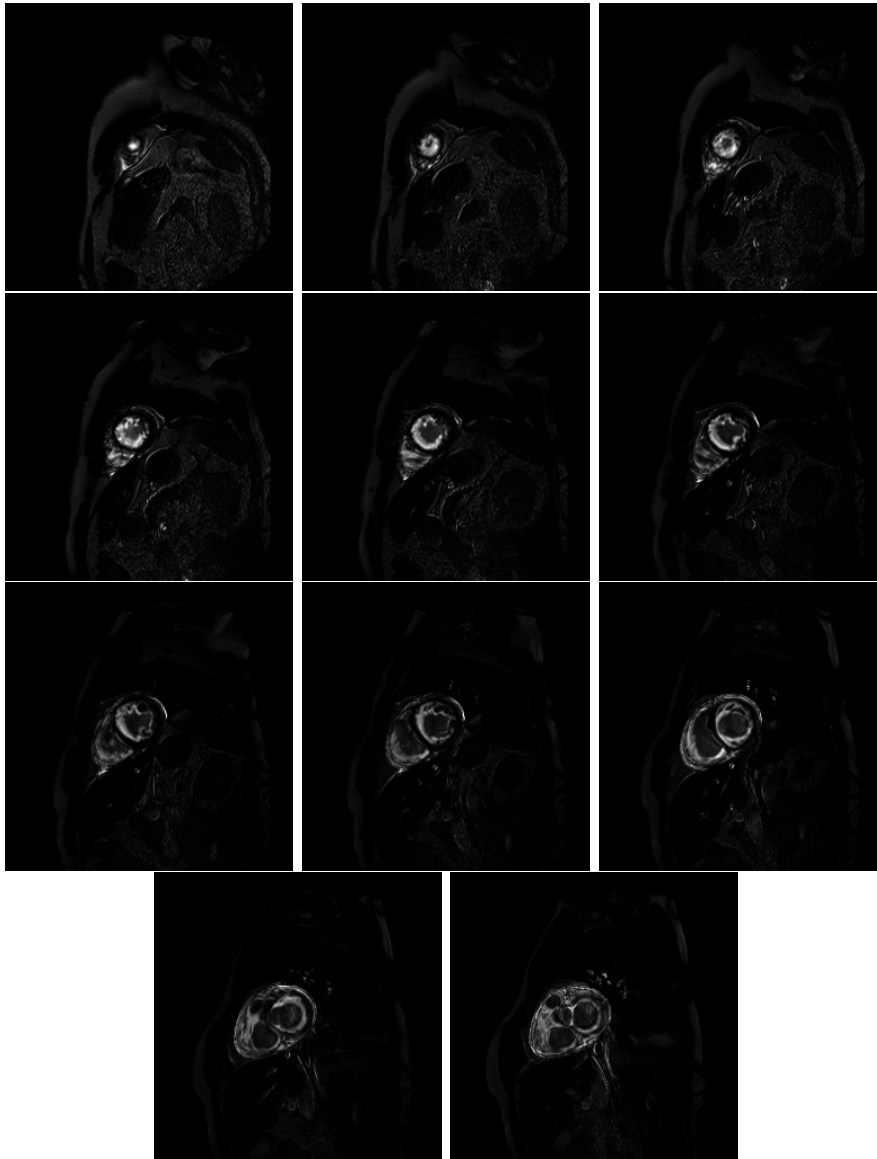
**Figure 2.2:** *Variance images for individual slices of a single dataset.*

are deleted. Figure 2.3(b) shows an example of the outcome of this step. To further reduce artifacts only the largest connected region in the mask is considered (figure 2.3(c)). A bounding box around it defines the ROI as shown in figure 2.3(d). Since information from different time steps and different slices is combined it is argued that the resulting mask robustly identifies the region of the heart.
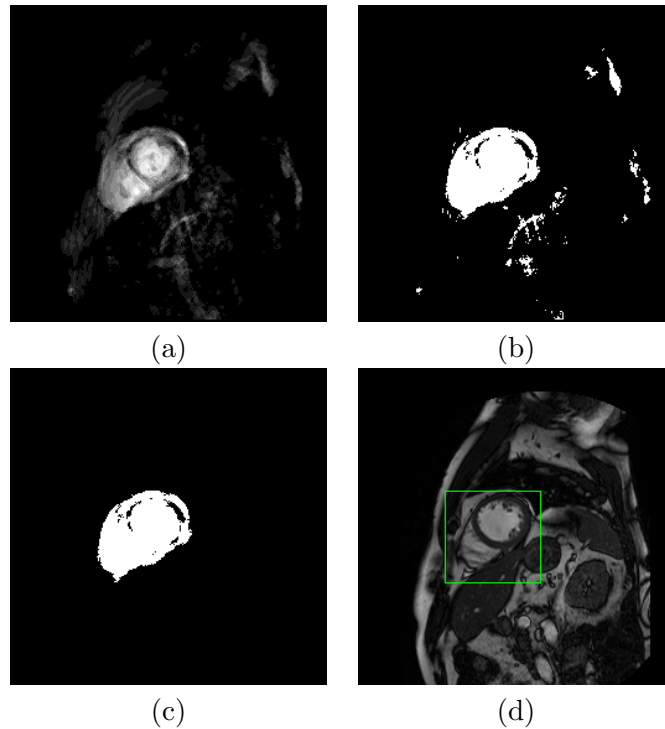
***Figure 2.3:*** *Towards the ROI: Sum of variations (a), thresholded (b), largest region extracted (c), and resulting bounding box (d).*

### 2.3.2   Localization of the Left Ventricle

While the first step in the algorithm takes the full 4D data into account the rest of the algorithm is performed on the central slice of end-diastole only. The end-diastole is typically known since the individual time steps are delivered as volumes sorted by time, starting with the end-diastolic volume. Since the captured volume typically covers the left ventricle from apex to base, the center slice of a volume is taken for further refined localization of the heart.

The myocardium of the left ventricle has approximately the shape of a circle. This fact motivates the use of a Hough-transformation for circles [17]. To reduce the computational burden the Hough-transformation is restricted to the ROI calculated in the previous step.

Typically the first step in Hough-transformation is edge detection. In the experiments carried out on cardiac MRI data it turned out that standard edge detection algorithms like Canny Edge Detection [6] give very poor results for many data sets. On the one hand this is due to properties of MRI data. On the other hand fuzzy anatomical structures such as papillary muscles and trabeculae make it very difficult to calculate meaningful image

26

gradients that clearly represent transitions between objects. Furthermore in experiments it was observed that gray value distributions for MRI images fluctuate significantly in inter and even intra patient studies. This makes it very hard to select generic parameters for an elaborate edge detection algorithm.

More elaborate approaches like Fuzzy Hough-transformation [49] try to circumvent the problem of structures deviating from perfect circles. Anyway the problem of strongly misleading edges in the region of papillary muscles remains.

In order to overcome the problems of edge detection, the Hough-transformation is adopted to take original gray-values rather than edge information as input. The assumption is made that gray values of the myocardium are significantly darker than those of the blood inside the ventricles. Thus, for transforming the image into Hough-space low gray values in the image are assumed to belong to the myocardium with high probability. Using this approach the detected circle does not lie on the boundaries of the myocardium but somewhere in between. As a result the circle is detected robustly even if the shape of the left ventricle deviates from the perfect circle. Compared to the Fuzzy Hough-transformation the computational complexity is even reduced (no gradient calculation is required). Note that the even darker gray values in the lung region were excluded since they lie outside the previously calculated ROI.

The Hough-space considered is a three-dimensional space of parameters. Its axes are $x$, $y$ (position of the circle's center) and $r$ (radius of the circle). $x$ and $y$ are constrained by the bounding box defining the ROI. $r$ is restricted to an interval of 25mm to 40mm – a typical range of radii for left ventricles.

Although Hough-transformation as we have described it works quite robustly there is still a small chance that the highest evidence for a circle is not correctly describing the left ventricle. Our experiments showed that the correct contour of the left ventricle always corresponds to one of the first two largest peaks in Hough-space. Thus the first two most prominent candidates for position and scaling of the left ventricle are considered at the last stage of the algorithm.

### 2.3.3 Heart Orientation

From previous steps two possible candidates for the left ventricle are extracted. Each of these candidates is described by position and size of the two Hough circles. What remains is to determine the *orientation* of the heart, i.e. where the right ventricle is located relative to the left ventricle.

The ROI computed in section 2.3.1 is thresholded such that the 20% brightest pixels remain. As experiments showed, the two largest connected regions robustly correspond to the blood inside left ventricle and right ventricle. The centroids of these regions already indicate the spatial relation

between the ventricles. It is however not known which region corresponds to the left ventricle and which to the right one. To resolve this ambiguity the region with its centroid closer to the center of a Hough candidate is identified as the left ventricle. This way a unique orientation is assigned to both Hough-candidates.

### 2.3.4 Model-based Candidate Selection

The preceding steps reduced the initialization search space from millions (possibly every pixel with multiple different orientations) to two candidates: two Hough circles for the myocardium of the left ventricle together with estimates of LV-RV orientation. Each of the two candidates defines position, scaling, and orientation for a possible initialization of the model.

To select the optimal candidate the root mean squared (RMS) texture errors between model and both initialization candidates are calculated. The candidate which produces the smaller error is identified as the final result.

## 2.4 Validation and Results

The method has been evaluated for a total of 42 MRI studies. Automatic initializations have been compared to manual ones: Five users interactively initialized the model. To assess the quality of the automatic method three figures of merit have been evaluated: average point-to-surface distance, texture error, and time performance.

The average point-to-surface (PTS) distance is calculated for the manually and automatically placed mean model shape relative to the accurately done manual ground truth segmentation. This was only possible for a subset of 31 datasets where ground truth segmentation was available. Figure 2.4 (top) summarizes PTS measures achieved by users and the automatic method. It is observed that automatic initializations come close to the manual ones. Please note that the average discrepancy of 6mm only refers to *rigid* initialization of the *mean* model. In this chapter only initialization is investigated – no subsequent deformations of the model are applied in an attempt to achieve final segmentations.

In order to evaluate initializations for which no ground truth was given, the texture difference between mean model and image data was determined. Figure 2.4 (middle) shows the quality of matches for all (unsegmented) 42 datasets after manual/automatic initializations with respect to texture difference. It is again concluded that the automatic method generates initializations qualitatively comparable to those of the users. The final results – the initializations – for all validation datasets are visualized in figure 2.5 for the central slices of end-diastole.

While similar in quality, figure 2.4 (bottom) proves another advantage of the automatization over user interaction – the speed-up. The average

**Average point-to-surface distance**

| | |
|---|---|
| User 5 | 6.18 |
| User 4 | 6.40 |
| User 3 | 6.30 |
| User 2 | 5.97 |
| User 1 | 5.76 |
| Automatic | 6.49 |

millimeters

(a)

**RMS texture error**

| | |
|---|---|
| User 5 | 21.0% |
| User 4 | 22.1% |
| User 3 | 21.6% |
| User 2 | 21.5% |
| User 1 | 21.8% |
| Automatic | 21.1% |

% of gray-level scale

(b)

**Time performance**

| | |
|---|---|
| User 5 | 9 |
| User 4 | 13 |
| User 3 | 23 |
| User 2 | 15 |
| User 1 | 47 |
| Automatic | 1 |

seconds

(c)
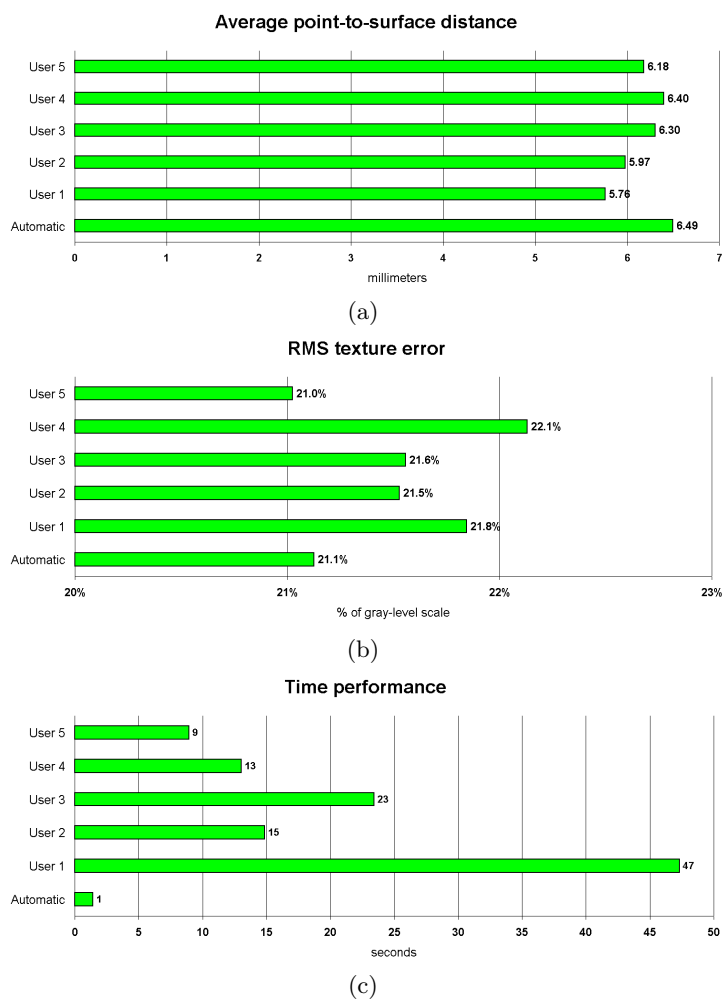
**Figure 2.4:** *User study at a glance: Averaged point-to-surface distances for 41 datasets (a), RMS texture errors for all validation datasets (b), and time performance for all validation datasets (c).*

initialization time of 1 second has been achieved by a Java implementation.

## 2.5 Conclusion

This chapter has introduced an automatic and robust method for localization of the left ventricle and right ventricle in 4D cardiac MRI data. The method has been designed with the help of few elementary image processing operators. The Hough-transformation for circles was adapted to operate on original image gray values instead of gradient magnitudes. This makes the detection of the left ventricle highly robust. The overall quality of initial-

**Figure 2.5:**   *The result: Initialization of the AAM's mean at the central slices.*

ization has been assessed by a user study. Time performance of the method indicates a high potential for daily clinical use.

# Chapter 3

# Two-component Statistical Model of the Heart Ventricles

**This chapter is based on the following publication:**

## 3.1 Introduction

Correct segmentation of the left ventricle in cardiac MR short-axis images is very important for further diagnosis of the heart's function. Manual segmentation is very time-consuming and therefore efforts are made to automate this process to the largest possible extent.

Although variants of Active Appearance Models (AAMs) [14] have been applied to this problem [74, 62, 43, 42], a robust and completely automatic segmentation still poses a challenge.

Several problems appear in the context of shape- and appearance-based modeling of the left ventricle:

- The appearance of papillary muscles and trabeculae varies irregularly from patient to patient. Especially in slices close to the heart's apex these fuzzy anatomical structures are hard to model statistically. The necessary requirement for building an AAM – that the underlying training data has a Gaussian distribution – is not satisfied in the apical/apex region.

- Often, only a part of the left ventricle is captured. Training data consisting of poorly corresponding volumes decreases the quality of the resulting model.

- Respiratory-induced motion introduces shifts of neighboring slices and so leads to irregular local variances in the data.

- Principal Component Analysis (PCA) involved in the build leads to a model where variances apply to the complete model. This makes it hard to handle local variations, e.g. different brightness of individual slices.

In this chapter we propose a new and robust approach to segmentation of the left ventricle. By linking a set of 2D AAMs with a 3D shape model we perform model matching at a global and local context iteratively. With this approach we handle the above list of problems.

This chapter is structured as follows. In section 3.2 we review related work on statistical models of shape and appearance in context of left ventricle segmentation. In section 3.3 we introduce a two-component model of the left ventricle. In section 3.4 we outline how the two-component model is matched to unseen data. Results are presented in section 3.5 and a conclusion is drawn in section 3.6.

## 3.2 Statistical Modeling of the Left Ventricle

Our approach benefits from the combination of both Active Shape Models (ASMs) [15] and Active Appearance Models (AAMs) [14]. ASMs are statis-

tical models of shape that can be used for identification and segmentation of known objects in unknown images. AAMs are a direct extension of ASMs and incorporate not only information about shape but also model the underlying texture. Variations of both methods have successfully been applied to segmentation in medical imaging [43, 4, 65].

Statistical models of shape and appearance are created from a finite number of training datasets. In other words, the model is only able to represent and thus segment new datasets that are similar to the ones in the training set. Increasing the size of the training set is a rather limited way to improve the generalization ability of the model. By adding local deformability the generalization ability can be increased explicitly. The statistical model is used to find a rough initial segmentation which is refined by restricted local deformations [65].

Several authors have discussed local and global deformability of a model. Independent Component Analysis (ICA) [68, 63] leads to modes of variation which have a rather local effect compared to the global modes of variation derived from the conventionally used PCA. To deal with local variations of a model it can explicitly be split into sub-models. The split is achieved either with the help of human expertise or by means of optimization based on the Minimal Description Length (MDL) [38].

A great problem that arises in segmentation of short-axis MRI images of the left ventricle is respiratory-induced motion. Such artifacts appear as slight displacements of spatially neighboring slices. Handling of these displacements is crucial to achieve both a correct model and correct segmentations. A recently proposed approach [61, 60] first detects the left ventricle in one or multiple slices. In a second step image alignment is used to compensate the shifts of neighboring slices. Finally a 3D AAM search is performed to achieve the final segmentation.

## 3.3 A Two-component Model of the Left Ventricle

Inspired by the idea of modeling global and local features separately [38, 65] we propose to combine a set of local 2D AAMs with a global 3D shape model. The purpose of the 2D AAMs is to precisely match the well articulate slices of the heart's base. The purpose of the 3D shape model is twofold: to propagate the position and size of the basal slices to apical ones and to keep the global shape characteristics plausible. In the following we describe the two components of our model.

### 3.3.1 Component 1: A Set of 2D Active Appearance Models

In a first step we consider the given training data, i.e. texture and annotation, slice-wise. From base to apex we identify the following four classes of slices:

(a)        (b)        (c)        (d)
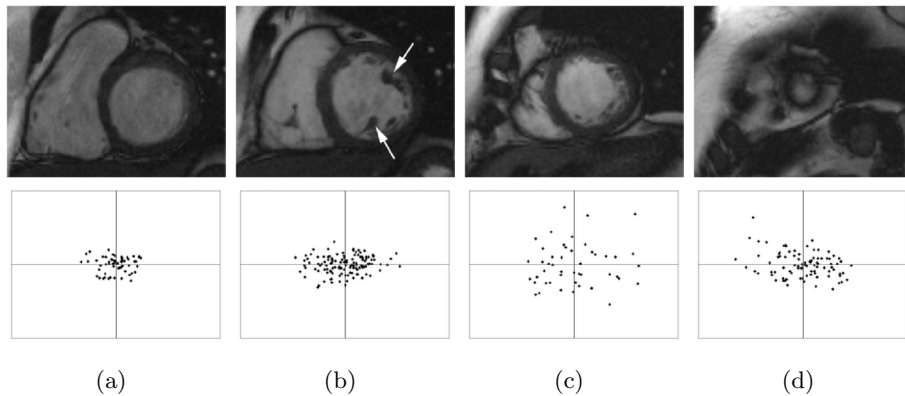
***Figure 3.1:*** *Typical examples of basal (a), mid (b) (the arrows indicate papillary muscles), apical (c), and apex slices (d) (top) and the first two principal components of texture after PCA (bottom).*

**Basal slices** (figure 3.1(a)) reside close to the base of the heart and do not contain papillary muscles.

**Mid slices** (figure 3.1(b)) clearly show papillary muscles (arrows).

**Apical slices** (figure 3.1(c)) contain trabeculae and papillary muscles, which are represented by irregular texture.

**Apex slices** (figure 3.1(d)) show the very apex of the heart and contain highly irregular texture.

We performed PCA on the shape-normalized texture vectors of all slices in the training set. Scatter-plots of the first two principal components are shown in figure 3.1 for the according classes of slices. We observe that basal and mid slices show a relatively compact Gaussian distribution and are thus well suited for linear statistical modeling using PCA. This is not the case for apical and apex slices, whose texture is much more irregular.

With a manual classification of slices we build a set of four individual 2D AAMs. This proceeding has the advantage that even incomplete MRI datasets can be included in the training set and used for building the first component of the model.

### 3.3.2   Component 2: A Global Shape Model

The intention of the global model is to represent the ventricle's shape in an overall simplified way. Its task is to assure a valid relative placement and scaling of the four 2D AAMs.

The core of the global model is a centerline connecting the 2D AAMs in 3D. For the landmark points of each slice of the annotated training set a
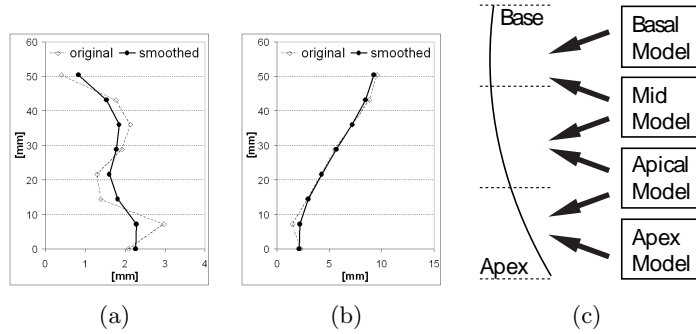
Figure 3.2: *The original and smoothed centerlines projected to XZ (a) and YZ (b) plane. (c) The assignment of sub-models to sections of the global shape model.*
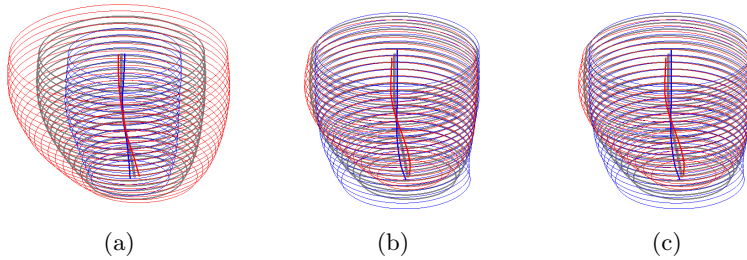


Figure 3.3: *The first (a), second (b), and third (c) modes of variation of the global shape model. The plots show the mean shape together with the largest possible deformations.*

centroid is calculated. The assembly of these centroids forms the centerline. Figures 3.2(a) and 3.2(b) show such a centerline for one of the annotated datasets. It can be seen that respiratory-induced shifts of neighboring slices appear in the data. We use a Gaussian filter to smooth the centerlines and to reduce respiratory motion artifacts in the training set.

Additionally to the centroids we incorporate the radii of slices into the global model. For each slice a radius as the mean distance of shape points to the centroid is calculated. This results in three variables that approximately describe the ventricle's shape on one slice: x/y-coordinates and radius.

To build a statistical shape model, an equal number of corresponding landmarks has to be placed in every training example. We interpolate centroid positions and radii to get a total of 20 evenly-spaced slices. With the three features per slice this results in a total of 60 features included in the global shape model.

Before PCA can be applied, the individual training examples have to

be aligned. Since we model not only the positions of centroids but also the radii we can not directly apply 3D Procrustes analysis. We rather align the center lines with respect to x/y-coordinates. The radii are thus not affected by the alignment. Figure 3.3 illustrates the first three modes of variation of the global shape model.

### 3.3.3 Combining Local Models and Global Model

In order to benefit from both components the local models have to be linked to the global model. As some datasets are delivered without apex or basal slices, we compensate this missing information by attaching two 2D AAMs to each slice. For example, the top most slice is assigned the basal model and the mid model. The better matching model is kept while the other one is ignored. Figure 3.2(c) shows the assignment of 2D AAM sub-models to the global shape model.

## 3.4 Matching the Two-component Model

In the previous section we have outlined the idea of splitting a statistical model of the left ventricle into four parts and described how these parts are coupled over a global model. In this section we explain how the model iteratively is matched to unseen data.

### 3.4.1 Matching the Local Sub-models

We switch between two alternating steps. First a local matching of 2D AAMs is carried out for individual slices by standard AAM search [14]. In theory it should be possible to match all 2D AAMs in this way to get a valid global segmentation. While a valid match is obtained in basal and mid areas the 2D AAM search very often fails in the apical and apex slices. This is where the global model comes into play.

### 3.4.2 Updating the Global Model

Using the global component we propagate information from the better fitting slices to badly matching slices: The root mean square (RMS) texture error is calculated for all slices and the best 80% are used to update the global shape model. The shape update is done analogously to ASM search [15]. The only difference is that the model is not directly attracted by image features. Instead it is driven by the local 2D AAMs.

### 3.4.3 Iterative Global and Local Matching

After the global model has been updated the local AAMs are aligned to it. The search proceeds iteratively switching between 2D AAM search and

update of the global model. In this way divergence due to bad initialization in critical slices is avoided and the overall segmentation gets improved. The loop of 2D and 3D updates is repeated until convergence.

The resulting segmentation still suffers from the lack of local variability. Further improvements are achieved performing additional 2D AAM search steps with position updates restricted by a constant maximum displacement.

Finally respiratory-induced shifts are compensated. The slices are shifted such that the centroids of the 2D AAMs align to the global model's centroid coordinates. Compared to the work of Stegmann [61] our motion compensation thus benefits from prior knowledge that is encoded in the global shape model.

## 3.5 Results

We evaluated the described method with a set of 32 different short-axis studies. The quality of segmentation achieved with the two-component model was compared to that of 3D AAMs. Leave-one-out tests for all of the 32 datasets were performed. The average point-to-surface error (PSE) with respect to expert annotation was used to validate the segmentation quality. Figure 3.4 illustrates the measurements. Although the two-component model led to slightly worse results in 14 cases out of 32, the overall PSE got improved from an average of 2.20mm (3D AAM) to 1.96mm (two-component model). Even though the average improvement by 0.24mm does not sound impressive, we emphasize that compared to the standard 3D AAM the two-component model performs better by 11%.
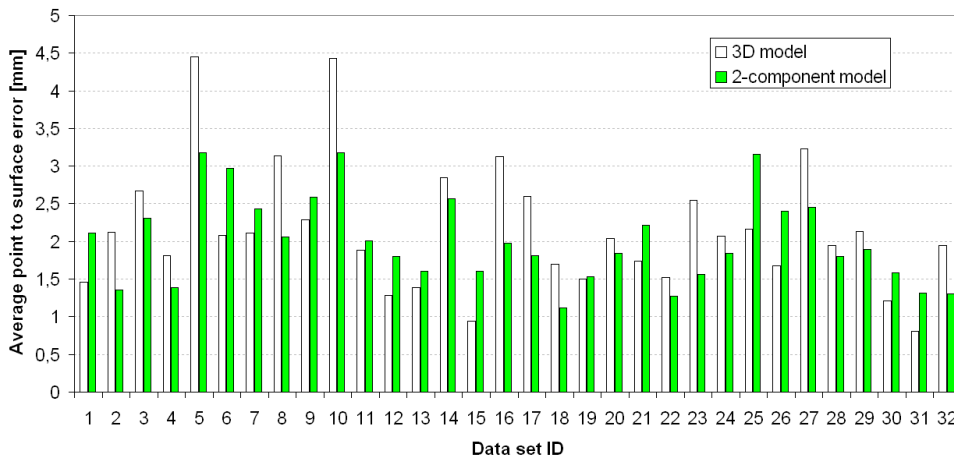


**Figure 3.4:** *Point-to-surface error measured in leave-one-out tests for all training datasets.*
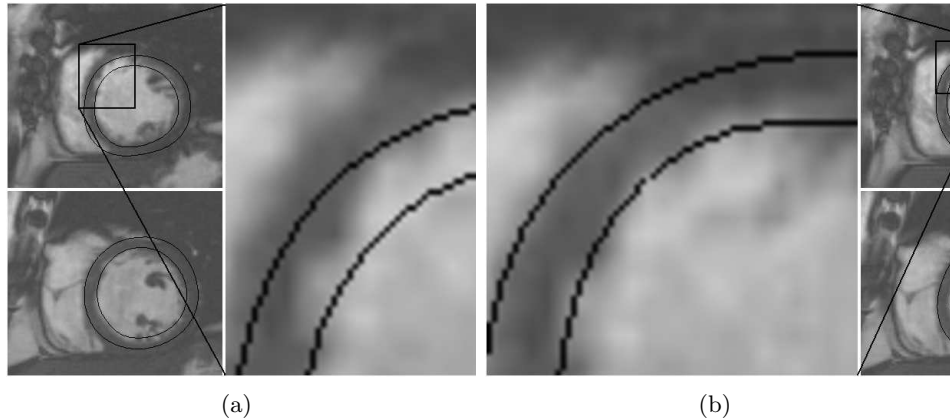
**Figure 3.5:** *Results of matching dataset 10 with 3D AAM (a) and two-component model (b).*

In figure 3.5 we provide a visual comparison for the largest improvement in terms of the average PSE which could be achieved for dataset 10. It shows the result obtained with a standard 3D AAM (figure 3.5(a)) and the improved segmentation achieved with the two-component model (figure 3.5(b)).

Figure 3.6 demonstrates the motion compensation performed with the two-component model. A section of dataset number 10 is depicted in figure 3.6(a). Figure 3.6(b) shows the dataset after matching and aligning the slices to the centerline of the global shape model.

Between 10 and 20 iterations are necessary for the two-component model matching algorithm to converge. The whole segmentation process typically takes a few seconds on standard PC hardware.

## 3.6 Conclusion and Discussion

We have introduced a new approach to 3D segmentation of the left ventricle from short-axis MR images by interconnecting a set of 2D AAMs with a simple 3D shape model. The two-component model is more robust than a 3D AAM since local irregularities such as respiratory-induced motion and different intensities of gray values in individual slices can be handled.

(a)  (b)
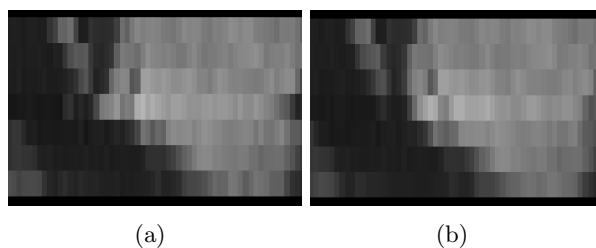
**Figure 3.6:** *Motion compensation of dataset 10 carried out by the two-component model. A cross section through the original volume (a) and the automatically corrected volume (b) are shown.*

Incomplete training datasets that do not contain the entire left ventricle from base to apex pose a severe problem for 3D AAMs. If such datasets are present in the training set the correspondence between them is ill-posed. The outcoming model allows for shrinking within its modes of variation. The topmost or the bottommost slices thus often remain unsegmented. This disadvantage is avoided with the two-component model which allows the use of incomplete datasets as training examples. Since slices are assigned to individual 2D AAM sub-models even a single annotated 2D short-axis slice can be added to the training set. As the two-component model attempts to match two neighboring 2D AAMs to each slice, segmentation of datasets that do not cover the entire left ventricle is still possible.

We are convinced that the idea of combining different types of models over a global shape model is promising for other medical segmentation problems. Especially if local anatomical abnormalities (e.g., a tumor) appear, models consisting of multiple components will likely lead to more precise results.

# Chapter 4

# Extended Two-component Statistical Model

## 4.1 Introduction

Magnetic Resonance (MR) Tomography is a very important imaging technique for assessing the function of a patient's heart. An MR study of a single patient typically includes several hundred images. For medical diagnosis it is necessary to enrich the captured data by segmenting the images. Since manual segmentation of large amounts of images is a very tedious task many research efforts are put into the development of algorithms for automatic segmentation of cardiac structures. Many of the implemented approaches use some kind of atlas or template exploiting prior knowledge about the structures of interest.

Several authors have proposed methods based on the popular Active Appearance Model (AAM) [14] including extensions to 3D [42], 2D + time [55], or 3D + time [62]. In this chapter the previous two-component model [76] which is also based on AAMs is extended and its integration into a software tool for heart function analysis is reported. The software system presented here provides automatic segmentation and subsequent display of important data such as wall-thickening and ejection fraction. Based on the geometry derived in the segmentation stage a precise medical diagnosis may be performed.

## 4.2 Data

MR studies frequently include multiple time-triggered series of short axis images. Each series consists of about 20 images taken at intervals of typically 50ms over the full heart cycle. Multiple series (typically between 7 and 13) are captured to get a stack of series. The gap between slices is about 7mm.

With a time resolution of about 20 samples and a stack size of about 10 slices, this results in a total of 200 images for a single patient. Relevant features such as thickening of the myocardium, myocardial mass and the volume of ejected blood are of great interest. Such information is not directly available from the raw MR images. In fact it is possible to calculate and display interesting features only when the according segmentation of the myocardium is provided. Manual segmentation of 200 images is very time-consuming and tiring. In order to speed up and improve diagnosis fully automatic segmentation is thus highly desirable.

## 4.3 Methods

The following paragraphs describe the individual steps of the workflow provided by the presented software tool. The complete workflow was integrated into a commercial software package for medical image analysis.

### 4.3.1 Motion Compensation

Series of individual slices are captured one after the other. If the patient moves during the capturing process the slice stacks show significant shifts of neighboring slices. To compensate for these artefacts our software provides automatic motion compensation. The key idea is to perform a comparison of short axis images with long axis images. Long axis images are approximately perpendicular to short axis images. Grey values along the intersection lines of long and short axis images are considered. Based on some similarity measure an optimal compensating shift can be calculated. Previously Normalized Mutual Information (NMI) was proposed as similarity measure for alignment of long- and short axis volumes [36]. We implemented root mean squared texture difference, mutual information, and overlap of gradients as similarity measures. Tests showed that motion compensation based on gradients was most reliable. The relatively bad results we achieved using NMI might be due to the fact that our data came with only one or two long-axis views per patient. We suppose that NMI is not robust on such sparse data.

### 4.3.2 Automatic Model Placement

For the actual segmentation process a good initial placement of the model is needed. To achieve a correct localization we extended an existing approach[56]. First the variances of individual pixels are analyzed over time. The resulting variance images are integrated, thresholded, and cleaned. A bounding box over the resulting region with largest variances is determined. Inside this bounding box the two largest connected regions are determined. They correspond to the inner regions of left and right ventricles. The line connecting the centroids of these two regions indicates the orientation of the heart. Using a circular Hough transform we determine the position of the left ventricle (which has an approximately circular shape). For some datasets the left ventricle might not exhibit the strongest evidence for a circle in Hough space. However, the correct candidate is always among the first few. To choose the optimal candidate we calculate cross-correlation with an Active Appearance Model in the central slice of the dataset.

### 4.3.3 Model-based Segmentation

Several authors have proposed different methods for splitting shape models into parts. These approaches have been shown to be very fruitful [16, 76, 38]. In this chapter we extend the recently introduced two-component model [76]. This model was originally designed for the left ventricle only. It consists of two components: a set of 2D Active Appearance Models and a global shape model connecting the 2D AAMs. In this chapter we propose two important extensions of the two-component model:
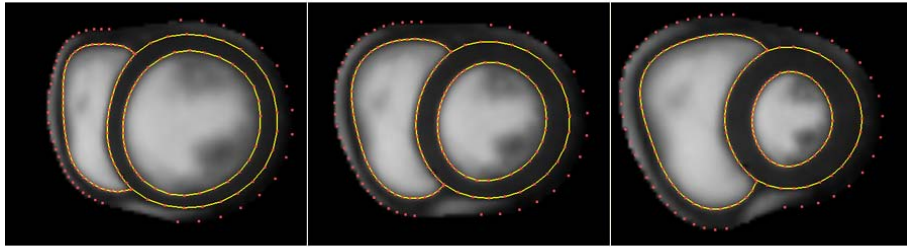
**_Figure 4.1:_** _The first mode of shape variation for a 2D AAM of a mid slice._

- The right ventricle is added. For the set of 2D models this means that additional landmark points outlining the right ventricle's border are added. Figure 4.1 shows the first mode of shape variation for a 2D AAM describing a mid slice.

- Segmented datasets from end-systole are included in the training set as well as datasets from end-diastole. The resulting model very well shows the heart's contraction as individual modes of variation and is able to interpolate time steps between end-systole and end-diastole.

While the second extension is relatively straight forward, adding the right ventricle makes some structural changes of the global shape model necessary. In the original version the global component consisted of three variables for each slice: Position of the centroid in x and y and the average radius. Now we add a fourth variable to the global model describing the relative position of the right ventricle.

In an intermediate step the centroid of the right ventricle's contour is calculated. An angle between the centroids of left and right ventricle can now be calculated. This angle is the fourth variable which we add to the global model. Figure 4.2 illustrates the first mode of variation (the first principal component) of the global shape model. The dark black points represent the centroid positions of the left ventricle. Since the landmark points are placed more densely on the border between left and right ventricles the centroids are not located exactly in the left ventricle's center. The black lines point from the left ventricle's centroid towards the right ventricle's centroid. The lengths of these lines indicate the scaling for the according 2D AAM. The first mode of variation of the global shape model clearly reflects the contraction of the heart.

Model matching proceeds very much in the same way as for the original two-component model: iteratively the 2D AAMs and the global shape model are updated. Starting at the end-diastole the model is matched to each time step. At any step the result from the previous step is copied. Under
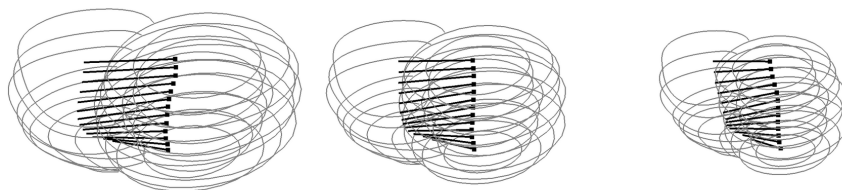
***Figure 4.2:*** *Modes of Variation of the global shape model (center: mean, left and right: positive and negative standard deviation of the first mode of variation). For better comprehensibility the according mean shapes of the 2D AAMs are shown in light gray.*

the assumption that the heart does not contract or relax too abruptly this ensures that the model converges quickly at each time step.

### 4.3.4 Manual Inspection and Correction

After the automatic segmentation has been done our software offers the possibility to inspect the segmentation and correct it, if necessary. The contours of the heart are displayed on the individual slices. The user can correct boundaries using snakes, splines or circle-shaped interpolation.

### 4.3.5 Analysis and Diagnosis

The final step in the workflow is to derive important medical information from the extracted boundaries of the myocardium and perform a diagnosis. Our software provides a 3D rendering of the contours which can be displayed as an animation over time. Furthermore a bull's-eye illustrating the dynamics of myocardial wall-thickness and statistics such as the volume of blood contained in the left ventricle are displayed.

## 4.4 Results

The software has been tested with CMR studies of 45 different patients from scanners of two different vendors. Although our model was built from training datasets of only two time steps it could well generalize to all time steps.

## 4.5 Conclusions

Robust automatic segmentation is very important for effective analysis of MR data in cardiology. We have discussed a new approach to segmentation of the left and right ventricles of the heart. The core of our method

is an extended bi-temporal two-component model including both ventricles. Our software system supports the complete workflow of analysis of cardiac MR data. Since the complete segmentation process is automated the physician does not have to waste much time with tedious segmentation and may concentrate on diagnosis.

# Chapter 5

# Entropy-Optimized Texture Models

**This chapter is based on the following publication:**

Sebastian Zambal, Katja Bühler, and Jiří Hladůvka. Entropy-Optimized Texture Models. *Medical Image Computing and Computer Assisted Intervention (MICCAI)*, pages 213–221, 2008.

## 5.1 Introduction

Statistical shape models exploit prior knowledge of shape to perform robust segmentation. Active Shape Models (ASMs) [15] are based on Principal Component Analysis (PCA) of a set of corresponding training shapes. In the matching process, the model iteratively deforms attracted by image features (e.g. edges).

Additionally to shape, Active Appearance Models (AAMs) [14] incorporate texture variations (represented again by PCA). In the following we motivate our new approach to texture representation for statistical models by summarizing some critical aspects of texture modeling in AAMs.

**Low contrast and fuzzy structures.** Model matching is understood as finding the model instance which exhibits the minimal difference to the unseen image. Hence it is very important to employ an effective difference measure which consistently reflects how well a given model instance matches the image. In the context of AAMs, typically measures based on texture differences are used. The assumption is made that large texture differences correspond to a large misalignment of the model. However, low contrast (e.g., lung and myocardium in cardiac MRI) and fuzzy/irregular structures (e.g., spongy bone, trabeculae) make it difficult to objectively compare texture differences which are measured in different image regions. It may thus happen, that regions of low contrast are over-ruled by regions showing fuzzy structures.

**PCA-based texture modelling.** For many datasets we observed that a large number of PCA texture parameters are required to sufficiently well cover variations in a training set. For the data investigated in this chapter we observed that the sorted eigenvalues of shape decrease much faster than those of texture. This suggests that PCA is not the optimal choice for texture modeling.

**Texture normalization.** To improve the quality of AAMs, a texture normalization step is usually applied before statistical analysis. The goal is to keep irrelevant texture variations (e.g., global variations in brightness or gamma) out of the model. In the scope of AAMs different methods have been proposed (e.g., different types of non-linear texture normalization [35]). However, in general it is hard to predict which type of texture normalization leads to good results for which kind of data.

**Mutual Information.** A very popular matching criterion for medical image registration is mutual information (MI) [70]. The great advantage of this measure is that it makes it even possible to register images which were acquired using different imaging methods. Mutual information is based on entropy terms and in its original form limited to registration of a pair of images. Thus, although it would be reasonable to integrate mutual information into the AAM framework this cannot be done straightforwardly.

**Bayesian Framework.** Bayesian reasoning makes use of posterior
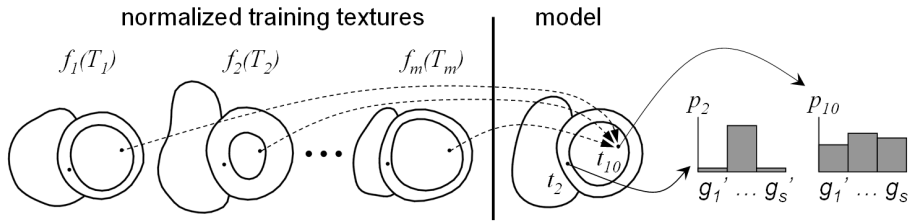
**Figure 5.1:** *The entropy texture model: normalized corresponding pixels are modeled by probability distributions.*

probabilities to quantify how well a given model explains unknown data. Based on Bayes' law prior probability is combined with the likelihood of an observation to derive the posterior probability of the model. Bayesian reasoning has a sound mathematical background and is well-established for pattern recognition tasks. Thus it seems worth to incorporate it into the framework of statistical models of shape and appearance.

To tackle the above issues we borrow ideas about entropy from groupwise registration and formulate a novel probabilistic texture model. In section 5.2 we derive an optimization function for texture normalization which has similarities with a recently proposed function for *shape* correspondence optimization [8]. In section 5.3 we match the model to unseen images using Bayesian inference. We demonstrate the robustness of our entropy-optimized texture model (ETM) on four different 2D training sets: vertebra, brain ventricles, mid cardiac, and basal cardiac slices (section 5.4). Based on this validation we conclude in section 5.5 that the proposed ETM outperforms AAMs and even copes with texture variations due to different imaging modalities (different MRI scanners, T1/T2/FLAIR, CT/MRI).

## 5.2 Entropy Texture Model: Construction

Similar to AAM, the input for the model we propose is a set of $m$ training images $T_i$, annotated with a fixed number of landmark points in correspondence, consistently triangulated, resampled by $n$ texels and quantized to $r_i$ gray levels.

While identical in shape description by mean and principal components, our model differs from AAMs in the representation of texture. Each of the $n$ model texels $t_j$ captures the statistical variations observed at corresponding training pixels.

In order to keep unspecific intensity variations out of the model we propose to normalize the training images using generic intensity mappings. The task is to optimize $m$ intensity maps $f_i$ that quantize the training images

from $r_i$ to $s$ gray levels.

$$f_i : \mathbb{Z}_{r_i} \to \mathbb{Z}_s, \quad s \ll r_i \qquad i = 1 \dots m \tag{5.1}$$

In the following we design the cost function to assess mappings $f_i$. Each model's texel $t_j$ observes $m$ occurrences of the $s$ possible mapped gray values at corresponding training texels. Such a set of observations can be interpreted as probability density function (PDF) and we denote it $p_j$. $p_j(g'_k)$ is the probability that at corresponding texel $t_j$ a mapped gray value $g'_k$ is observed.

The predictability of mapped gray values expressed by PDFs varies across model texels. Figure 5.1 illustrates the situation for two texels. While PDF $p_2$ exhibits a single high peak, $p_{10}$ is rather equally distributed. This suggests that predictions of gray values for texel $t_2$ will be more reliable than for texel $t_{10}$.

Inspired by Balci *et al.* [1] we propose to favor reliability (similar to $p_2$) and to penalize uncertainty (similar to $p_{10}$) by minimizing the entropy of the corresponding PDFs: $H(p_j) = -\sum_{k=1}^{s} p_j(g'_k) \log_2(p_j(g'_k))$. Considering all $n$ model texels yields a cost function that measures the quality of mappings $f_i$:

$$H^{model} = \frac{1}{n} \sum_{j=1}^{n} H(p_j) \quad \to \min \tag{5.2}$$

$H^{model}$ yields a minimum when the mappings degenerate such that all mapped training pixels show the same gray value. In this case the model exhibits maximal specificity.

However, this specificity has to be put into relation to the training images which contain no information once degenerated. This motivates for a compensation term which drives the mapped training textures $f_i(T_i)$ towards maximum information content. We measure the information content by *image entropy* $H(f_i(T_i))$ and aim at its maximization across the entire normalized training set:

$$H^{tex} = \frac{1}{m} \sum_{i=1}^{m} H(f_i(T_i)) \quad \to \max \tag{5.3}$$

$H^{tex}$ reaches a maximum when the texture transformations $f_i$ maximize the information content of the textures $T_i$. This is equivalent to histogram equalization.

We combine the entropy terms of model (eq. (5.2)) and training textures (eq. (5.3)). The goal is maximization in terms of texture mappings $f_i$:

$$\{f_1^*, \dots, f_m^*\} = \underset{\{f_1, \dots, f_m\}}{\operatorname{argmax}} \quad (H^{tex} - H^{model}) \tag{5.4}$$

(a) original



(b) optimized
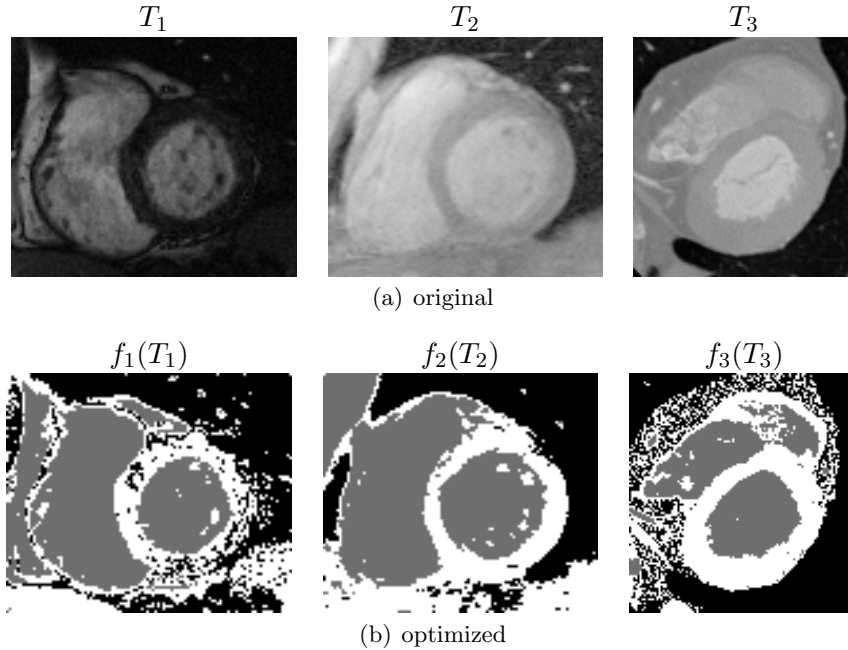
**Figure 5.2:** *An example training set (two different MRI scanners and a CT) before (a) and after (b) entropy-optimization (using three target gray levels: s = 3).*

There is no need for an ad-hoc weighing of the two entropy terms since they are commensurate, i.e., measured in bits per texel and bits per pixel respectively. An objective function similar to eq. (5.4) has recently been proposed for *shape* correspondence optimization [8]. In this work similarly two energy terms are used: one for individual shapes and one for a shape ensemble. This makes our entropy-optimization of texture a direct analogy to the Minimal Description Length (MDL) of shape with the difference that we do not stick to the Gaussian distribution as description language for texture.

We used Simulated Annealing to optimize mappings $f_i$ subject to the cost function of eq. (5.4). Represented by lookup tables, the texture mappings $f_i$ are initialized to linearly remap the training images to $s$ levels. During optimization the lookup tables are updated in each iteration. After optimization the mapped training textures represent structures with minimal uncertainty at maximum information content (figure 5.2(b)).

Figure 5.3 shows entropies of the optimized distributions of four models we use for validation in section 5.4. While bright texels exhibit strong variations (high entropy), dark texels represent high predictability (low entropy).

(a) heart LV+RV     (b) heart LV     (c) vertebra     (d) brain ventricles
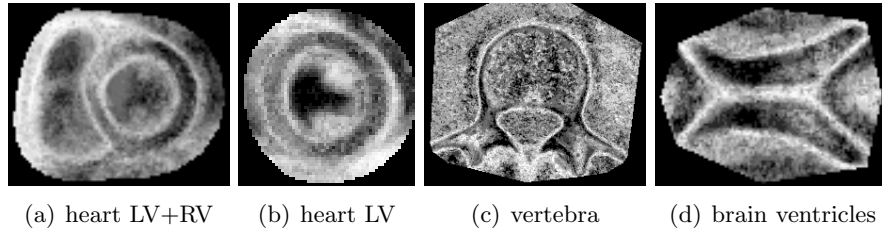
***Figure 5.3:*** *Entropy (brightness) of model PDFs after optimization.*

## 5.3   Entropy Texture Model: Matching

In contrast to AAMs, only shape parameters $S = \{$position, scaling, rotation, and statistical shape deformation$\}$ are optimized. The cost function describing model matching accuracy is based on model PDFs and sub-texture $U = (u_1, \ldots, u_n)$ of the unseen image currently overlapped by the model.

### Mapping of the Unseen Image's Texture

As our model texels capture PDFs of $s$ normalized gray values, we first need to normalize $U$ accordingly: we seek for a function $f_u : \mathbb{Z}_{r_u} \to \mathbb{Z}_s$ that maps the texture to $s$ gray levels.

We want to find a suitable intensity mapping for each of the $r_u$ gray values. For a fixed gray value $\hat{u} \in \{1, \ldots, r_u\}$ all model texels observing it vote according to their PDFs: out of the $s$ possibilities the target gray value leading to the maximal likelihood is assigned. Formally:

$$f_u(\hat{u}) = \operatorname*{argmax}_{g'_k} \prod_{u_j = \hat{u}} p_j(g'_k) \qquad k = 1 \ldots s \qquad (5.5)$$

### Cost Function

To assess how well the shape instance $S$ fits to the unseen image, we compare model PDFs $p(.)$ to the normalized texels $U' = f_u(U) = \{f_u(u_j)\}_{j=1}^n$. To convey this, we consider maximizing the posterior probability $P(S|U')$ of the shape instance $S$, with the observed normalized texture $U'$ given. According to Bayes' law [5] the posterior is proportional to the product of a likelihood and a prior (left side of eq. (5.6)).

The *likelihood* $P(U'|S)$ of the observed normalized texture $U'$, with the shape instance $S$ given, is (under the *naive* Bayesian assumption) the product of probabilities of the normalized texels. This is only true under a naive Bayesian assumption: A pixel's gray value in an image depends only on the parameters of the model but not on other pixels' gray values. Although in general the Bayesian assumption does not hold, recent literature suggests

(a)          (b)          (c)          (d)          (e)
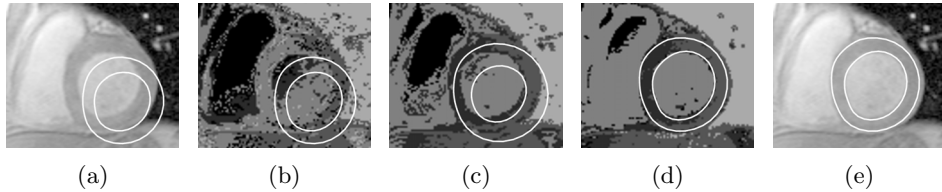
**Figure 5.4:** *Matching of a model comprising five target values ($s = 5$): original image with initialized contour (a), maximum likelihood estimate for $f_u$ for initial contour (b), after 4 iterations (c), and after 8 iterations (d). Final match over the original unseen (e).*

that in the case of a large number of random variables (in our case pixels), naive Bayesian reasoning is astonishingly reliable [78].

The *prior* probability $P(S)$ of shape instance $S$ is calculated feeding its parameters into the multivariate Gauss distribution that corresponds to the PCA shape space (please refer to [5] for details).

Putting both terms together yields the cost function which is maximized subject to shape parameters $S$:

$$P(S|U') \quad \propto \quad P(U'|S)\,P(S) \quad = \quad \left( \prod_{j=1}^{n} p_j(f_u(u_j)) \right) \ P(S) \qquad (5.6)$$

**Strategy and Implementation Issues**

In contrast to AAM there are no texture parameters to optimize. The search space is only spanned by shape parameters and typically has not more than 10 to 15 dimensions. This makes exhaustive search strategies similar to [18] affordable and we employ such a scheme in this work. Figure 5.4 illustrates how a model with five gray levels evolves during matching. Shape and maximum likelihood texture mapping converge consistently. Algorithm 1 summarizes how model matching is implemented: shape update, estimation of texture transformation, and likelihood calculation of the model are iterated.

Any $p_j(.)$ being zero degenerates the equations (5.5) and (5.6). In order to avoid this we assign a small compensation probability of $1/(2m)$ and renormalize the distribution $p_j$.

To avoid numerical instability due to the large number of multiplications in equations (5.5) and (5.6) we maximize sums of logarithms of the probabilities instead.

---

**Algorithm 1** *Model matching*

---
input:  unseen image
output: model instance, i.e., segmentation
**repeat**
    change {position, rotation, scale, shape: $[mode_1, [mode_2, \ldots]]$ }         $\triangleright$
shape update
    re-estimate texture transformation                    $\triangleright$ eq. (5.5)
    evaluate the match                           $\triangleright$ eq. (5.6)
**until** improvement falls below threshold

---

## 5.4   Validation and Results

In order to validate our approach we compared the segmentations achieved by ETM ($s = 5$) to those achieved by standard AAM. For cross validation we split the training sets into reasonable subsets (e.g., images from same patient or same scanner). Every image was matched as an unseen by a model built from complementary subsets. Model matching was performed by initializing each of the models close to the correct contours (hence no automatic initialization of the model was done). Matching accuracy was measured in terms of average point-to-contour distances. To include enough information about object boundary regions into the models, additional landmark points outside the objects were defined. In the following we describe the datasets and the results in detail.

**Heart LV+RV, basal region:**

contains short axis slices from the base of the heart showing few or no papillary muscles. The training set comprises data from four different sources: CT and three different MR protocols. Annotations define the contours of inner and outer boundaries of the left ventricle (LV) and the inner contour of the right ventricle (RV). ETM performed better in 23 out of 38 cases, reducing the average point-to-contour distance from 4.36 to 3.36 mm.

**Heart LV, mid region:**

includes 42 short axis MR images from the mid region of the heart exhibiting large texture variations due to papillary muscles. Images stem from two different MR scanners.The average pixel size is 1.39mm. Annotations define the contours of the inner and outer boundaries of the left ventricle (LV). ETM performed better in 38 out of 42 cases, reducing the average point-to-contour distance from 4.02 to 2.38 mm.

**Brain ventricle:**

comprises 17 transversal MR slices of 15 different patients. One patient is represented by a T1 image and a FLAIR image. Another patient is represented by a T2 image and a FLAIR image. The remaining patients are represented each by a T1 image. The average pixel size is 0.85mm. Annotations define the contours of brain ventricles. ETM performed better in 16 out of 17 cases, reducing the average point-to-contour distance from 3.53 to 1.67 mm.

**Vertebra:**

consists of 13 CT slices from 4 different patients showing transversal sections of lumbar vertebrae. The average pixel size is 0.32mm. Annotations define the outer contour of the vertebra and the contour of the spinal canal. ETM performed better in 9 out of 13 cases, reducing the average point-to-contour distance from 2.67 to 2.06 mm.

On average our ETMs clearly outperformed AAMs. Results are summarized graphically in figure 5.5.

## 5.5 Conclusions

We proposed a novel texture model for medical image segmentation. Its texture is described by probability distributions of individual texels. Moreover, these probabilities are optimized by information entropy terms. This allows to effectively cope with unspecific intensity variations in the training set caused e.g. by different modalities, scanner settings, and fuzzy anatomical structures. The model is matched to unseens in accordance with Bayesian reasoning.

There are two major messages we would like to conclude with. First, ETM perform better than AAM, as it is shown in the validation. Second, thanks to intensity normalizations that are an integral part of model construction, some requirements on the training texture (e.g. Gaussian distribution) can be relaxed. We have demonstrated this with training sets containing mixtures of CT/MR and MR T1/T2/FLAIR images.

There are several issues left for future work. To name a few, we intend to address extension to 3D volume textures, automatic initialization, and acceleration of matching in the near future.
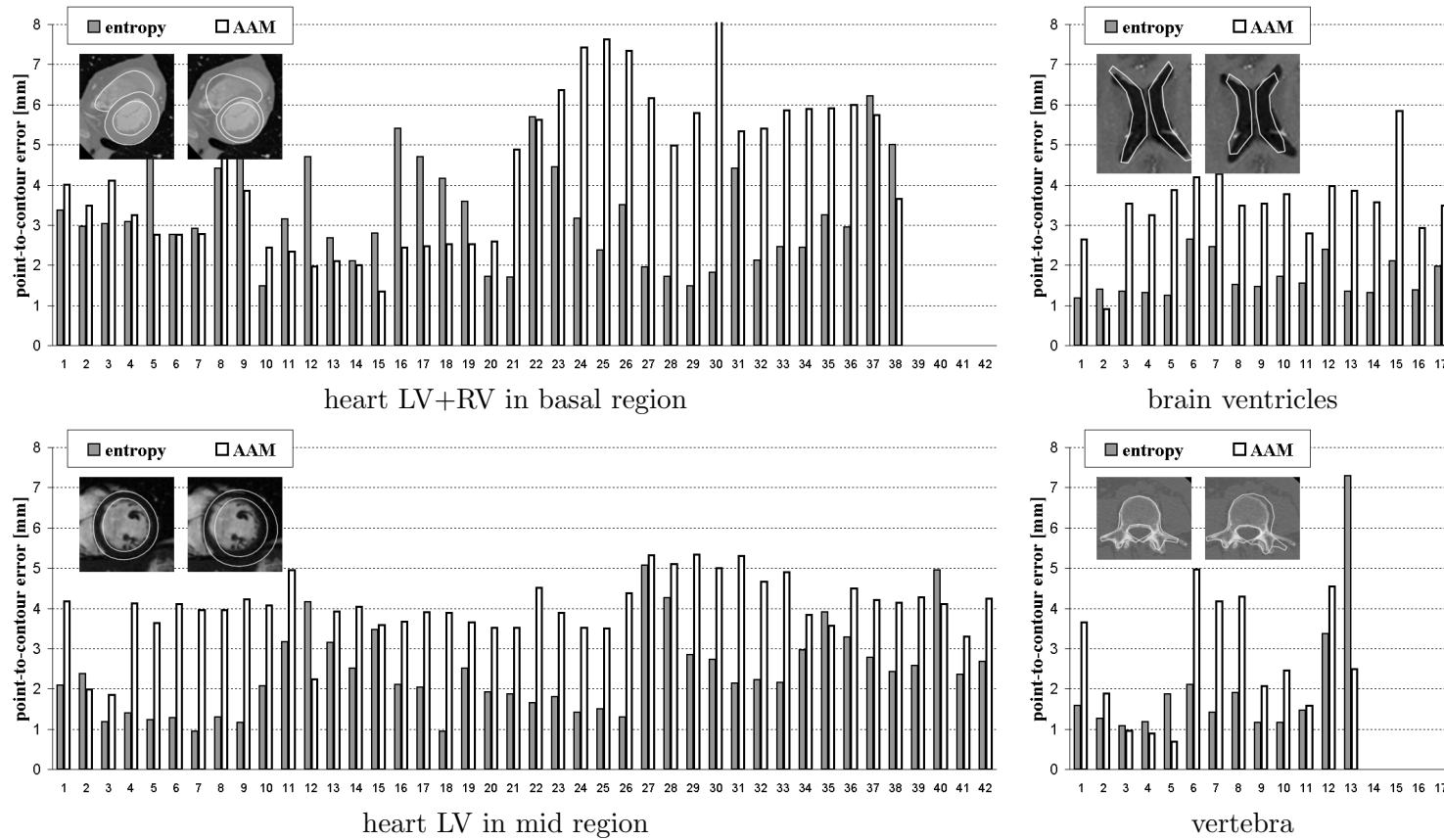
**Figure 5.5:** *Average point-to-contour errors [mm] achieved by ETMs and AAMs. Example thumbnails show final segmentations.*

# Chapter 6

# Shape and Appearance Models for Automatic Coronary Artery Tracking

## 6.1 Introduction

Automatic detection of coronary arteries in Computed Tomography Angiography (CTA) is a clinically very important but challenging task. Efforts are currently being undertaken to automate coronary artery tracking in order to improve the medical workflow and objectively quantify clinically important properties of coronary arteries.

There is a large amount of literature about vessel extraction in 2D and 3D medical images [33]. Many of the approaches rely on features such as the response of the Hessian matrix filter [51]. However, it is in general difficult to derive the full connectivity of a vessel tree from this information. A method is required which takes into account the spatial relationships of features. For example, a shortest path algorithm with costs corresponding to feature responses may be applied for extracting a vessel [28, 23].

A very promising direction in medical image analysis is the application of (statistical) models which represent shape (geometry) and appearance (texture) of the investigated anatomical structures. Active Appearance Models (AAMs) [14], for example, extract knowledge about shape and appearance from a set of training examples by applying Principal Component Analysis (PCA). Another approach uses Markov Random Fields (MRFs) in combination with symmetry features [20]. By matching a model of shape and appearance to unknown image data, high-level knowledge about spatial and gray value relationships of structures is exploited.

In this chapter we refer to a model of shape and appearance as a set of spatial configurations of texture sample positions (shape model) and well defined relationships between gray values at these sample positions (texture model). When matching a model of shape and appearance to unknown image data, two critical issues arise: First, a reasonable objective function has to be used which sufficiently well reflects matching accuracy of the model. Second, an effective optimization technique has to be applied which robustly optimizes the objective function to achieve a match.

The method proposed here employs two distinct shape and appearance models. First, an anatomical model of the complete heart is used (followed by symmetry feature extraction) to roughly locate potential seed points of coronary arteries (section 6.2). Second, vessel tracking is accomplished by matching a cylinder-like model in combination with depth-first search (section 6.3). For detailed information on the datasets used for validation please refer to [41].

The proposed method was directly compared to four other automatic [3, 66, 34, 71], three semi-automatic [37, 19, 7], and five interactive [24, 64, 40, 79, 26] coronary artery tracking algorithms at the MICCAI 2008 workshop "Segmentation in the Clinic: A Grand Challenge II". In the following the other fully automatic approaches are shortly outlined.

Very good results were obtained by Bauer and Bischof [3]. Their ap-

proach is based on a robust vesselness filter using a normalized gradient vector field (GVF). Normalization of gradients leads to a high independence from the image contrast and thus increases robustness. The proposed vesselness filter is applied to the complete volume. Centerlines of vessels are then extracted all over the dataset using a hysteresis loop. Finally vessel segments are connected and the largest connected component represents the extracted coronary artery tree. Due to its bottom-up structure the method achieves better results in overlap measures than the presented method. However, accuracy measures are worse because the normalized gradient vector field does not necessarily align the automatically computed centerlines with the reference centerlines.

Tek et al. [66] implement a shortest path algorithm for small vessel segments. A cost function is used which calculates local vesselness based on a 2D cross section of the volume. By iteratively finding optimal local paths the vessel tree is extracted.

The basic idea behind the work of Kitslaar et al. [34] is connected component labeling. From the segmentation masks the centerlines are then reconstructed. Fast-marching level sets are used to calculate initial centerlines. These initial centerlines are further refined by calculating curved multi planar reformatted images and detecting longitudinal lumen contours. Although Kitslaar et al. reach a relatively high accuracy of centerlines, their accuracy is still lower than the model-based approach.

Wang and Smedby [71] segment the coronary artery tree using fuzzy connectedness. A distance map is then used to improve the centerline.

## 6.2 Detection of Potential Coronary Artery Origins

Two steps are carried out to automatically detect potential origins of coronary arteries: First, a 3D model of the heart is matched to the volume data. Second, local maxima of a symmetry feature volume are calculated and identified as potential coronary artery origins.

### 6.2.1 3D Model of the Heart

A 3D model of the heart is built based on 2245 manually placed landmark points defined on dataset 04. This dataset is chosen since it exhibits a low noise level according to the noise estimation algorithm outlined in section 6.3.3. Landmark points are defined on the left atrium, the left ventricle, the origin of the aorta, the pericardium, and outside around the heart. Figure 6.1(a) shows the model as wireframe and figure 6.1(b) as transparent rendering. Figure 6.1(c) shows the model matched to dataset 03.

A Delaunay tetrahedralization of the landmark points is performed to

(a)  (b)

(c)
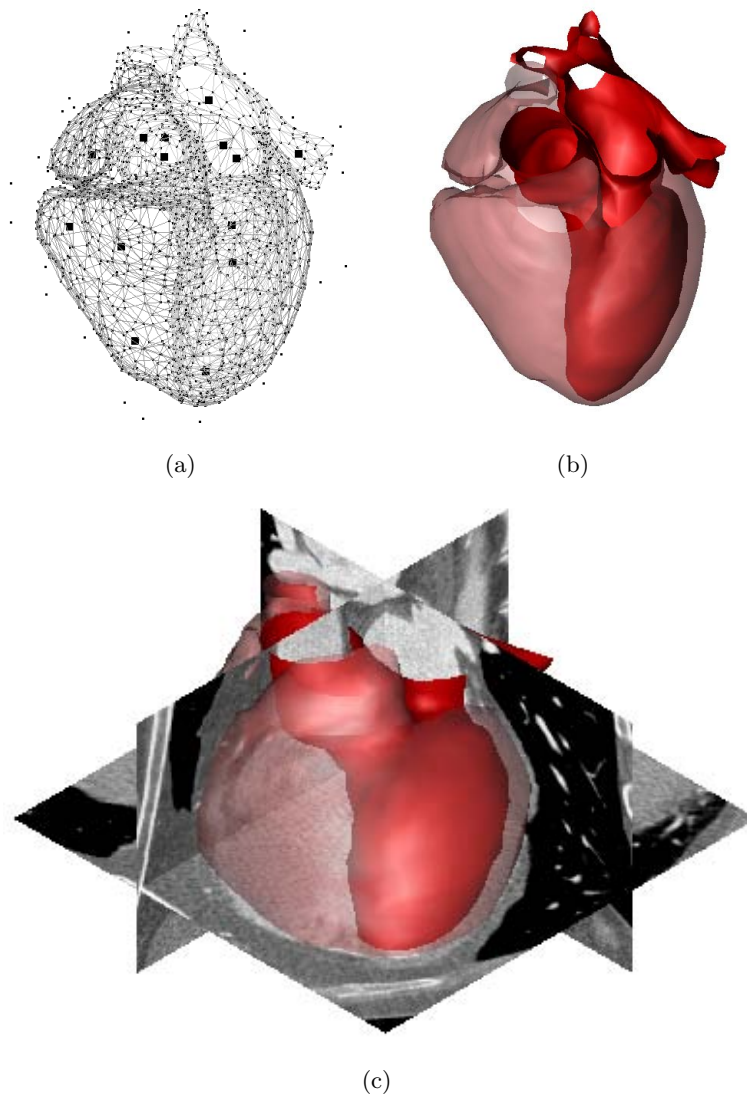
**Figure 6.1:**  *The 3D heart model as wireframe (a) (small black squares
represent control points for diffeomorphic warps), as partially transparent
surface model (b) and matched to dataset 03 (c).*

obtain a volumetric tetrahedra mesh. A grid of texture samples (with a cell size of 7mm edge length) is layed over the tetrahedra mesh. For each sample position the barycentric coordinates within the surrounding tetrahedron are stored. A deformation describing the displacements of landmark points can easily be passed on (via the precalculated barycentric coordinates) to the volumetric grid of texture samples.

To allow for smooth deformations of the landmark points during matching we apply a combination of diffeomorphic warps similar to those used, e.g., for diffeomorphic statistical shape models [12]. However, we do not use a regular grid for control points, but manually distribute them sparsely within the heart. Small black squares in figure 6.1(a) represent the 14 control points. Spatial transformations (scaling and translation) at control points are passed on to landmarks in the neighborhood. Deformation displacements are weighted with a function $k$ of the distance between landmark and control point. As $k$ we choose a scaled Gaussian function ($\sigma = 30mm$, $\mu = 0$). A scaling factor is used such that $k(0) = 1$.

The appearance part of the model assigns one out of three classes to each texture sample. A class is assigned to each voxel by investigation of the original gray values as observed in dataset 04. Histogram equalization is performed for normalization first. A quantization of gray values to three quantization levels each representing one class is performed. As expected, the three classes correspond approximately to the regions of lung, myocardium and contrast enhanced blood.

Model matching accuracy (the objective function for matching) is evaluated by first sampling gray values according to the spatial configuration of the model in the current iteration. Next, gray value classification is estimated via maximum likelihood of the observed gray values. Finally, the *observed* classes are compared with the *expected* classes for each texture sample and a likelihood is calculated as in [75]. A probability of 0.1 is assigned to misclassified samples and a probability of 0.9 is assigned to correctly classified samples. We use a shape particle filtering approach [18] for calculating the optimal shape (with respect to the texture model) in the shape space spanned by the parameters of rigid transformation and diffeomorphic warps.

### 6.2.2 Local Symmetry

Two of the 3D model's landmark points, **L** and **R**, are located directly on the left and right coronary arteries close to the aorta (figure 6.2(a)). After model matching these two landmarks define the locations where the origins of the two main coronary arteries are approximately located. Due to anatomical variations, however, these points will probably not exactly reside on the coronary arteries of the unknown dataset after model matching. This is why we look for coronary origins within a region of radius $r_{init}$ around **L** and **R**. $r_{init}$ is chosen 2.5 times the distance of two landmark points $\mathbf{A_1}$
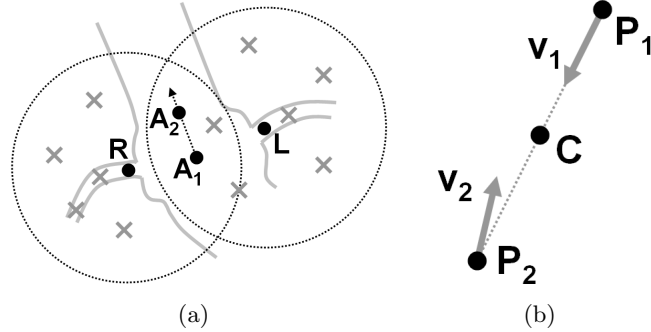
***Figure 6.2:*** *(a) Four landmark points $\mathbf{A_1}$, $\mathbf{A_2}$, $\mathbf{L}$, and $\mathbf{R}$ are used to define regions that are searched for coronary artery origins. Local maxima of symmetry features (potential origins) are shown as bright crosses. (b) Calculation of symmetry feature contribution along scan lines.*

and $\mathbf{A_2}$ inside the aorta as illustrated in figure 6.2(a).

At this stage of the algorithm we are interested in *potential* coronary artery origins. The idea is to gain robustness by calculating multiple candidates and to later select the best ones after more detailed evaluation. In fact we decide which of the potential origins are coronary arteries after few tracking iterations using the tracking algorithm outlined in section 6.3. We calculate a simple symmetry feature to identify locally promising coronary artery candidates. A symmetry feature volume for regions around $\mathbf{L}$ and $\mathbf{R}$ is initialized with value 0 for every voxel and 3D image gradients are precalculated. A scan line of length $10mm$ (which is assumed the maximum diameter of a coronary artery) along the direction of the gradient vector $\mathbf{v_1}$ is traversed. Figure 6.2(b) illustrates this for a voxel at position $\mathbf{P_1}$. At every position along the scanline such as $\mathbf{P_2}$, a second gradient vector $\mathbf{v_2}$ is investigated. The squared length of $\mathbf{v_1} - \mathbf{v_2}$ is calculated and added to the voxel within the feature volume at position $\mathbf{C}$ (which lies in the middle between $\mathbf{P_1}$ and $\mathbf{P_2}$). This procedure is carried out for every voxel. Finally, the feature volume contains high values at voxels which locally exhibit high symmetry. After the symmetry volume has been generated, local maxima are identified as potential coronary artery origins.

Each potential coronary seed is tracked 3 iterations wide using the vesselness function $v$ defined below. For these three iterations the average vesselness is calculated and the origin with the best evaluation is used as the first coronary artery to be further tracked. The vector $\mathbf{a}$ from $\mathbf{A_1}$ to the first symmetry maximum is calculated. The next best candidate with a vector $\mathbf{b}$ from $\mathbf{A_1}$ to this candidate and an angle of more than $50°$ between $\mathbf{a}$ and $\mathbf{b}$ is selected as the second coronary artery. For these two finally selected origins a tracking backward into the aorta is performed by using the tracking method outlined below.

## 6.3 Vessel Tracking

We accomplish vessel tracking by incremental matching of a shape and appearance model. In contrast to the 3D model for the heart it is difficult to formulate a generic shape model for the vessel tree of coronary arteries. Shape and topology vary substantially between patients. We incrementally grow the vessel tree starting from the two origins of left and right coronary arteries. In principle we proceed in a similar way as a recently proposed method that uses Bayesian tracking [53]. However, our method differs in how successive candidates are selected. Furthermore our method handles branching and termination.

### 6.3.1 Estimating Vesselness

We track a vessel by iteratively matching a rigid model with simple symmetric shape. For a given position $\mathbf{x}$, a vector $\mathbf{d}$ indicating the tangential direction of the vessel, and a radius $r$, we define a function $v(\mathbf{x}, \mathbf{d}, r)$ which reflects the "vesselness" of the given configuration for a given volume dataset. Texture samples are created by using a shape pattern of two concentric circles which are translated and scaled along direction $\mathbf{d}$. A pure translation of two concentric (an interior and an exterior) circles leads to a perfectly cylindrical pattern. However, if – as illustrated in figure 6.3 – the artery exhibits strong bending at the investigated position, a straight cylindrical model does not fit well. Along the central axis we scale the circles which carry texture samples by using a scaling function $s(x)$ where $x$ is the distance to the center of the pattern divided by the radius $r$.

In fact we use two patterns for two different levels of detail. In the first step a pattern with larger margins but smaller scaling is used for evaluating the approximate direction of the vessel. This pattern is depicted in figure 6.4(a) (cross section) and 6.4(b) (3D). Quadratic scaling functions

$$s_{1,in}(x) = 0.75 - x^2 * 0.2 \tag{6.1}$$

and

$$s_{1,ext}(x) = 1.25 + x^2 * 0.2 \tag{6.2}$$

of interior and exterior radii are applied along the axis. In the second step the estimated position of the vessel is refined by using a second pattern depicted in 6.4(c) (cross section) and 6.4(d) (3D). Circle-shaped scaling functions

$$s_{2,in}(x) = -0.05 + \sin\left(\arccos\left(x\right)\right) \tag{6.3}$$

and

63
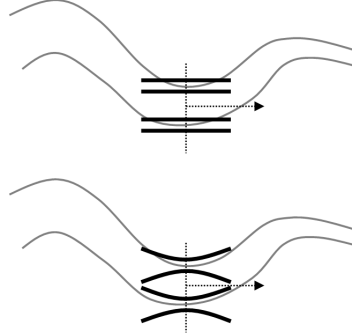
***Figure 6.3:***  *Straight cylindrical pattern versus bent pattern for estimation of vesselness.*

$$s_{2,ext}(x) = 2.05 - \sin\left(\arccos\left(x\right)\right) \tag{6.4}$$

of interior and exterior radii are applied along the axis. For both patterns additional samples lying at the central axis along the direction of the vessel are sampled and marked as interior samples. In figures 6.4(a), 6.4(b), 6.4(c), and 6.4(d) the interior sample positions are colored gray and exterior samples are colored black.

For a given shape configuration $(\mathbf{x}, \mathbf{d}, r)$, the texture values of the sampling pattern are accordingly extracted from the volume data using nearest neighbor interpolation. These values are used to create two separate histograms $H_{in}$ and $H_{out}$ for interior and exterior sample values respectively. The basic assumption is made that in case of a perfect alignment with a vessel, there must be a threshold that optimally separates both histograms. This is illustrated in figure 6.5(a) where the dashed line represents the threshold and on the left side perfectly separates samples from inside and outside the vessel. On the right side the separation is not so obvious. The number of values which are (as expected) greater than the threshold for the interior histogram are divided by the total number of interior samples. The resulting fraction $f_{in}$ is the fraction of gray values which have a value as expected by the model. Similarly, for the exterior histogram the fraction $f_{ext}$ of values smaller than the threshold (as expected) is calculated. The vesselness function $v$ is finally defined as the mean of the above fractions:

$$v(\mathbf{x}, \mathbf{d}, r) = \frac{f_{in} + f_{ext}}{2} \tag{6.5}$$

where the threshold is chosen such that $v$ is maximized.

(a)

(b)

(c)

(d)
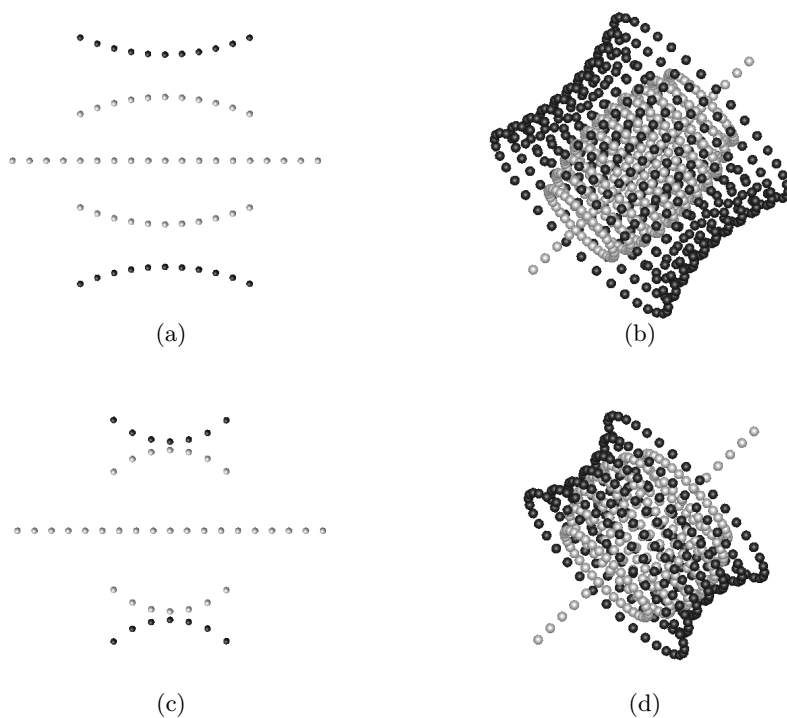
**Figure 6.4:** *Cross section (a) and 3D view of sampling pattern 1 (b). Cross section (c) and 3D view of sampling pattern 2 (d).*



(a)

(b)
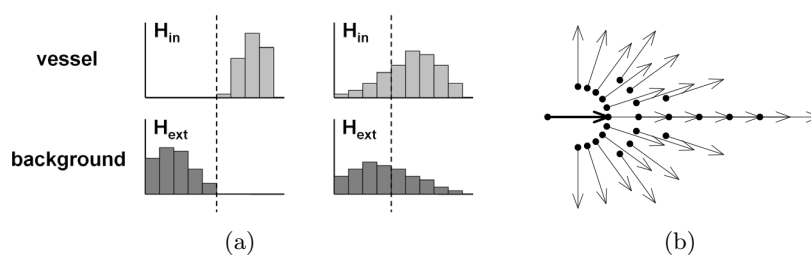
**Figure 6.5:** *The histograms generated from locally sampled texture (a). Candidates evaluated for finding the successive segment (b). Dots with arrows indicate positions and orientations of the segments. The bold arrow represents the current segment.*

65

### 6.3.2   Tracking of Vessels

The proposed vessel tracking algorithm proceeds in a depth-first fashion by adding new vessel segments to the vessel tree that has been extracted so far. A vessel segment is defined again by a shape configuration $(\mathbf{x}, \mathbf{d}, r)$ as outlined in section 6.3.1. By convention $\mathbf{d}$ points from proximal to distal. The idea is to compare possible candidates for the successive vessel segment distal to the current one. Vessel tracking is continued with the segment that exhibits the highest value of the vesselness function $v$.

Let $\mathbf{s}_c = (\mathbf{x}_c, \mathbf{d}_c, r_c)$ be the current vessel segment. A set of candidates for successive segments is calculated in the following way. Direction vectors $\mathbf{d}_{n,i}$ with angles $\alpha$ between $-90°$ to $90°$ relative to $\mathbf{d}_c$ in steps of $18°$ are considered. Radii for the new candidates range from $0.5r_c$ to $1.5r_0$ in scaling increments of 1.1. Positions for candidates are generated as

$$\mathbf{x}_{n,i} = \mathbf{p}_c + \Delta(\mathbf{d}_c + \mathbf{d}_{n,i})/2 \qquad (6.6)$$

where $\Delta$ is the step size. We use a variable number of step sizes $n_{steps}$ depending on $\alpha$. The values 6, 3, 2, 1 are assigned to $n_{steps}$ for $\alpha < 5°$, $30°$, $60°$, $90°$ respectively. The distance to the successive candidates is calculated as $(n_{steps} \cdot r_c)/2 + 0.5$. This scheme for the generation of successive candidate positions $\mathbf{x}$ and directions $\mathbf{d}$ is illustrated in figure 6.5(b).

From all generated candidates the one with the most significant (largest) vesselness $v(\mathbf{s}_{n,i})$ is selected as the successive candidate. In order to refine the candidate, a set of refined (altered position, scaling, radius) candidates close to the selected one is generated by using sampling pattern 2. Again the one with the most significant vesselness survives.

The second best candidate for which the direction vector differs more than $30°$ to the direction vector of the best successive candidate is stored as a possible branch. The vessel is tracked until the termination criterion which is discussed in section 6.3.3 is fulfilled. Then all possible branches of the terminated vessel are investigated. Each branch is tracked five segments wide. The depth-first search is continued with the branch that exhibits the largest average vesselness of the first five segments. The algorithm proceeds until a maximum number of vessels (in the reported experiments we used 30) is found. An additional restriction is that sub-branching is stopped for vessels where a branching depth of two is reached.

### 6.3.3   Termination Criterion

We estimate the level of noise in a CTA volume before starting vessel tracking. Later this estimate is used in a noise-adaptive criterion for vessel termination. The vessel termination criterion is not related with the vesselness function $v$ which is only used for selection of the optimal successive segment. We apply a simple noise estimation scheme where we consider gray value differences, $\delta_g$, of neighboring voxel pairs. A neighboring voxel pair is defined
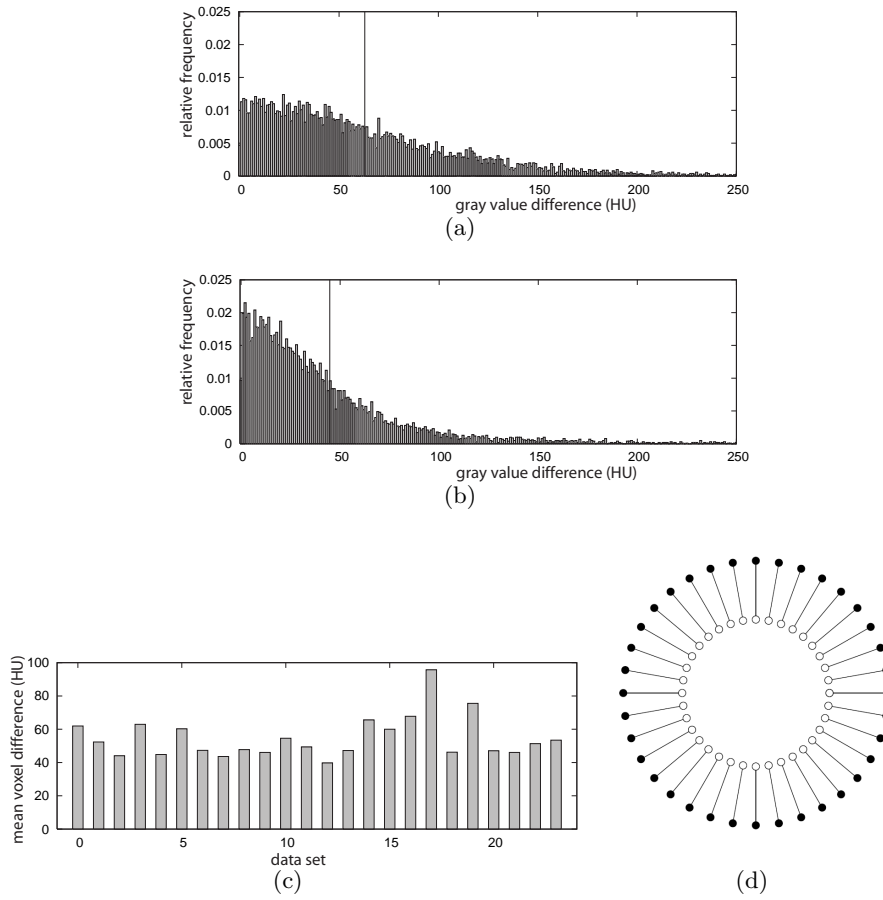
**Figure 6.6:** *The relative frequencies of local gray value differences in datasets 03 (a) and 04 (b) respectively (vertical lines indicate mean absolute differences $\overline{\delta}_g$). (c) The mean of estimated noise distributions for workshop datasets 00 – 23. (d) Pairs of samples compared with mean voxel difference for termination criterion.*

as a pair of voxels with a distance of three voxel diameters. 100,000 voxel pairs are randomly chosen and absolute gray value differences are measured. In order to keep out regions within the lung, only voxel pairs are considered for which both gray values are greater than -500 Hounsfield units (HU). Figures 6.6(a) and 6.6(b) show the resulting relative frequencies of gray value differences for datasets 03 and 04. The mean values of gray value differences $\bar{\delta}_{g,03}$ and $\bar{\delta}_{g,04}$ for datasets 03 and 04 are 63 and 45 Hounsfield units respectively. The mean values for all datasets are shown in figure (c).

We consider a gray value difference, $\delta_g$, less than or equal the mean, $\bar{\delta}_g$, most likely to originate from noise. A gray value difference greater than $\bar{\delta}_g$ rather indicates a meaningful transition between background and object at the corresponding voxel pair. During vessel tracking, pairs of gray values are considered: each interior texture sample is compared to its radially exterior neighbor sample (figure 6.6(d); sample pairs are connected by lines). If more than half of the measured texture differences are less than the average gray value difference, the vessel is considered not distinguishable from the background. If two successive vessel segments fulfill this criterion the vessel is terminated.

In fact we use some additional vessel termination criteria. If the vessel intersects with itself (a segment overlaps with one of its preceding segments) the vessel is terminated. Further, if the mean gray value of exterior samples falls below a Hounsfield value of -500 (lung vessel), tracking is stopped.

### 6.3.4 Smooth Interpolation of Centerline Segments

The method presented above generates a discrete set of vessel center points. In order to derive a continuous 3D curve which better approximates the vessel's centerline, an adequate interpolation technique has to be applied.

A Bezier curve is fit in order to interpolate the vessel's centerline in between adjacent segment centers. An example is illustrated in figure 6.7. The center positions $\mathbf{P_0}$ and $\mathbf{P_1}$ and unit length tangent vectors of the centerline $\mathbf{t_0}$ and $\mathbf{t_1}$ are known from segment fitting. However, in order to fit a cubic Bezier curve, two additional control points (or the exact lengths of tangent vectors) are required. In this work the assumption is made that the following distances are equal: $\overline{\mathbf{P_0P_2}}, \overline{\mathbf{P_2P_3}}, \overline{\mathbf{P_3P_1}}$. With this assumption the exact positions of control points $\mathbf{P_2}$ and $\mathbf{P_3}$ upon tangents of the centerline are calculated. By taking the additional control points into account, a Bezier curve can be calculated for each segment.

Let $v$ be the vector from $\mathbf{P_0}$ to $\mathbf{P_1}$. Let further be $\mathbf{t_0}$ the normalized tangent vector at $\mathbf{P_0}$ and $\mathbf{t_1}$ the normalized tangent vector at $\mathbf{P_1}$. Then there must be a unit vector $\mathbf{u}$ and a scaling factor $s$ such that:

$$s \cdot \mathbf{t_0} + s \cdot \mathbf{t_1} + s \cdot \mathbf{u} = \mathbf{v}. \tag{6.7}$$

Equation (6.7) and the condition that $\mathbf{u}$ is a unit vector ($|\mathbf{u}| = 1$) together
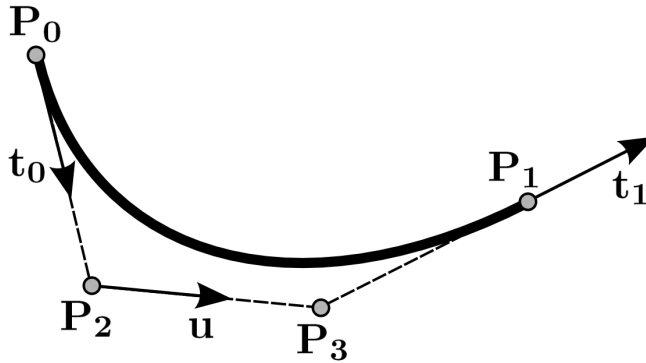
***Figure 6.7:*** *Interpolation of an artery's centerline between two adjacent vessel segments. A cubic Bezier curve is calculated. Points $\mathbf{P_0}$ and $\mathbf{P_1}$ together with normalized tangential vectors $\mathbf{t_0}$ and $\mathbf{t_1}$ are known from segment fitting. The two missing control points $\mathbf{P_2}$ and $\mathbf{P_3}$ are calculated using the assumption that the distances $\overline{\mathbf{P_0P_2}}$, $\overline{\mathbf{P_2P_3}}$, and $\overline{\mathbf{P_3P_1}}$ have equal length.*

define a system of four equations. The solution consists of the scaling factor $s$ and the three coordinates of the unit vector $\mathbf{u}$. This solution ensures an equal distance between $\overline{\mathbf{P_0P_2}}$, $\overline{\mathbf{P_2P_3}}$, and $\overline{\mathbf{P_3P_1}}$. For some configurations the system of equations has no solution. However, solutions do exist for all possible spatial configurations of coronary artery segments as they are calculated by the algorithm described above.

## 6.4 Evaluation Framework

Evaluation of the presented algorithm was performed at the MICCAI 2008 workshop "3D Segmentation in the Clinic: a Grand Challenge II". For this workshop an elaborate evaluation framework was introduced by the workshop organizers. In this section this framework is outlined and the selection of the correct reference vessels is described.

### 6.4.1 Evaluation Framework

A database of 32 CTA datasets was provided for testing coronary artery centerline extraction algorithms. For each dataset the centerline and radii were manually defined. This was done for the right coronary artery (RCA), the left descending anterior coronary artery (LDA), the left circumflex coronary artery (LCx), and one additional larger side branch of the coronary artery tree. Thus, a total set of 32 (datasets) × 4 (vessels) = 128 reference

coronary arteries were generated by the workshop organizers. The manual
annotation was performed by three different observers. From the three dif-
ferent annotations a reference standard (ground truth) was derived as well
as inter-observer variances.

The 32 CTA datasets (which are representative for clinical practice) were
split into three groups:

- **Training datasets:** Datasets 00 – 07 including the reference standard
  were available for all participants before the workshop. These datasets
  could be used for experimenting and tuning the algorithm.

- **Testing-1 datasets:** Datasets 08 – 23 without reference standards
  were available for all participants before the workshop. Workshop par-
  ticipants had to run their coronary centerline extraction algorithms on
  these datasets. The results had to be submitted before the workshop.

- **Testing-2 datasets:** Datasets 24 – 31 were not available before the
  workshop. These datasets were made available (without reference
  standard) at the beginning of the workshop. Workshop participants
  had a few hours time to run their algorithms directly at the workshop
  and submit their results.

The evaluation of the different algorithms is based on six different mea-
sures. Three different overlap measures and three different accuracy mea-
sures:

- The first overlap measure, **overlap (OV)**, measures the complete
  overlap of a calculated centerline with the reference centerline. An
  overlap is considered if the computed centerline is within the reference
  radius of the reference centerline.

- The **overlap until first error (OF)** measures the overlap with the
  reference until the first (most proximal) error (i.e., a non-overlap) oc-
  curs.

- Coronary arteries with a diameter larger than 1.5mm are assumed to
  be clinically relevant. The last overlap measure, **the overlap with
  the clinically relevant part of the vessel (OT)** measures the
  percentage of overlap with the part of the vessel where it reaches (from
  distal to proximal) the first time a diameter of at least 1.5mm.

- The first accuracy measure is the **average distance (AD)**. It is the
  average distance between the calculated and the reference centerlines.

- The **average distance inside a vessel (AI)** measures the average
  distance only in those parts where an overlap occurs.

- The **average distance to the clinically relevant part of a vessel (AT)** measures the average distance between centerlines within clinically relevant parts of the vessel (with a diameter of at least 1.5mm).

Based on these measures a scoring system scores each method by taking into account the inter-observer variations. The scoring is defined such that a scoring of 100 corresponds to a perfect accordance with the reference. A scoring of 50 indicates approximately a performance close to inter-observer variability. A score of 0 means that the method completely failed. The ranking of individual algorithms is based on the scoring system. For scoring and ranking only the testing-1 and testing-2 datasets were used. No reference standards are publicly available for these datasets. Ranking and scoring is calculated for each measure and each vessel (of testing datasets 08 – 31). Thus, a total of 24 (datasets) $\times$ 4 (vessels) $\times$ 6 (measures) = 576 ranks and scores are calculated for each algorithm. The comparison of algorithms is based on these ranks.

The algorithms that were compared in the workshop were classified into three different categories:

1. Fully automatic methods (no user interaction).

2. Semi-automatic methods (limited user interaction).

3. Interactive methods (any user interaction).

For detailed information about the workshop environment including evaluation measures and scoring please refer to the workshop description [41]. A detailed comparison of the different workshop methods and general conclusions can be found in a recent publication [52]. Since 2008 the Rotterdam Coronary Artery Algorithm Evaluation Framework [50] is publicly available. This platform enables researchers to register a team, download the datasets and compare their results with others.

### 6.4.2   Selection of Reference Vessels

For evaluation purposes the reference centerline has to be selected that corresponds to an automatically extracted centerline. Therefore the evaluation framework provides for each reference vessel two individual points that both lie on the reference centerline. Point **A** represents a point close to the distal end of the vessel. Point **B** lies close to the aorta at a proximal location on the centerline. Workshop participants could freely choose a method to select the correct reference by using points **A** and **B**.

The results presented below were achieved by applying the following procedure for selecting the correct reference vessel: For a given point **A** the closest computed vessel with a distance of less than 5mm was selected. If no vessel was closer than 5mm to point **A**, point **B** was used. If there

| Dataset | 08 | 11 | 14 | 19 | 22 | 23 | 26 | 29 | 30 |
|---------|-----|----|----|----|----|----|-----------|----|----|
| Vessel | 1, 2 | 3 | 3 | 1 | 1 | 2 | 1, 2, 3, 4 | 2 | 1 |

**Table 6.1:** *Reference vessel selection using the (proximal) point* **B**.

was also no vessel closer than 5mm to point **B** the vessel was not detected. For 13 out of the 96 reference vessels of datasets 08 – 31 point **B** was used for selection. More precisely point **B** was used for the vessels listed in table 6.1. All remaining vessels of testing datasets were identified using point **A**. The selection of point **B** already indicates a relatively bad result. Point **A** suggests a good result.

## 6.5 Results

As an example the result for a single dataset is illustrated in figure 6.8. It shows the roughly registered model together with the extracted coronary artery segments. Each segment is illustrated by a center point together with a circle that indicates the calculated radius and orientation of the respective segment.

Results for testing datasets 08 – 31 reach an average scoring of 38.0 for accuracy measures and a scoring of 52.6 for overlap measures. Tables 6.2, 6.3, and 6.4 summarize the results for the testing datasets.

An illustration of the overlap measure (OV) for all vessels of the testing datasets is shown in figure 6.9. Figure 6.10 shows the accuracy for overlapping regions (AI measure). Detailed results per vessel are listed in appendix A. The tables in appendix A also show for each vessel and measure the ranking with respect to other workshop participants.

A comparison with other methods presented at the workshop is given in table 6.5. The model-based approach presented in this work (Zambal et al.) had the third best average ranking with respect to all methods. It outperformed all other automatic and all semi-automatic methods.

The workshop framework provides a classification of datasets with respect to image quality and severity of calcifications. Table 6.6 shows the rankings of Zambal et al. for different subsets of testing datasets. Rankings shown in the table are integer numbers that are derived from sorting the methods by their average rankings. The conclusions that can be drawn from this table are: Zambal et al. outperform other automatic methods if the calcium score is low, or moderate, or all images with respect to calcium score are considered. However, in the case of severe calcifications (all image qualities) the method is ranked second among the automatic methods. In case of severe calcifications and poor image quality the method produces only the third best results among automatic methods. However, it has to be stated that only one dataset had poor image quality and severe calcium
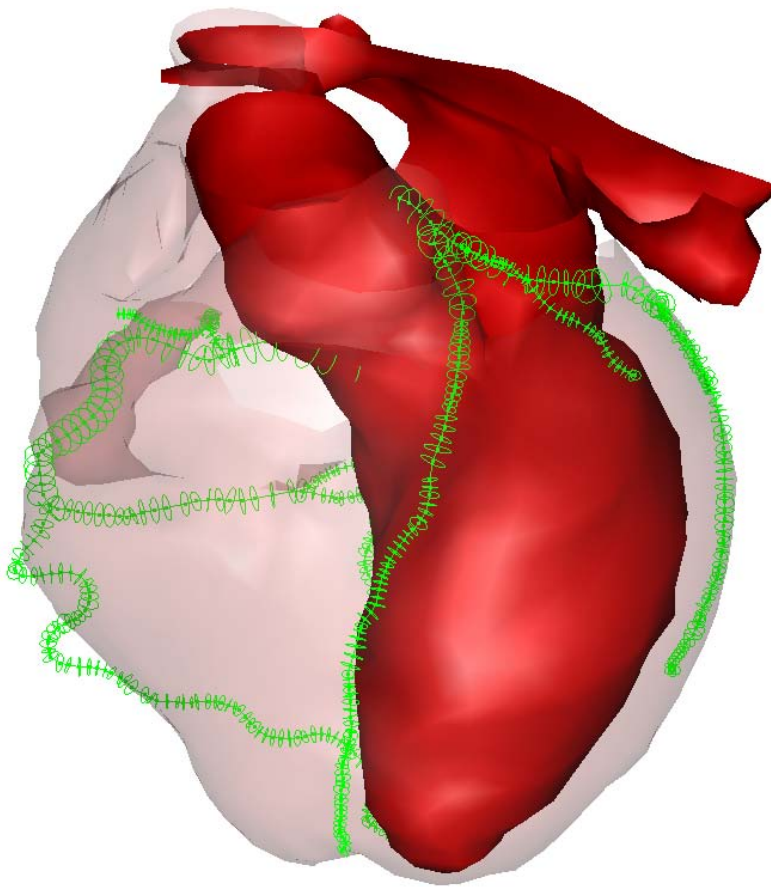
**Figure 6.8:** *Coronary artery tracking: The result for dataset 11 (matched model and extracted coronary arteries).*
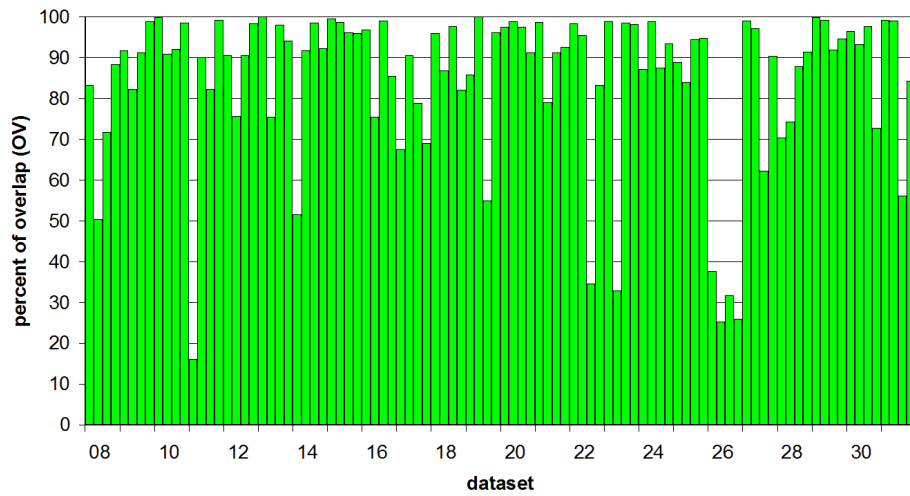
**Figure 6.9:** *Results of coronary artery tracking on all 24 testing datasets.
The percentage of overlap (OV) is plotted for all four vessels of each dataset.*

score. In table 6.6 relatively small subsets of the testing datasets are considered. The resulting questionable statistical reliability has to be taken into account here.
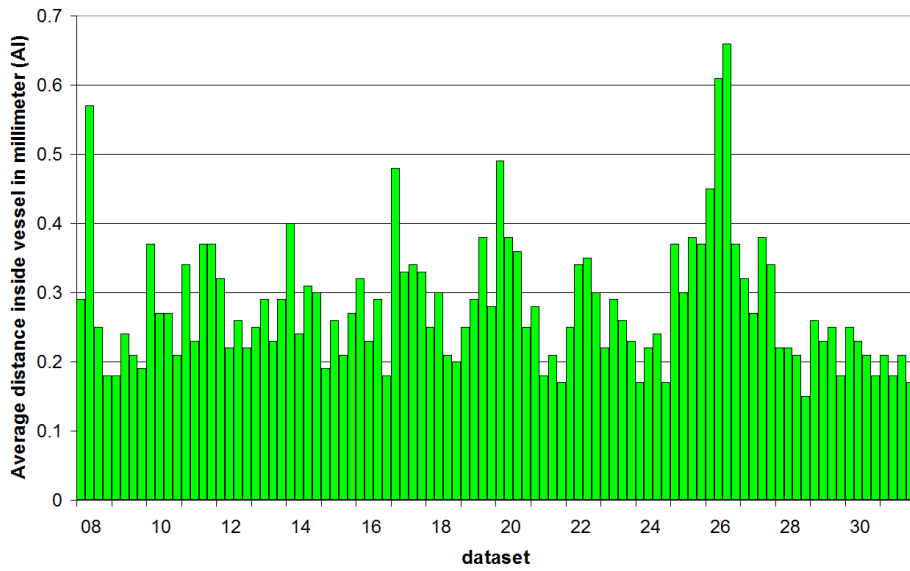
***Figure 6.10:*** *Results of coronary artery tracking on all 24 testing datasets. The average distance to the reference segmentation inside the vessel (AI) is plotted for all four vessels of each dataset.*

| Dataset | OV | % | score | rank | OF | % | score | rank | OT | % | score | rank | Avg. |
|---------|----|------|-------|------|----|------|-------|------|----|------|-------|-------|------|
| 08 | | 73.4 | 39.8 | 7.75 | | 62.7 | 41.7 | 3.75 | | 76.0 | 40.7 | 7.25 | 6.25 |
| 09 | | 91.1 | 55.3 | 7.00 | | 89.8 | 67.8 | 3.75 | | 93.6 | 72.4 | 5.25 | 5.35 |
| 10 | | 95.4 | 49.1 | 5.50 | | 76.6 | 64.3 | 2.50 | | 95.8 | 73.4 | 3.75 | 3.92 |
| 11 | | 71.9 | 36.7 | 8.75 | | 52.8 | 52.1 | 5.50 | | 72.1 | 49.3 | 8.00 | 7.42 |
| 12 | | 88.8 | 45.8 | 8.00 | | 25.8 | 14.5 | 7.00 | | 92.3 | 46.8 | 7.00 | 7.33 |
| 13 | | 91.9 | 58.9 | 6.50 | | 70.7 | 48.6 | 6.25 | | 92.6 | 59.0 | 6.50 | 6.42 |
| 14 | | 83.6 | 42.2 | 8.50 | | 71.8 | 64.0 | 4.00 | | 86.1 | 62.5 | 7.00 | 6.50 |
| 15 | | 97.6 | 58.9 | 6.00 | | 89.2 | 70.7 | 4.50 | | 98.8 | 83.5 | 3.75 | 4.75 |
| 16 | | 89.2 | 48.8 | 7.50 | | 72.6 | 48.1 | 6.50 | | 92.4 | 59.6 | 6.00 | 6.67 |
| 17 | | 76.5 | 39.4 | 9.75 | | 24.2 | 13.0 | 7.25 | | 77.4 | 39.4 | 10.00 | 9.02 |
| 18 | | 90.6 | 46.1 | 7.75 | | 72.6 | 61.6 | 5.50 | | 92.2 | 71.6 | 4.75 | 6.00 |
| 19 | | 84.3 | 56.1 | 7.75 | | 79.4 | 66.0 | 5.25 | | 84.9 | 56.0 | 7.25 | 6.73 |
| 20 | | 96.3 | 54.6 | 3.75 | | 37.7 | 21.5 | 6.00 | | 98.6 | 56.6 | 2.75 | 4.15 |
| 21 | | 90.4 | 51.4 | 8.25 | | 95.4 | 66.8 | 5.25 | | 96.1 | 60.8 | 6.50 | 6.65 |
| 22 | | 77.9 | 39.3 | 8.75 | | 77.3 | 51.2 | 6.75 | | 79.8 | 64.9 | 7.00 | 7.50 |
| 23 | | 82.2 | 46.1 | 7.25 | | 71.0 | 60.8 | 5.75 | | 83.7 | 67.0 | 5.00 | 6.00 |
| 24 | | 91.8 | 51.6 | 6.50 | | 76.0 | 72.3 | 3.25 | | 97.2 | 86.1 | 2.00 | 3.92 |
| 25 | | 90.5 | 45.7 | 6.25 | | 39.1 | 19.7 | 7.00 | | 92.7 | 46.4 | 6.00 | 6.40 |
| 26 | | 30.1 | 15.7 | 9.25 | | 14.8 | 11.0 | 4.50 | | 30.6 | 15.9 | 9.50 | 7.73 |
| 27 | | 87.2 | 60.6 | 4.50 | | 37.2 | 35.2 | 7.50 | | 87.4 | 57.2 | 4.50 | 5.50 |
| 28 | | 81.0 | 42.3 | 9.00 | | 81.4 | 44.0 | 7.25 | | 88.0 | 45.3 | 9.25 | 8.50 |
| 29 | | 96.4 | 59.4 | 4.50 | | 75.7 | 63.5 | 2.75 | | 98.0 | 86.5 | 1.50 | 2.92 |
| 30 | | 90.0 | 59.5 | 7.25 | | 90.0 | 68.7 | 5.25 | | 93.6 | 72.1 | 6.00 | 6.17 |
| 31 | | 84.7 | 63.2 | 9.00 | | 83.6 | 54.5 | 5.25 | | 88.9 | 69.6 | 5.00 | 6.42 |
| **Avg.** | | **84.7** | **48.6** | **7.29** | | **65.3** | **49.2** | **5.34** | | **87.0** | **60.1** | **5.90** | **6.18** |

**Table 6.2**: *Average overlap per dataset*

| Dataset | AD | mm | score | rank | AI | mm | score | rank | AT | mm | score | rank | Avg. |
|---------|----|----|-------|------|----|----|-------|------|----|----|-------|------|------|
| 08 | | 3.93 | 36.8 | 4.75 | | 0.32 | 48.3 | 3.50 | | 3.75 | 38.0 | 4.75 | 4.35 |
| 09 | | 0.95 | 40.0 | 2.75 | | 0.20 | 43.9 | 2.75 | | 0.80 | 41.1 | 2.75 | 2.75 |
| 10 | | 0.47 | 36.0 | 3.00 | | 0.28 | 37.7 | 4.25 | | 0.46 | 35.4 | 3.00 | 3.42 |
| 11 | | 7.03 | 31.1 | 6.50 | | 0.33 | 44.0 | 3.00 | | 6.96 | 31.2 | 6.50 | 5.33 |
| 12 | | 1.22 | 37.0 | 3.00 | | 0.26 | 41.2 | 2.75 | | 0.53 | 38.3 | 3.00 | 2.92 |
| 13 | | 1.15 | 40.7 | 3.25 | | 0.27 | 44.1 | 3.00 | | 1.13 | 41.3 | 3.25 | 3.15 |
| 14 | | 2.03 | 37.9 | 5.25 | | 0.31 | 44.2 | 3.25 | | 1.67 | 38.7 | 5.00 | 4.50 |
| 15 | | 0.34 | 41.8 | 3.25 | | 0.23 | 42.7 | 3.50 | | 0.29 | 42.6 | 3.25 | 3.33 |
| 16 | | 1.44 | 37.5 | 2.75 | | 0.26 | 41.9 | 2.50 | | 1.29 | 37.8 | 2.75 | 2.67 |
| 17 | | 4.30 | 33.7 | 6.25 | | 0.37 | 42.6 | 5.00 | | 4.31 | 33.9 | 6.25 | 5.85 |
| 18 | | 1.37 | 37.9 | 3.50 | | 0.24 | 41.6 | 3.75 | | 1.29 | 38.4 | 3.50 | 3.58 |
| 19 | | 4.26 | 38.0 | 5.50 | | 0.30 | 44.7 | 3.50 | | 4.21 | 38.2 | 5.50 | 4.83 |
| 20 | | 0.69 | 41.6 | 2.50 | | 0.37 | 43.0 | 3.00 | | 0.39 | 42.6 | 2.50 | 2.67 |
| 21 | | 1.45 | 37.2 | 3.25 | | 0.21 | 40.8 | 3.25 | | 0.58 | 39.1 | 3.25 | 3.25 |
| 22 | | 5.06 | 29.7 | 5.75 | | 0.31 | 37.3 | 3.75 | | 4.86 | 30.2 | 5.75 | 5.08 |
| 23 | | 5.75 | 35.9 | 4.75 | | 0.25 | 41.9 | 2.75 | | 4.76 | 36.5 | 4.75 | 4.08 |
| 24 | | 0.93 | 38.3 | 2.50 | | 0.20 | 41.3 | 3.00 | | 0.23 | 40.3 | 2.50 | 2.65 |
| 25 | | 0.84 | 32.0 | 3.75 | | 0.35 | 35.1 | 4.00 | | 0.68 | 32.6 | 3.75 | 3.83 |
| 26 | | 29.26 | 17.5 | 8.75 | | 0.52 | 53.0 | 3.50 | | 28.23 | 17.8 | 8.75 | 6.97 |
| 27 | | 2.91 | 36.2 | 2.75 | | 0.33 | 40.5 | 3.50 | | 2.90 | 36.7 | 2.75 | 3.00 |
| 28 | | 2.95 | 31.3 | 4.25 | | 0.20 | 38.3 | 3.25 | | 1.36 | 34.0 | 3.75 | 3.75 |
| 29 | | 0.42 | 39.1 | 2.75 | | 0.23 | 40.3 | 3.25 | | 0.36 | 39.6 | 2.50 | 2.83 |
| 30 | | 1.14 | 36.8 | 2.75 | | 0.22 | 40.7 | 2.75 | | 0.68 | 38.1 | 2.75 | 2.77 |
| 31 | | 4.97 | 31.6 | 4.75 | | 0.19 | 37.1 | 3.25 | | 4.53 | 32.8 | 4.25 | 4.10 |
| **Avg.** | | **3.54** | **35.6** | **4.09** | | **0.28** | **41.9** | **3.33** | | **3.18** | **36.5** | **4.03** | **3.82** |

*Table 6.3*: *Average accuracy per dataset*

| Measure | % / mm | | | score | | | rank | | |
|---------|--------|--------|--------|--------|--------|--------|--------|--------|--------|
| | min. | max. | avg. | min. | max. | avg. | min. | max. | avg. |
| AD | 0.19 mm | 37.88 mm | 3.54 mm | 9.9 | 48.8 | 35.6 | 1 | 13 | 4.09 |
| AI | 0.15 mm | 0.66 mm | 0.28 mm | 30.2 | 65.7 | 41.9 | 1 | 11 | 3.33 |
| AT | 0.16 mm | 33.91 mm | 3.18 mm | 9.9 | 48.8 | 36.5 | 1 | 13 | 4.03 |
| OV | 16.1% | 100.0% | 84.7% | 8.3 | 100.0 | 48.6 | 1 | 13 | 7.29 |
| OF | 4.2% | 100.0% | 65.3% | 2.1 | 100.0 | 49.2 | 1 | 13 | 5.34 |
| OT | 16.2% | 100.0% | 87.0% | 8.3 | 100.0 | 60.1 | 1 | 13 | 5.90 |
| **Total** | | | | | | | **1** | **13** | **5.00** |

***Table 6.4:*** *Coronary artery tracking results: Summary*

| Method | Challenge | | | Overlap rank | Accuracy rank | Avg. rank |
|---|---|---|---|---|---|---|
| | 1 | 2 | 3 | | | |
| Friman et al. [24] | | | × | 2.07 | 1.42 | 1.75 |
| Szymczak [64] | | | × | 4.21 | 2.35 | 3.28 |
| Zambal et al. [77] | × | | | 6.17 | 3.82 | 4.99 |
| Krissian et al. [37] | | × | | 4.31 | 7.94 | 6.13 |
| Bauer and Bischof [3] | × | | | 5.39 | 7.29 | 6.34 |
| Tek et al. [66] | × | | | 7.69 | 5.74 | 6.72 |
| Metz et al. [40] | | | × | 5.30 | 8.17 | 6.73 |
| Kitslaar et al. [34] | × | | | 8.56 | 5.75 | 7.15 |
| Dikici et al. [19] | | × | | 6.95 | 9.11 | 8.03 |
| Wang and Smedby [71] | × | | | 8.71 | 8.36 | 8.53 |
| Zhang et al. [79] | | | × | 7.52 | 10.33 | 8.92 |
| Hoyos et al. [26] | | | × | 9.05 | 8.91 | 8.98 |
| Castro et al. [7] | | × | | 10.42 | 11.77 | 11.10 |

**Table 6.5:** *Coronary artery tracking: Comparison of different methods. The column "Challenge" indicates the type of the method: (1) fully automatic, (2) semi-automatic, and (3) interactive.*

| Calcium score / Image quality | all | low | moderate | severe |
|---|---|---|---|---|
| all | 3 / 1 | 3 / 1 | 3 / 1 | 5 / 2 |
| good | 3 / 1 | 3 / 1 | 3 / 1 | - |
| moderate | 3 / 1 | 4 / 1 | 3 / 1 | 3 / 1 |
| poor | 4 / 1 | 6 / 1 | 2 / 1 | 7 / 3 |

**Table 6.6:** *The above table illustrates the final rankings of Zambal et al. when the evaluation is restricted to only subsets of all testing datasets. Each subset is defined by a specific image quality and severity of calcification. Each cell contains two values: The first value is the final ranking with respect to all the 13 methods (including semi-automatic and interactive approaches). The second value is the final ranking with respect to the 5 automatic methods. A value of 3 means that the method lead to the third lowest average ranking. None of the testing datasets had good image quality and severe calcifications. This is why the respective cell in the table is empty.*

## 6.6   Conclusion

We have outlined a method for automatic centerline extraction of the coronary artery tree in CTA. The three most critical issues in vessel tracking probably are vesselness estimation, termination criterion, and branching. In

the presented approach we handle these issues by putting multiple texture samples into relation for vesselness estimation. For this we avoid the use of a sample mean of gray values because of its sensitivity to outliers. Instead we apply a method which evaluates the separability of histograms. Noise estimation is performed to achieve an effective termination criterion. Branching is handled by applying a depth-first search where new branches are selected after few tracking iterations have been performed. Overlap measures achieved with the model-based approach of Zambal et al. are partially slightly worse than overlaps from other automatic methods. However, the great advantage of the method is its high accuracy. Because of this the method was ranked best among the automatic methods. It could even outperform many of the interactive and semi-interactive methods.

# Chapter 7

# Summary and Conclusions

## 7.1 Summary

Computed tomography and Magnetic Resonance Imaging nowadays offer great possibilities. Temporal and spatial resolutions are continuously improving. For many applications in cardiology a satisfying image quality is already achieved with present scanner technology. In daily clinical routine a huge amount of image data is generated from which important relevant information has to be derived. Currently this leads to considerable overhead: tedious manual postprocessing and annotation of medical images has to be performed. The goal is to reduce this overhead. Automatic image segmentation algorithms are developed to achieve this goal. Automatic methods do not only support the clinician by reducing workload but also improve standardization and quality control of medical image analysis.

Initialization of model-based cardiac MR segmentation was presented in chapter 2. The initial placement is crucial for starting the algorithm that fits the model accurately to the image. Results of the presented method are comparable to manual initializations performed by five different users.

A two-component approach to shape modeling was introduced in chapter 3. This model is especially designed for 3D MRI studies of the left ventricle. Individual 2D models are combined in 3D by a centerline model. The results are better than those of a standard 3D Active Appearance Model. An extended two-component model was presented in chapter 4. The extended model is bi-temporal and the right ventricle is additionally included.

In Chapter 5 an information theoretic approach to texture modeling was presented. The idea behind entropy-optimization is to reduce the influence of brightness and contrast variations in different images. An optimal texture transformation is calculated which optimizes the information content of a set of images with predefined correspondences. For different data (heart, spine, brain ventricles) it is shown that the proposed model is more robust than standard Active Appearance Models.

In chapter 6 a model-based technique for automatic coronary artery tracking was introduced. Two different models at different scales are used. A large-scale model of the complete heart is fitted to a volume in order to determine regions of interest for coronary artery origins. A small-scale model representing coronary artery segments is iteratively matched. To effectively cope with low contrast, an adaptive thresholding is used to evaluate matching accuracy of small-scale vessel segment models. In a comparison with four other automatic coronary artery segmentation algorithms, the method presented in chapter 6 achieves the best results.

## 7.2 Conclusions

Four major conclusions can be drawn from this thesis:

**Conclusion 1: Use prior knowledge!** Medical image segmentation is the bottleneck for many interesting applications including visualization, surgery planning, and extraction of relevant clinical properties. Medical image segmentation is in many cases very hard to perform and requires even in case of human operators a high level of experience. Automatic medical image segmentation will only be really successful when incorporating prior knowledge.

**Conclusion 2: Use effective model representation!** The use of prior knowledge leads to the question how such prior knowledge can be optimally represented. Typically a model is used which optimally contains the necessary information about the segmented organs. The question is how to represent such a model in an optimal way. Occham's theorem is an interesting answer to this question. It states that if multiple theories describe a phenomenon equally well, then the simplest of these theories should be used. Although Occham's theorem dates back to the Middle Ages, information theory makes it possible to formulate it in a modern way. By describing complexity by information entropy, the optimal model representation can be identified. Using minimal entropy to find an optimal texture model was proposed in chapter 5. In general the consideration of entropy is very promising for the formulation of expressive models for effective automatic image segmentation.

**Conclusion 3: Use statistics and probability theory!** The environment of image segmentation algorithms usually contains multiple sources of uncertainty: Weak definitions of the segmented objects, noise and image artifacts, complex pathologies, etc. Such uncertainty is difficult to handle and requires adequate methods. Statistics and probability theory are well-established mathematical frameworks. It is worth to formulate segmentation problems within these frameworks and to build on these. Especially Bayesian reasoning is a very promising technique from probability theory. It is the basis for many popular probabilistic models such as Markov Chains or Markov Random Fields.

**Conclusion 4: Use adaptiveness!** *Every* segmentation algorithm has a set of parameters which influences the segmentation result. Often it is very difficult to find suitable parameters to let the algorithm produce reasonable results. The optimal way of designing a segmentation algorithm is to keep the number of parameters low. Adaptiveness can help here. By making a segmentation algorithm adaptive, this does not only reduce the number of parameters, it also increases robustness. An example for adaptiveness is the entropy-optimized texture model proposed in chapter 5. In standard Active Appearance Models a texture normalization has to be performed in each iteration of the model matching process. This requires the selection of a specific normalization procedure. In the entropy-optimized texture model the transformation of gray values is adaptively re-estimated in each step. Since random transformations are possible, the model adaptively selects a

texture transformation which fits the current model shape. In a similar way the threshold for vessel segment matching in chapter 6 is determined adaptively.

**Conclusion 5: Perform comparative evaluations!** New evaluation and comparison standards, open evaluation frameworks, and reference databases are needed to push forward the state of the art in medical image analysis. Frameworks like the one used in chapter 6 allow a comparative evaluation of different approaches and helps to increase robustness and efficiency of existing algorithms.

# Bibliography

[1] S. K. Balci, P. Golland, M. Shenton, and W. M. Wells. Free-form B-spline deformation model for groupwise registration. In *Medical Image Computing and Computer–Assisted Intervention (Statistical Registration Workshop)*, pages 23–30, 2007.

[2] D. Baraff and A. Witkin. Large steps in cloth simulation. *ACM Computer Graphics*, 32:43–54, 1998.

[3] C. Bauer and H. Bischof. Edge based tube detection for coronary artery centerline extraction. *Midas Journal*, 2008. Available online at http://www.midasjournal.org/browse/publication/248, March 2009.

[4] R. Beichel, H. Bischof, F. Leberl, and M. Sonka. Robust active appearance models and their application to medical image analysis. *IEEE Transactions on Medical Imaging*, 24(9):1151–1169, 2005.

[5] C. M. Bishop. *Pattern Recognition and Machine Learning*. Springer, 2006.

[6] J. F. Canny. A variational approach to edge detection. In *AAAI Conference on Artificial Intelligence*, pages 54–58, 1983.

[7] C. Castro, M. Luengo-Oroz, A. Santos, and M. Ledesma-Carbayo. Coronary artery tracking in 3D cardiac CT images using local morphological reconstruction operators. *Midas Journal*, 2008. Available online at http://www.midasjournal.org/browse/publication/266, March 2009.

[8] J. Cates, P. T. Fletcher, M. Styner, M. Shenton, and R. Whitaker. Shape modeling and analysis with entropy-based particle systems. In *Information Processing in Medical Imaging*, pages 333–345, 2007.

[9] M. D. Cerqueira, N. J. Weissman, V. Dilsizian, A. K. Jacobs, S. Kaul, W. K. Laskey, D. J. Pennell, J. A. Rumberger, T. Ryan, and M. S. Verani. Standardized myocardial segmentation and nomenclature for tomographic imaging of the heart. *Circulation*, 105(4):539–42, 2002.

[10] T. F. Chan and L. A. Vese. Active contours without edges. *Transactions on Image Processing*, 10(2):266–277, 2001.

[11] C. Chartrand-Lefebvre, A. Cadrin-Chenevert, E. Bordeleau, P. Ugolini, R. Quellet, J.-L. Sablayrolles, and J. Prenovault. Coronary computed tomography angiography: Overview of technical aspects, current concepts, and perspectives. *Canadian Association of Radiologists Journal*, 58(2):92–108, 2007.

[12] T. Cootes, C. Twining, and C. Taylor. Diffeomorphic statistical shape models. In *British Machine Vision Conference*, volume 1, pages 447–456, 2004.

[13] T. Cootes, C. Twining, V.Petrović, R.Schestowitz, and C. Taylor. Groupwise construction of appearance models using piece-wise affine deformations. In *British Machine Vision Conference*, volume 2, pages 879–888, 2005.

[14] T. F. Cootes, G. J. Edwards, and C. J. Taylor. Active appearance models. In *European Conference on Computer Vision*, volume 2, pages 484–498, 1998.

[15] T. F. Cootes, C. J. Taylor, D. H. Cooper, and J. Graham. Active shape models: Their training and application. *Computer Vision and Image Understanding*, 61(1):38–59, 1995.

[16] C. Davatzikos, X. Tao, and D. Shen. Hierarchical active shape models, using the wavelet transform. *IEEE Transactions on Medical Imaging*, 22(3):414–423, 2003.

[17] E. Davies. A modified Hough scheme for general circle location. *Pattern Recognition Letters*, 7(1):37–43, 1988.

[18] M. de Bruijne and M. Nielsen. Shape particle filtering for image segmentation. In *Medical Image Computing and Computer–Assisted Intervention*, pages 168–175, 2004.

[19] E. Dikici, T. O'Donnell, L. Grady, R. Setser, and R. D. White. Coronary artery centerline tracking using axial symmetries. *Midas Journal*, 2008. Available online at http://www.midasjournal.org/browse/publication/257, March 2009.

[20] R. Donner, B. Micušík, G. Langs, and H. Bischof. Sparse MRF appearance models for fast anatomical structure localisation. In *British Machine Vision Conference*, pages 1080–1089, 2007.

[21] A. A. Efros and T. K. Leung. Texture synthesis by non-parametric sampling. In *International Conference on Computer Vision*, pages 1033–1038, 1999.

Bibliography

[22] P. F. Felzenszwalb and J. D. Schwartz. Hierarchical matching of deformable shapes. In *Computer Vision and Pattern Recognition*, pages 1–8, 2007.

[23] M. Figueiredo and J. Leitao. A nonsmoothing approach to the estimation of vessel contours in angiograms. *IEEE Transactions on Medical Imaging*, 14(1):162–172, 1995.

[24] O. Friman, C. Kühnel, and H.-O. Peitgen. Coronary centerline extraction using multiple hypothesis tracking and minimal paths. *Midas Journal*, 2008. Available online at http://www.midasjournal.org/browse/publication/263, March 2009.

[25] E. J. Halpern. *Clinical Cardiac CT*. Thieme Medical Publishers, 2008.

[26] M. H. Hoyos, M. A. Zuluaga, M. Lozano, J. C. Prieto, P. C. Douek, I. E. Magnin, and M. Orkisz. Coronary centerline tracking in CT images with use of an elastic model and image moments. *Midas Journal*, 2008. Available online at http://www.midasjournal.org/browse/publication/246, March 2009.

[27] J.Bogaert, S.Dymarkowski, and A.M.Taylor, editors. *Clinical Cardiac MRI*. Springer, 2005.

[28] A. Kanitsar. *Curved Planar Reformation for Vessel Visualization*. PhD thesis, Institute of Computer Graphics and Algorithms, Vienna University of Technology, 2004.

[29] M. Kass, A. Witkin, and D. Terzopoulos. Snakes: Active contour models. *International Journal of Computer Vision*, 1(4):321–331, 1988.

[30] D. G. Kendall. The diffusion of shape. *Advances in Applied Probability*, 9(3):428–430, 1977.

[31] D. G. Kendall. Shape manifolds, procrustean metrics, and complex projective spaces. *Bulletin of the London Mathematical Society*, 16(2):81–121, 1984.

[32] M. Kilian, N. J. Mitra, and H. Pottmann. Geometric modeling in shape space. In *ACM Transactions on Graphics*, volume 26, pages 641–648, 2007.

[33] C. Kirbas and F. K. H. Quek. A review of vessel extraction techniques and algorithms. *ACM Computing Surveys*, 36(2):81–121, 2004.

[34] P. H. Kitslaar, M. Frenay, E. Oost, J. Dijkstra, B. Stoel, and J. H. Reiber. Connected component and morphology

based extraction of arterial centerlines of the heart (Co-comoBeach). *Midas Journal*, 2008. Available online at http://www.midasjournal.org/browse/publication/290, March 2009.

[35] P. Kittipanya-ngam and T. F. Cootes. The effect of texture representations on aam performance. In *International Conference on Pattern Recognition*, pages 328–331, 2006.

[36] J. Koikkalainen, M. Pollari, J. Lötjönen, S. Kivistö, and K. Lauerma. Segmentation of cardiac structures simultaneously from short- and long-axis MR images. In *Medical Image Computing and Computer–Assisted Intervention*, pages 427–434, 2004.

[37] K. Krissian, H. Bogunović, J. Pozo, M. Villa-Uriol, and A. Frangi. Minimally interactive knowledge-based coronary tracking in CTA using a minimal cost path. *Midas Journal*, 2008. Available online at http://www.midasjournal.org/browse/publication/264, March 2009.

[38] G. Langs, P. Peloschek, R. Donner, and H. Bischof. Clique of active appearance models by minimum description length. In *British Machine Vision Conference*, volume 2, pages 859–868, 2005.

[39] B. P. F. Lelieveldt, S. C. Mitchell, J. G. Bosch, R. J. van der Geest, M. Sonka, and J. H. C. Reiber. Time-continuous segmentation of cardiac image sequences using active appearance motion models. In *Information Processing in Medical Imaging*, pages 446–452, 2001.

[40] C. Metz, M. Schaap, T. van Walsum, and W. Niessen. Two point minimum cost path approach for CTA coronary centerline extraction. *Midas Journal*, 2008. Available online at http://www.midasjournal.org/browse/publication/310, March 2009.

[41] C. Metz, M. Schaap, T. van Walsum, A. van der Giessen, A. Weustink, N. Mollet, G. Krestin, and W. Niessen. 3D segmentation in the clinic: A grand challenge II - coronary artery tracking. *Midas Journal*, 2008. Available online at http://www.midasjournal.org/browse/publication/245, March 2009.

[42] S. C. Mitchell, J. G. Bosch, P. F. Lelieveldt, R. J. van der Geest, J. H. C. Reiber, and M. Sonka. 3D active appearance models: Segmentation of cardiac MR and ultrasound images. *IEEE Transactions on Medical Imaging*, 21(9):1167– 1178, 2002.

[43] S. C. Mitchell, B. P. F. Lelieveldt, R. J. van der Geest, J. G. Bosch, J. H. C. Reiber, and M. Sonka. Multistage hybrid active appearance model matching: Segmentation of left and right ventricles in cardiac MR images. *IEEE Transactions on Medical Imaging*, 20(5):415–423, 2001.

[44] D. Mumford and J. Shah. Optimal approximations by piecewise smooth functions and associated variational problems. *Communications on Pure and Applied Mathematics*, 42(5):577–685, 1989.

[45] D. Nain, S. Haker, A. F. Bobick, and A. Tannenbaum. Multiscale 3d shape analysis using spherical wavelets. In *Medical Image Computing and Computer–Assisted Intervention*, pages 459–467, 2005.

[46] D. Nain, S. Haker, A. F. Bobick, and A. Tannenbaum. Shape-driven 3d segmentation using spherical wavelets. In *Medical Image Computing and Computer–Assisted Intervention*, pages 66–74, 2006.

[47] A. Nealen, M. Müller, R. Keiser, E. Boxerman, and M. Carlson. Physically based deformable models in computer graphics. *Computer Graphics Forum*, 25(4):809–836, 2006.

[48] K. Philip, E. Dove, D. McPherson, N. Gotteiner, W. Stanford, and K. Chandran. Automatic detection of myocardial contours in cine-computed tomographic images. *IEEE Transactions on Medical Imaging*, 13:241–253, 1994.

[49] K. Philip, E. Dove, D. McPherson, N. Gotteiner, W. Stanford, and K. Chandran. The fuzzy Hough transform-feature extraction in medical images. *IEEE Transactions on Medical Imaging*, 13:235–240, 1994.

[50] Rotterdam Coronary Artery Algorithm Evaluation Framework, 2008. Available online at http://coronary.bigr.nl/, March 2009.

[51] Y. Sato, S. Nakajima, H. Atsumi, T. Koller, G. Gerig, S. Yoshida, and R. Kikinis. 3D multi-scale line filter for segmentation and visualization of curvilinear structures in medical images. In *Computer Vision, Virtual Reality and Robotics in Medicine*, pages 213–222, 1997.

[52] M. Schaap, C. Metz, T. van Walsum, A. van der Giessen, A. Weustink, N. Mollet, C. Bauer, H. Bogunović, C. Castro, X. Deng, E. Dikici, T. O'Donnell, M. Frenay, O. Friman, M. H. Hoyos, P. Kitslaar, K. Krissian, C. Kühnel, M. Orkisz, M. A. Luengo-Oroz, O. Smedby, M. Styner, A. Szymczak, H. Tek, C. Wang, S. Warfield, S. Zambal, Y. Zhang, G. Krestin, and W. Niessen. Standardized evaluation methodology and reference database for evaluating coronary artery centerline extraction algorithms. *Medical Image Analysis*, 2009. (to appear).

[53] M. Schaap, I. Smal, C. Metz, T. van Walsum, and W. Niessen. Bayesian tracking of elongated structures in 3D images. In *Information Processing in Medical Imaging*, pages 74–85, 2007.

[54] P. Soille. *Morphological Image Analysis*. Springer Verlag Berlin, 2002.

[55] M. Sonka, B. P. Lelieveldt, S. C. Mitchell, J. G. Bosch, R. J. V. der Geest, and J. H. Reiber. Active appearance motion model segmentation. In *Second International Workshop on Digital and Computational Video*, pages 64–68, 2001.

[56] W. Sörgel and V. Vaerman. Automatic heart localization from a 4D MRI dataset. In *Proceedings SPIE Medical Imaging*, pages 333–344, 1997.

[57] Statistik Austria. *Jahrbuch der Gesundheitsstatistik 2007*. Verlag Österreich, 2008.

[58] M. B. Stegmann. Active appearance models: Theory, extensions and cases. Master's thesis, Informatics and Mathematical Modelling, Technical University of Denmark, DTU, 2000.

[59] M. B. Stegmann. *Generative Interpretation of Medical Images*. PhD thesis, Informatics and Mathematical Modelling, Technical University of Denmark, 2004.

[60] M. B. Stegmann and H. B. W. Larsson. Motion-compensation of cardiac perfusion MRI using a statistical texture ensemble. In *Functional Imaging and Modeling of the Heart*, volume 2674, pages 151–161, 2003.

[61] M. B. Stegmann, H. Ólafsdóttir, and H. B. W. Larsson. Unsupervised motion-compensation of multi-slice cardiac perfusion MRI. *Medical Image Analysis*, 9(4):394–410, 2005.

[62] M. B. Stegmann and D. Pedersen. Bi-temporal 3D active appearance models with applications to unsupervised ejection fraction estimation. In *International Symposium on Medical Imaging*, volume 5747, pages 336–350, 2005.

[63] A. Suinesiaputra, A. F. Frangi, M. Üzümcü, J. H. C. Reiber, and B. P. F. Lelieveldt. Extraction of myocardial contractility patterns from short-axes MR images using independent component analysis. In *European Conference on Computer Vision (Workshops CVAMIA and MMBIA)*, pages 75–86, 2004.

[64] A. Szymczak. Vessel tracking by connecting the dots. *Midas Journal*, 2008. Available online at http://www.midasjournal.org/browse/publication/251, March 2009.

[65] C. J. Taylor and T. F. Cootes. Combining elastic and statistical models of appearance variation. In *European Conference on Computer Vision*, pages 149–163, 2000.

[66] H. Tek, A. Gülsün, S. Laguitton, L. Grady, D. Lesage, and G. Funka-Lea. Automatic coronary tree modeling. *Midas Journal*, 2008. Available online at http://www.midasjournal.org/browse/publication/271, March 2009.

[67] H. H. Thodberg. Minimum description length shape and appearance models. In *Information Processing in Medical Imaging*, pages 51–62, 2003.

[68] M. Üzümcü, A. Frangi, J. Reiber, and B. Lelieveldt. The use of independent component analysis in statistical shape models. In *SPIE Medical Imaging*, volume 5032, pages 375–383, 2003.

[69] H. C. van Assen, M. G. Danilouchkine, A. F. Frangi, S. Ordas, J. J. Westenberg, J. H. Reiber, and B. P. Lelieveldt. SPASM: a 3D-ASM for segmentation of sparse and arbitrarily oriented cardiac MRI data. *Medical Image Analysis*, 10(2):286–303, 2006.

[70] P. Viola and W. M. Wells. Alignment by maximization of mutual information. *International Journal of Computer Vision*, 24(2):137–154, 1997.

[71] C. Wang and Ö. Smedby. An automatic seeding method for coronary artery segmentation and skeletonization in CTA. *Midas Journal*, 2008. Available online at http://www.midasjournal.org/browse/publication/265, March 2009.

[72] K. Ward, F. Bertails, T.-Y. Kim, S. R. Marschner, M.-P. Cani, and M. Lin. A survey on hair modeling: Styling, simulation, and rendering. *IEEE Transactions on Visualization and Computer Graphics*, 13(2):213–34, Mar-Apr 2007.

[73] C. E. Wilkins, B. Bentacourt, V. S. Mathur, A. Massumi, C. M. De-Castro, E. Garcia, and R. J. Hall. Coronary artery anomalies. *Texas Heart Institute Journal*, 15(3):166–173, 1988.

[74] S. Zambal. 3D active appearance models for segmentation of cardiac MRI data. Master's thesis, Institute of Computer Graphics and Algorithms, Vienna University of Technology, 2005.

[75] S. Zambal, K. Bühler, and J. Hladůvka. Entropy-optimized texture models. In *Medical Image Computing and Computer Assisted Intervention*, pages 213–221, 2008.

[76] S. Zambal, J. Hladůvka, and K. Bühler. Improving segmentation of the left ventricle using a two-component statistical model. In *Medical Image Computing and Computer Assisted Intervention*, pages 151–158, 2006.

[77] S. Zambal, J. Hladůvka, A. Kanitsar, and K. Bühler. Shape and appearance models for automatic coronary artery tracking. *Midas Journal*, 2008. Available online at http://www.midasjournal.org/browse/publication/256, March 2009.

[78] H. Zhang. The optimality of naive Bayes. In *Florida Artificial Intelligence Research Society Conference*, 2004.

[79] Y. Zhang, K. Chen, and S. Wong. 3D interactive centerline extraction. *Midas Journal*, 2008. Available online at http://www.midasjournal.org/browse/publication/254, March 2009.

# Appendices

# Appendix A: Details Challenge Results

| | | | OV | | | OF | | | OT | |
|---|---|---|---|---|---|---|---|---|---|---|
| D | V | % | score | rank | % | score | rank | % | score | rank |
| 8 | 0 | 88.4 | 44.7 | 5 | 81.8 | 41.9 | 1 | 98.6 | 49.3 | 3 |
| 8 | 1 | 71.7 | 36.5 | 8 | 58.9 | 29.5 | 4 | 71.7 | 35.9 | 8 |
| 8 | 2 | 50.3 | 34.3 | 11 | 35.8 | 50.3 | 6 | 50.3 | 33.8 | 11 |
| 8 | 3 | 83.3 | 43.8 | 7 | 74.3 | 45 | 3 | 83.3 | 43.7 | 7 |
| 9 | 0 | 98.9 | 84.4 | 4 | 100 | 100 | 1 | 100 | 100 | 1 |
| 9 | 1 | 91.3 | 46.2 | 7 | 83.9 | 44.5 | 6 | 91.3 | 45.8 | 7 |
| 9 | 2 | 82.3 | 43.6 | 12 | 79.6 | 42.6 | 6 | 82.9 | 43.9 | 12 |
| 9 | 3 | 91.8 | 47.1 | 5 | 95.7 | 84.1 | 2 | 100 | 100 | 1 |
| 10 | 0 | 98.5 | 49.8 | 6 | 100 | 100 | 1 | 100 | 100 | 1 |
| 10 | 1 | 92.1 | 46.1 | 6 | 20.2 | 10.1 | 7 | 92.1 | 46 | 6 |
| 10 | 2 | 90.9 | 50.5 | 6 | 86.3 | 47.3 | 1 | 91.1 | 47.7 | 6 |
| 10 | 3 | 99.9 | 50 | 3 | 100 | 100 | 1 | 100 | 100 | 1 |
| 11 | 0 | 99.3 | 49.7 | 6 | 100 | 100 | 1 | 100 | 100 | 1 |
| 11 | 1 | 82.2 | 43.2 | 7 | 12.9 | 50.4 | 3 | 82.2 | 43.2 | 7 |
| 11 | 2 | 90 | 45.7 | 10 | 86.5 | 45.5 | 9 | 90.2 | 45.7 | 11 |
| 11 | 3 | 16.1 | 8.3 | 13 | 11.7 | 12.7 | 8 | 16.2 | 8.3 | 13 |
| 12 | 0 | 98.3 | 49.3 | 8 | 20.9 | 10.5 | 4 | 99.1 | 49.6 | 2 |
| 12 | 1 | 90.6 | 47.8 | 7 | 7.6 | 5.2 | 6 | 90.6 | 46.4 | 7 |
| 12 | 2 | 75.7 | 40.6 | 11 | 64 | 36.7 | 8 | 89.1 | 46 | 10 |
| 12 | 3 | 90.6 | 45.6 | 6 | 10.8 | 5.4 | 7 | 90.5 | 45.3 | 8 |
| 13 | 0 | 94.2 | 47.1 | 10 | 19.8 | 9.9 | 11 | 95.3 | 47.6 | 10 |
| 13 | 1 | 98 | 49.4 | 5 | 93 | 47.1 | 3 | 99.6 | 49.9 | 5 |
| 13 | 2 | 75.5 | 39.1 | 10 | 70.2 | 37.6 | 9 | 75.5 | 38.5 | 10 |
| 13 | 3 | 100 | 100 | 1 | 100 | 100 | 1 | 100 | 100 | 1 |
| 14 | 0 | 92.3 | 46.7 | 7 | 35.5 | 30.3 | 6 | 99.5 | 77.6 | 3 |
| 14 | 1 | 98.5 | 49.3 | 3 | 100 | 100 | 1 | 100 | 100 | 1 |
| 14 | 2 | 91.8 | 46.5 | 12 | 100 | 100 | 1 | 91.8 | 45.9 | 12 |
| 14 | 3 | 51.6 | 26.5 | 12 | 51.6 | 25.8 | 6 | 53 | 26.5 | 12 |
| 15 | 0 | 96 | 48.1 | 5 | 100 | 100 | 1 | 100 | 100 | 1 |
| 15 | 1 | 96.2 | 49.6 | 9 | 93.7 | 47.7 | 9 | 96.2 | 48.7 | 9 |
| 15 | 2 | 98.7 | 88.1 | 4 | 63 | 35.1 | 8 | 99 | 85.4 | 4 |
| 15 | 3 | 99.5 | 49.8 | 7 | 100 | 100 | 1 | 100 | 100 | 1 |

**Table A.1:** *Overlap measures for testing datasets 08 – 15*

| D | V | OV | | | OF | | | OT | | |
|---|---|------|-------|------|------|-------|------|------|-------|------|
| | | % | score | rank | % | score | rank | % | score | rank |
| 16 | 0 | 85.4 | 43.2 | 12 | 87.8 | 44.9 | 5 | 95.4 | 47.7 | 8 |
| 16 | 1 | 99.1 | 61.6 | 3 | 98.2 | 90.9 | 4 | 100 | 100 | 1 |
| 16 | 2 | 75.5 | 41.4 | 12 | 66.8 | 37.6 | 12 | 75.5 | 41.4 | 12 |
| 16 | 3 | 96.8 | 48.8 | 3 | 37.8 | 18.9 | 5 | 98.8 | 49.4 | 3 |
| 17 | 0 | 69 | 35.5 | 10 | 52.5 | 29.4 | 6 | 69 | 35.5 | 10 |
| 17 | 1 | 78.8 | 41.3 | 9 | 19.1 | 9.8 | 5 | 78.8 | 40 | 9 |
| 17 | 2 | 90.5 | 46.1 | 11 | 4.2 | 2.1 | 12 | 91.7 | 46.6 | 10 |
| 17 | 3 | 67.5 | 34.6 | 9 | 21.2 | 10.6 | 6 | 70 | 35.7 | 11 |
| 18 | 0 | 82.1 | 41.5 | 12 | 81.5 | 41.6 | 9 | 82.1 | 41.5 | 13 |
| 18 | 1 | 97.7 | 49.1 | 6 | 100 | 100 | 1 | 100 | 100 | 1 |
| 18 | 2 | 86.8 | 44.9 | 4 | 9.1 | 4.9 | 11 | 86.8 | 44.8 | 4 |
| 18 | 3 | 96 | 48.9 | 9 | 100 | 100 | 1 | 100 | 100 | 1 |
| 19 | 0 | 96.1 | 48.3 | 9 | 99 | 97.4 | 6 | 98.5 | 49.5 | 7 |
| 19 | 1 | 55 | 28 | 13 | 43.4 | 22.2 | 8 | 55 | 27.7 | 13 |
| 19 | 2 | 100 | 100 | 1 | 100 | 100 | 1 | 100 | 100 | 1 |
| 19 | 3 | 85.9 | 48 | 8 | 75.2 | 44.4 | 6 | 85.9 | 46.8 | 8 |
| 20 | 0 | 91.2 | 45.8 | 7 | 99.9 | 50 | 3 | 99.7 | 49.8 | 3 |
| 20 | 1 | 97.5 | 48.9 | 4 | 10.8 | 5.4 | 5 | 97.5 | 48.8 | 4 |
| 20 | 2 | 98.9 | 49.7 | 1 | 11.3 | 5.7 | 11 | 99.8 | 77.9 | 1 |
| 20 | 3 | 97.5 | 74.1 | 3 | 28.8 | 24.9 | 5 | 97.5 | 49.9 | 3 |
| 21 | 0 | 92.6 | 47.7 | 8 | 88.5 | 48.9 | 7 | 100 | 100 | 1 |
| 21 | 1 | 91.2 | 46 | 10 | 94 | 68.8 | 9 | 96.6 | 48.6 | 9 |
| 21 | 2 | 79 | 39.8 | 11 | 100 | 100 | 1 | 89 | 44.9 | 12 |
| 21 | 3 | 98.8 | 71.9 | 4 | 99.2 | 49.6 | 4 | 98.8 | 49.7 | 4 |
| 22 | 0 | 83.3 | 41.7 | 13 | 79.9 | 40 | 10 | 83.9 | 41.9 | 13 |
| 22 | 1 | 34.6 | 17.6 | 13 | 33.8 | 16.9 | 13 | 35.3 | 17.7 | 13 |
| 22 | 2 | 95.5 | 48.4 | 6 | 100 | 100 | 1 | 100 | 100 | 1 |
| 22 | 3 | 98.4 | 49.4 | 3 | 95.6 | 47.9 | 2 | 100 | 100 | 1 |
| 23 | 0 | 98.2 | 49.1 | 4 | 100 | 100 | 1 | 100 | 100 | 1 |
| 23 | 1 | 98.6 | 49.3 | 6 | 100 | 100 | 1 | 100 | 100 | 1 |
| 23 | 2 | 32.9 | 16.8 | 13 | 35.9 | 18.3 | 12 | 35.8 | 18.1 | 13 |
| 23 | 3 | 98.9 | 69.3 | 4 | 48.1 | 24.8 | 8 | 98.9 | 49.8 | 4 |

**Table A.2:** *Overlap measures for testing datasets 16 – 23*

| | | OV | | | OF | | | OT | | |
|---|---|---|---|---|---|---|---|---|---|---|
| **D** | **V** | **%** | **score** | **rank** | **%** | **score** | **rank** | **%** | **score** | **rank** |
| 24 | 0 | 93.5 | 47.9 | 8 | 100 | 100 | 1 | 100 | 100 | 1 |
| 24 | 1 | 87.6 | 45.2 | 5 | 7.8 | 3.9 | 7 | 88.9 | 44.5 | 5 |
| 24 | 2 | 98.9 | 67.8 | 2 | 97.9 | 96.4 | 2 | 100 | 100 | 1 |
| 24 | 3 | 87.1 | 45.5 | 11 | 98.3 | 89 | 2 | 100 | 100 | 1 |
| 25 | 0 | 94.8 | 47.6 | 6 | 6.8 | 3.8 | 12 | 97.7 | 49 | 8 |
| 25 | 1 | 94.4 | 47.9 | 2 | 36.7 | 18.3 | 2 | 95.8 | 48 | 2 |
| 25 | 2 | 84 | 42.7 | 8 | 81.6 | 40.8 | 7 | 84 | 42 | 8 |
| 25 | 3 | 88.9 | 44.6 | 9 | 31.2 | 15.7 | 7 | 93.1 | 46.6 | 6 |
| 26 | 0 | 25.9 | 14.1 | 10 | 14.8 | 17.7 | 4 | 27.8 | 15.2 | 11 |
| 26 | 1 | 31.7 | 16.6 | 7 | 4.9 | 3.6 | 5 | 31.8 | 16.6 | 7 |
| 26 | 2 | 25.2 | 12.9 | 9 | 15.8 | 8.2 | 7 | 25.2 | 12.8 | 9 |
| 26 | 3 | 37.6 | 19.1 | 11 | 23.5 | 14.4 | 4 | 37.6 | 19.1 | 11 |
| 27 | 0 | 90.4 | 45.3 | 6 | 6.2 | 3.1 | 13 | 89.9 | 44.9 | 8 |
| 27 | 1 | 62.3 | 35.1 | 7 | 18.8 | 25.8 | 7 | 62.3 | 35.1 | 7 |
| 27 | 2 | 97.1 | 73.7 | 2 | 23.9 | 12 | 9 | 97.4 | 48.9 | 2 |
| 27 | 3 | 99.1 | 88.4 | 3 | 100 | 100 | 1 | 100 | 100 | 1 |
| 28 | 0 | 91.4 | 45.7 | 12 | 85.1 | 42.6 | 12 | 91.4 | 45.7 | 13 |
| 28 | 1 | 87.9 | 45.9 | 6 | 78.3 | 46.1 | 2 | 90.5 | 46.9 | 6 |
| 28 | 2 | 74.2 | 41.5 | 8 | 73.2 | 42.9 | 7 | 81.4 | 44.2 | 8 |
| 28 | 3 | 70.4 | 36.2 | 10 | 88.9 | 44.6 | 8 | 88.7 | 44.4 | 10 |
| 29 | 0 | 94.7 | 47.6 | 6 | 91 | 45.7 | 3 | 100 | 100 | 1 |
| 29 | 1 | 91.9 | 46.1 | 3 | 12 | 8.4 | 6 | 91.9 | 46.1 | 3 |
| 29 | 2 | 99.3 | 49.9 | 4 | 100 | 100 | 1 | 100 | 100 | 1 |
| 29 | 3 | 99.9 | 94.1 | 4 | 100 | 100 | 1 | 100 | 100 | 1 |
| 30 | 0 | 72.8 | 36.7 | 13 | 66.8 | 33.4 | 12 | 80.5 | 40.3 | 13 |
| 30 | 1 | 97.7 | 87.7 | 3 | 100 | 100 | 1 | 100 | 100 | 1 |
| 30 | 2 | 93.2 | 48.1 | 9 | 95.2 | 48.3 | 7 | 93.9 | 48.3 | 9 |
| 30 | 3 | 96.5 | 65.5 | 4 | 97.9 | 93 | 1 | 100 | 100 | 1 |
| 31 | 0 | 84.3 | 42.3 | 13 | 94 | 47 | 6 | 100 | 100 | 1 |
| 31 | 1 | 56.2 | 28.5 | 12 | 41.7 | 21.4 | 8 | 56.2 | 28.5 | 12 |
| 31 | 2 | 99.1 | 92.7 | 5 | 100 | 100 | 1 | 100 | 100 | 1 |
| 31 | 3 | 99.3 | 89.1 | 6 | 98.5 | 49.7 | 6 | 99.3 | 49.8 | 6 |

**Table A.3:** *Overlap measures for testing datasets 24 – 31*

| | | AD | | | AI | | | AT | | |
|---|---|---|---|---|---|---|---|---|---|---|
| D | V | mm | score | rank | mm | score | rank | mm | score | rank |
| 8 | 0 | 0.91 | 42.8 | 2 | 0.18 | 48.1 | 1 | 0.2 | 47.5 | 2 |
| 8 | 1 | 8.04 | 35.7 | 3 | 0.25 | 49.6 | 1 | 8.04 | 35.7 | 3 |
| 8 | 2 | 5.06 | 30.6 | 10 | 0.57 | 50.8 | 9 | 5.06 | 30.6 | 10 |
| 8 | 3 | 1.69 | 38.2 | 3 | 0.29 | 44.7 | 3 | 1.69 | 38.2 | 3 |
| 9 | 0 | 0.21 | 39.3 | 2 | 0.19 | 39.7 | 2 | 0.18 | 39.8 | 2 |
| 9 | 1 | 1.28 | 41.6 | 2 | 0.21 | 45.4 | 2 | 1.28 | 41.6 | 2 |
| 9 | 2 | 1.65 | 36.8 | 2 | 0.24 | 44.5 | 2 | 1.56 | 37.1 | 2 |
| 9 | 3 | 0.65 | 42.3 | 2 | 0.18 | 45.8 | 2 | 0.18 | 45.9 | 2 |
| 10 | 0 | 0.24 | 35.9 | 2 | 0.21 | 36.3 | 2 | 0.22 | 34 | 2 |
| 10 | 1 | 0.59 | 33.9 | 3 | 0.27 | 36.5 | 5 | 0.59 | 33.9 | 3 |
| 10 | 2 | 0.7 | 43.8 | 2 | 0.27 | 47.8 | 2 | 0.68 | 43.9 | 2 |
| 10 | 3 | 0.37 | 30.2 | 3 | 0.37 | 30.2 | 5 | 0.37 | 29.9 | 3 |
| 11 | 0 | 0.38 | 33.3 | 5 | 0.37 | 33.5 | 5 | 0.37 | 33.5 | 5 |
| 11 | 1 | 1.81 | 38.3 | 3 | 0.37 | 44.2 | 3 | 1.81 | 38.3 | 3 |
| 11 | 2 | 0.62 | 42.8 | 3 | 0.23 | 45.7 | 1 | 0.6 | 42.9 | 3 |
| 11 | 3 | 25.3 | 9.9 | 13 | 0.34 | 52.4 | 1 | 25.06 | 9.9 | 13 |
| 12 | 0 | 0.25 | 34.7 | 2 | 0.22 | 35.2 | 2 | 0.24 | 34.8 | 2 |
| 12 | 1 | 0.64 | 39.8 | 2 | 0.26 | 43 | 2 | 0.64 | 39.8 | 2 |
| 12 | 2 | 3.56 | 33.5 | 3 | 0.22 | 43.6 | 3 | 0.79 | 39.3 | 3 |
| 12 | 3 | 0.45 | 40 | 2 | 0.32 | 43 | 1 | 0.46 | 39.3 | 2 |
| 13 | 0 | 0.39 | 40.3 | 2 | 0.29 | 42.4 | 2 | 0.36 | 41.6 | 2 |
| 13 | 1 | 0.26 | 39.9 | 3 | 0.23 | 40.6 | 4 | 0.23 | 40.7 | 3 |
| 13 | 2 | 3.68 | 34.6 | 4 | 0.29 | 45.5 | 2 | 3.68 | 34.6 | 4 |
| 13 | 3 | 0.25 | 48.1 | 1 | 0.25 | 48.1 | 1 | 0.25 | 48.1 | 1 |
| 14 | 0 | 1.43 | 45 | 2 | 0.3 | 48.4 | 2 | 0.31 | 48.2 | 2 |
| 14 | 1 | 0.35 | 39.8 | 2 | 0.31 | 40.3 | 3 | 0.32 | 39.5 | 2 |
| 14 | 2 | 1.07 | 46.9 | 2 | 0.24 | 50.9 | 2 | 1.08 | 46.9 | 3 |
| 14 | 3 | 5.26 | 19.8 | 12 | 0.4 | 37.4 | 3 | 4.97 | 20.3 | 11 |
| 15 | 0 | 0.49 | 44.1 | 2 | 0.27 | 45.7 | 2 | 0.27 | 45.7 | 2 |
| 15 | 1 | 0.43 | 36 | 3 | 0.21 | 37.2 | 3 | 0.43 | 36 | 3 |
| 15 | 2 | 0.26 | 38.9 | 2 | 0.26 | 39.3 | 3 | 0.27 | 40.3 | 2 |
| 15 | 3 | 0.2 | 48.2 | 2 | 0.19 | 48.4 | 2 | 0.19 | 48.3 | 2 |

**Table A.4:** *Accuracy measures for testing datasets 08 – 15*

| D | V | AD | | | AI | | | AT | | |
|---|---|------|-------|------|------|-------|------|-------|-------|------|
| | | mm | score | rank | mm | score | rank | mm | score | rank |
| 16 | 0 | 0.93 | 39.3 | 2 | 0.18 | 45.6 | 2 | 0.37 | 43.6 | 2 |
| 16 | 1 | 0.31 | 40.1 | 2 | 0.29 | 40.3 | 2 | 0.3 | 39.9 | 2 |
| 16 | 2 | 4.11 | 30.9 | 3 | 0.23 | 40.7 | 2 | 4.11 | 30.9 | 3 |
| 16 | 3 | 0.39 | 39.7 | 1 | 0.32 | 40.8 | 1 | 0.37 | 36.8 | 1 |
| 17 | 0 | 11.61 | 29.8 | 8 | 0.33 | 42.8 | 7 | 11.61 | 29.8 | 8 |
| 17 | 1 | 1.67 | 37.4 | 3 | 0.34 | 46.2 | 2 | 1.67 | 37.4 | 4 |
| 17 | 2 | 0.94 | 38.1 | 3 | 0.33 | 41.2 | 2 | 0.92 | 38.3 | 2 |
| 17 | 3 | 2.96 | 29.5 | 9 | 0.48 | 40.3 | 8 | 3.02 | 30 | 9 |
| 18 | 0 | 2.88 | 37.1 | 2 | 0.2 | 45 | 2 | 2.88 | 37.1 | 2 |
| 18 | 1 | 0.3 | 40.7 | 3 | 0.21 | 41.5 | 4 | 0.21 | 41.4 | 3 |
| 18 | 2 | 1.82 | 35.7 | 2 | 0.3 | 40.8 | 3 | 1.82 | 35.7 | 2 |
| 18 | 3 | 0.48 | 37.9 | 3 | 0.25 | 39.3 | 3 | 0.25 | 39.3 | 3 |
| 19 | 0 | 0.5 | 44 | 3 | 0.28 | 45.5 | 3 | 0.32 | 45 | 3 |
| 19 | 1 | 13.78 | 23.7 | 12 | 0.38 | 42.8 | 3 | 13.78 | 23.7 | 12 |
| 19 | 2 | 0.29 | 44.3 | 2 | 0.29 | 44.3 | 2 | 0.29 | 44.3 | 2 |
| 19 | 3 | 2.47 | 39.9 | 2 | 0.25 | 46.2 | 2 | 2.47 | 39.9 | 2 |
| 20 | 0 | 1.45 | 42.9 | 2 | 0.25 | 46.7 | 2 | 0.25 | 46.6 | 2 |
| 20 | 1 | 0.39 | 44 | 2 | 0.36 | 44.8 | 2 | 0.39 | 44 | 2 |
| 20 | 2 | 0.4 | 39 | 2 | 0.38 | 39.4 | 2 | 0.39 | 39.3 | 2 |
| 20 | 3 | 0.52 | 40.6 | 2 | 0.49 | 41.3 | 3 | 0.52 | 40.6 | 2 |
| 21 | 0 | 0.44 | 36.8 | 2 | 0.17 | 39.4 | 2 | 0.16 | 39.7 | 2 |
| 21 | 1 | 1.03 | 35.3 | 4 | 0.21 | 38.6 | 5 | 0.34 | 37.4 | 4 |
| 21 | 2 | 4.04 | 33.9 | 2 | 0.18 | 42.1 | 1 | 1.51 | 36.4 | 2 |
| 21 | 3 | 0.3 | 42.8 | 2 | 0.28 | 43 | 2 | 0.3 | 42.8 | 2 |
| 22 | 0 | 2.22 | 27.7 | 3 | 0.3 | 33.1 | 3 | 2.07 | 27.9 | 3 |
| 22 | 1 | 17.17 | 12.8 | 13 | 0.35 | 36 | 4 | 16.76 | 13.1 | 13 |
| 22 | 2 | 0.57 | 39.4 | 2 | 0.34 | 41 | 2 | 0.34 | 40.5 | 2 |
| 22 | 3 | 0.29 | 38.8 | 2 | 0.25 | 39.3 | 2 | 0.26 | 39.4 | 2 |
| 23 | 0 | 0.28 | 40 | 1 | 0.23 | 40.6 | 1 | 0.23 | 40.6 | 1 |
| 23 | 1 | 0.28 | 43.4 | 3 | 0.26 | 43.8 | 3 | 0.26 | 43.8 | 3 |
| 23 | 2 | 22.2 | 11.6 | 13 | 0.29 | 34.1 | 4 | 18.34 | 12.6 | 13 |
| 23 | 3 | 0.23 | 48.8 | 2 | 0.22 | 49.1 | 2 | 0.23 | 48.8 | 2 |

**Table A.5:** *Accuracy measures for testing datasets 16 – 23*

| D | V | AD mm | AD score | AD rank | AI mm | AI score | AI rank | AT mm | AT score | AT rank |
|---|---|-------|----------|---------|-------|----------|---------|-------|----------|---------|
| 24 | 0 | 0.89 | 36.3 | 2 | 0.17 | 38.6 | 2 | 0.17 | 38.1 | 2 |
| 24 | 1 | 0.39 | 34.1 | 2 | 0.24 | 37.3 | 3 | 0.35 | 35 | 2 |
| 24 | 2 | 0.24 | 40.4 | 2 | 0.22 | 40.8 | 2 | 0.22 | 39.6 | 2 |
| 24 | 3 | 2.18 | 42.5 | 2 | 0.17 | 48.3 | 3 | 0.17 | 48.3 | 2 |
| 25 | 0 | 0.47 | 30.6 | 4 | 0.37 | 32 | 4 | 0.4 | 31.6 | 5 |
| 25 | 1 | 0.45 | 31.8 | 2 | 0.38 | 33.2 | 4 | 0.42 | 32.1 | 2 |
| 25 | 2 | 1.3 | 35.2 | 2 | 0.3 | 41.6 | 2 | 1.3 | 35.2 | 2 |
| 25 | 3 | 1.15 | 30.3 | 3 | 0.37 | 33.8 | 2 | 0.58 | 31.7 | 2 |
| 26 | 0 | 37.88 | 18.5 | 9 | 0.37 | 59.7 | 1 | 33.91 | 19.8 | 9 |
| 26 | 1 | 30.83 | 23.3 | 6 | 0.66 | 65.7 | 1 | 30.69 | 23.3 | 6 |
| 26 | 2 | 25.84 | 13.2 | 9 | 0.61 | 50.3 | 1 | 25.84 | 13.2 | 9 |
| 26 | 3 | 22.49 | 14.9 | 11 | 0.45 | 36.4 | 11 | 22.49 | 14.9 | 11 |
| 27 | 0 | 0.45 | 41 | 2 | 0.34 | 44.4 | 3 | 0.46 | 42.6 | 2 |
| 27 | 1 | 10.53 | 25.9 | 4 | 0.38 | 38.6 | 3 | 10.53 | 25.9 | 4 |
| 27 | 2 | 0.32 | 40.6 | 1 | 0.27 | 41.6 | 2 | 0.31 | 40.8 | 1 |
| 27 | 3 | 0.33 | 37.3 | 2 | 0.32 | 37.5 | 2 | 0.32 | 37.4 | 2 |
| 28 | 0 | 1.14 | 37.5 | 2 | 0.15 | 40.9 | 2 | 1.14 | 37.5 | 2 |
| 28 | 1 | 2.21 | 31.4 | 2 | 0.21 | 35.5 | 3 | 1.45 | 32.3 | 2 |
| 28 | 2 | 3.69 | 27.9 | 5 | 0.22 | 37.2 | 2 | 2.14 | 30.6 | 4 |
| 28 | 3 | 4.76 | 28.5 | 4 | 0.22 | 39.7 | 2 | 0.72 | 35.6 | 3 |
| 29 | 0 | 0.42 | 38.4 | 2 | 0.18 | 40.3 | 2 | 0.18 | 40 | 2 |
| 29 | 1 | 0.76 | 35.4 | 2 | 0.25 | 38.1 | 3 | 0.76 | 35.4 | 2 |
| 29 | 2 | 0.24 | 40.9 | 2 | 0.23 | 41.1 | 2 | 0.24 | 41.3 | 2 |
| 29 | 3 | 0.26 | 41.4 | 2 | 0.26 | 41.5 | 2 | 0.27 | 41.4 | 2 |
| 30 | 0 | 3.42 | 31.1 | 3 | 0.18 | 42.6 | 2 | 1.79 | 34.4 | 3 |
| 30 | 1 | 0.27 | 39.3 | 2 | 0.21 | 40 | 2 | 0.21 | 40 | 2 |
| 30 | 2 | 0.51 | 36.2 | 3 | 0.23 | 38.5 | 3 | 0.46 | 36.5 | 3 |
| 30 | 3 | 0.37 | 40.4 | 1 | 0.25 | 41.5 | 2 | 0.25 | 41.6 | 2 |
| 31 | 0 | 1.93 | 31.1 | 4 | 0.17 | 36.4 | 2 | 0.17 | 36.6 | 2 |
| 31 | 1 | 17.56 | 21 | 8 | 0.21 | 37.2 | 3 | 17.56 | 21 | 8 |
| 31 | 2 | 0.19 | 39.4 | 2 | 0.18 | 39.5 | 2 | 0.19 | 38.4 | 2 |
| 31 | 3 | 0.22 | 35 | 3 | 0.21 | 35.3 | 3 | 0.22 | 35 | 3 |

**Table A.6:** *Accuracy measures for testing datasets 24 – 31*

# Appendix B: Curriculum Vitae

**Sebastian Zambal**
born on September 4$^{\text{th}}$, 1979,
in Waidhofen/Ybbs, Austria

Address:
Ybbsitzerstraße 44a,
3340 Waidhofen/Ybbs, Austria
Phone: +43 (0)676 78 21 224
eMail: sebastian.zambal@agfa.com

| | |
|---|---|
| Sept. 2008 | Developer (Clinical Applications / Cardiology) AGFA HealthCare, Vienna |
| 2005 - 2008 | Researcher at VRVis Research Center for Virtual Reality and Visualization |
| 1999 - 2005 | Study of Computer Science (Dipl.-Ing.) Vienna University of Technology |
| 1998 - 1999 | Military service (Gardemusik Wien) |
| 1990 - 1998 | Bundesrealgymnasium Waidhofen / Ybbs |
| 1986 - 1990 | Elementary school Waidhofen / Ybbs |

**Internships**

| | |
|---|---|
| Aug. - Sept. 2002 | PSE Siemens Austria |
| Mar. - July 2004 | Semester abroad (European ERASMUS student exchange program) École Nationale Supérieure de l'Aéronautique et de l'Espace, Toulouse, France |

**Prizes**

| | |
|---|---|
| Sept. 2008 | First prize in a Workshop on Segmentation (category "automatic methods") at the International Conference on Medical Image Computing and Computer Assisted Intervention (MICCAI). |

**Publications**

Sebastian Zambal, Andreas Schöllhuber, Katja Bühler, and Jiří Hladůvka. Fast and robust localization of the heart in cardiac MRI series. *International Conference on Computer Vision Theory and Applications (VISAPP)*, pages 341–346, 2008.

Sebastian Zambal, Jiří Hladůvka, and Katja Bühler. Improving Segmentation of the Left Ventricle using a Two-Component Statistical Model. *Medical Image Computing and Computer Assisted Intervention (MICCAI)*, pages 151–158, 2006.

Sebastian Zambal, Jiří Hladůvka, and Katja Bühler. A fully automatic system for segmentation and analysis of the left and right ventricles of the heart using a bi-temporal two-component model. *Computer Assisted Radiology and Surgery (CARS)*, pages 93–94, 2007.

Sebastian Zambal, Katja Bühler, and Jiří Hladůvka. Entropy-Optimized Texture Models. *Medical Image Computing and Computer Assisted Intervention (MICCAI)*, pages 213–221, 2008.

Sebastian Zambal, Jiří Hladůvka, Armin Kanitsar, and Katja Bühler. Shape and Appearance Models for Automatic Coronary Artery Tracking. *Midas Journal (presented at the MICCAI 2008 workshop "3D Segmentation in the Clinic: A Grand Challenge II")*, 2008.
Online available at http://www.midasjournal.org/browse/publication/256, March 2009.

**Other activities**

Reviewer for IEEE Transactions on Medical Imaging
Supervision of master theses and internships at the VRVis Research Center

**Hobbies**

Double bass, mountain bike, skiing.